Modulating and monitoring the microenvironment in cancer and renal fibrosis

Von der Medizinischen Fakultät
der Rheinisch-Westfälischen Technischen Hochschule Aachen
zur Erlangung des akademischen Grades
einer Doktorin der Theoretischen Medizin

genehmigte Dissertation
vorgelegt von

Maike Baues M. Sc.

aus

Würselen

Berichter: Herr Universitätsprofessor
Dr. sc. Hum. Twan Lammers

Herr Privatdozent
Dr. med. Peter Boor

Tag der mündlichen Prüfung: 03.02.2020

Diese Dissertation ist auf den Internetseiten der Universitätsbibliothek online verfügbar.

Parts of this thesis have been published in:

Theek B., **Baues M.**, Ojha T., Möckel D., Veettil SK., Steitz J., van Bloois L., Storm G., Kiessling F., Lammers T.: Sonoporation enhances liposome accumulation and penetration in tumors with low EPR. ***Journal of Controlled Release*.** (2016) 231:77-85

Baues M., Dasgupta A., Ehling J., Prakash J., Boor P., Tacke F., Kiessling F., Lammers T.: Fibrosis imaging: Current concepts and future directions. ***Advanced Drug Delivery Reviews*.** (2017) 121:9-26.

Theek B.*, **Baues M.***, Gremse F., Pola R., Pechar M., Negwer I., Koynov K., Weber B., Barz M., Jahnen-Dechent W., Storm G., Kiessling F., Lammers T.: Histidine-rich glycoprotein-induced vascular normalization improves EPR-mediated drug targeting to and into tumors. ***Journal of Controlled Release*.** (2018) 282:25-34

Sun Q.*, **Baues M.***, Klinkhammer B.M.*, Ehling J., Djudjaj S., Drude N.I., Daniel C., Amann K., Kramann R., Kim H., Saez-Rodriguez J., Weiskirchen R., Onthank D.C., Botnar R.M., Kiessling F., Floege J., Lammers T.$^{\#}$, Boor P.$^{\#}$: Elastin imaging enables noninvasive staging and treatment monitoring of kidney fibrosis. ***Science Translational Medicine*.** (2019) 486

Baues M.*, Klinkhammer B.M.*, Ehling J., Gremse F., van Zandvoort M.A.M.J., Reutelingsperger C.P.M., Daniel C., Amann K., Bábíčková J., Kiessling F., Floege J., Lammers T.$^{\#}$, Boor P.$^{\#}$: A collagen-binding protein enables molecular imaging of kidney fibrosis in vivo. ***Kidney International***. [in press]

Table of contents

List of abbreviations IV

1. Introduction 1

1.1. The microenvironment in cancer and fibrosis 1

1.2. Nanomedicines and theranostics 4

1.3. Modulation of the microenvironment 6

1.4. Monitoring of the microenvironment 10

2. Objectives 15

3. Material and Methods 16

4. Results 28

4.1. Vascular priming via macrophage re-education enhances drug delivery 28

4.2. Sonopermeation improves liposome delivery into tumors with low EPR 34

4.3. Collagen as an imaging biomarker of renal fibrosis 40

4.4. Elastin imaging enables noninvasive staging and treatment monitoring 44

5. Discussion 53

5.1. Vascular priming via macrophage re-education enhances drug delivery 53

5.2. Sonopermeation improves liposome delivery into tumors with low EPR 55

5.3. Collagen as an imaging biomarker of renal fibrosis 56

5.4. Elastin imaging enables noninvasive staging and treatment monitoring 57

6. Summary 58

7. References 60

8. Appendix 73

8.1. List of original publications 73

8.2. Acknowledgments 75

8.3. Erklärung zur Datenaufbewahrung 77

8.4. Erklärung über den Eigentanteil 78

8.5. Curriculum vitae 79

List of abbreviations

Act.	Actual
AIM2	Absent in melanoma 2 (Interferon-inducible protein AIM2)
ANOVA	Analysis of variance
α-SMA	Alpha smooth muscle actin
BP	Blood pressure
BW	Bandwidth
Ch.	Chapter
CKD	Chronic kidney disease
CNA35	Collagen-binding agent
CNR	Contrast to noise ratio
CRID3	Cytokine Release Inhibitory Drug 3
CT-FMT	Computed tomography-fluorescence molecular tomography
DAB	3,3'-Diaminobenzidine
DAPI	(4’-6-diamidine-2’-phenylindole dihydrochloride)
DMSO	Dimethyl sulfoxide
DSPE	1,2-Distearoyl-sn-glycero-3-phosphoethanolamine
DTPA	Diethylenetriaminepentaacetic acid
ECM	Extracellular matrix
EPR	Enhanced Permeability and Retention
ESMA	Elastin-specific imaging agent
FAN	Folic acid nephropathy
FFPE	Formalin-fixed paraffin-embedded
FITC	Fluorescein isothiocyanate
FOV	Field of view
FRI	Fluorescence reflectance imaging
fz	Frequency
Gd	Gadolinium
HER2	Human epidermal growth factor receptor 2
HRG	Histidine-rich glycoprotein
HRP	Horseradish peroxidase

ICP-MS	Inductively coupled plasma-mass spectrometry
IFP	Interstitial fluid pressure
IHC	Immunohistochemistry
I/R	Ischemia-reperfusion injury
i.p.	Intraperitoneal
i.v.	Intravenous
KO	Knockout
LA-ICP-MS	Laser ablation-inductively coupled plasma-mass spectrometry
MAR	Microautoradiography
MB	Microbubble
MI	Mechanical index
MM	Micromarker®
MR	Magnetic resonance
Mrc-1	Mannose receptor C-type 1
MRI	Magnetic resonance imaging
NBD-PE	*N*-(7-Nitrobenz-2-Oxa-1,3-Diazol-4-yl)-1,2-Dihexadecanoyl-sn-Glycero-3-Phosphoethanolamine
NLRP3	Nucleotide-binding domain, leucine-rich–containing family, pyrin domain–containing-3
ns	Not significant
NSA	Number of signal averages
NTN	Nephrotoxic nephritis
NTS	Nephrotoxic serum
PAS	Periodic acid–Schiff
PBCA	Poly(butyl cyanoacrylate)
PEG	Polyethylene glycol
pHPMA	poly(*N*-(2-hydroxypropyl)methacrylamide)
PlGF	Placental growth factor
rBV	Relative blood volume
ROI	Region of interest
scRNA-seq	Single cell RNA sequencing
SD	Standard deviation

SHG	Second harmonic generation
TAM	Tumor-associated macrophages
TE	Echo time
TEM	Transmission electron microscopy
TFE	Turbo field echo
TI	Inversion time
TPLSM	Two-photon laser scanning microscopy
TR	Repetition time
TSE	Turbo spin echo
US	Ultrasound
UUO	Unilateral ureteral obstruction
VEGFR	Vascular Endothelial Growth Factor Receptor
WFS	Water-fat shift
WT	Wild type

1. Introduction

1.1. The microenvironment in cancer and fibrosis

The tissue microenvironment is an active organization of cellular and non-cellular components. Homeostasis of the tissue microenvironment is maintained by precise crosstalk between the immune system, blood and lymphatic vasculature as well as stromal components. Such tight controls ensure the delicate balance of extracellular matrix (ECM) synthesis, post-translational modification, remodeling and degradation (Cox et al., 2014). ECM composition and organization is essential for a correct cellular behavior (Radisky et al., 2001), however, incorrect signaling from the microenvironment leads to destabilization of the tissue architecture and promotion of cell malignancy (Bissell et al., 2011). Most significant for fibrotic diseases is the induced excessive ECM deposition (Murray, 2015).

Fibrosis causes organ dysfunction, thereby it gives rise to life-threatening pathological conditions and is associated with over 45% of deaths in industrialized nations (Wynn, 2008). In recent years, the link between cancer and fibrosis has been an emerging area of interest. Fibrotic ECM remodeling is strongly connected to tumorigenesis, metastasis and hampered drug delivery to tumors, therefore it ultimately accounts for 90% of deaths from cancer (Cox et al., 2011, Ohlund et al., 2014).

Solid tumors contain not only malignant cells, >50% of their mass is in fact comprised out of endothelial cells, pericytes, adipocytes, immune cells (lymphocytes, neutrophils and macrophages), (myo)fibroblasts and ECM (Balkwill et al., 2012, Egeblad et al., 2010a, Klemm et al., 2015). The ECM is a complex 3D mesh of macromolecules, e.g. collagens, elastin, laminin, fibronectin, proteoglycans, glycoproteins and polysaccharides, that provides not only a static, physical cell scaffold but also an abundance of growth factors (Hui et al., 2015, Thomas et al., 2019). The interactions between cells and ECM create a dynamic network that has similarities to inflammatory and wound-healing processes and most importantly influences the cancer hallmarks (Dvorak, 1986, Mantovani et al., 2008, Pickup et al., 2014).

Already early on in tumorigenesis, the homeostasis of the microenvironment is disturbed and the biochemical as well as biomechanical properties of the ECM begin to change (Egeblad et al., 2010b). For example, the architecture of tumor-associated

collagens is severely altered, in form of linearization, thickening and crosslinking, which reflects the expression and post-translational modification status (Levental et al., 2009, Provenzano et al., 2006). Linearized fibers are most notable adjacent to the tumor vasculature and are stiffer than typical curly and anisotropic ones (Condeelis et al., 2003). This ECM stiffening potentiates the initiation of cell migration (Egeblad et al., 2010b, Zaman et al., 2006). In addition, the abnormal, leaky vasculature and the impaired lymphatic drainage increase the interstitial fluid pressure (IFP) (Heldin et al., 2004). This heterogonous pathophysiology of the tumor microenvironment comprises vascular, transvascular and interstitial transport routes as well as cellular uptake (Jain, 2001, Yazdani et al., 2017).

The fibrotic stroma affects disease progression and prognosis in various tumor types, e.g. breast, colon, pancreatic as well as head and neck cancer (Bachem et al., 2005, Tung et al., 2015). It is crucial to examine the environmental components responsible for tumor initiation and progression for the identification of commonalities between these seemingly distinct tumor types (Egeblad et al., 2010b, Hynes, 2009). Modifications of the ECM by means of growth factor production, activation of pathogenic signaling pathways and tissue remodeling are known to be crucial in fibrotic diseases and in promoting tumor growth and metastasis. Thereby, the desmoplastic reaction and increased ECM deposition in tumors is remarkably similar to organ fibrosis (Baues et al., 2017, Radisky et al., 2007). Over a century ago, Paget proposed the idea of “seed and soil” to explain the spread of solid tumors (de Groot et al., 2017). The microenvironment of the secondary tumor site has to be supportive for colonization of the metastasis (Cox et al., 2014, Poste et al., 1980). Underlying tissue fibrosis can be closely correlated with a risk of cancer in the respective organ (Radisky et al., 2007). For example, the existence of a predisposition in breast cancer has been shown (Jacobs et al., 1999), as well as an increased incidence of lung cancer formation with pulmonary fibrosis (Cox et al., 2014, Mossman et al., 1998).

Fibrosis is linked to chronic progressive failure in most organs, e.g. liver, lungs, heart and kidneys (Zeisberg et al., 2013). Alarmingly, chronic kidney disease (CKD) has reached an epidemic prevalence of 13% and is one of the major causes of death worldwide (Hill et al., 2016, Mortality et al., 2015). Fibrosis is the common endpoint of CKD and the best predictor for disease progression (Boor et al., 2010, Mills et al., 2015). A multitude of

stimuli, including trauma, infection, metabolic derangement, inflammation and autoimmunity can initiate and drive fibrosis (Rockey et al., 2015). The microenvironmental changes in renal fibrosis can be described as a variety of processes in different renal compartments (Djudjaj et al., 2019), thereby the ECM overproduction can be initiated by epithelial, endothelial and mesenchymal cells (Duffield, 2014). The progressive accumulation of ECM fibers in the glomerulus and tubulointerstitium disrupts the glomerular and tubular architecture and leads to microvascular compression (Aydin et al., 2008, Decleves et al., 2014, Tampe et al., 2014). Although multiple anti-fibrotic targets have been identified in preclinical research, translation into clinical routine has remained extremely poor (Baues et al., 2019). Major reasons therefore are the adverse effects of matrix-degrading approaches and the lack of diagnostic concepts to specifically, non-invasively and longitudinally assess kidney fibrosis (Kim et al., 2001, Klinkhammer et al., 2017, Zeisberg et al., 2006).

In case of cancer and fibrosis, the microenvironment contains many overlapping mechanisms and collective key players. The fibrotic elements within each microenvironment should be converted from challenges into opportunities with prognostic, response-predictive and targeting value. Given the significant similarities in fibrosis and cancer, diagnostic biomarkers and therapeutic strategies can be assessed that hold potential in both microenvironmental settings.

1.2. Nanomedicines and theranostics

One of the major disadvantages of intravenously (i.v.) administered anti-cancer treatments is the inefficient accumulation at the actual pathological target site. Typically, (chemo)therapeutic drugs suffer from a short blood half-life and an immense volume distribution causing severe systemic side effects (Allen et al., 2004, Langer, 1998, Theek et al., 2018). For several decades now, scientists have been developing 1-100(0) nm-sized nanocarrier materials and methods to address these delivery challenges. Theranostic nanomedicines, such as polymers, micelles and liposomes, can act as both therapeutic and diagnostic agents (Theek et al., 2014b). Depending on the design, the nanomedicines provide insight regarding a molecular target, vascular permeability, retention or drug release, if a chemotherapeutic drug is incorporated in their structure (Kiessling et al., 2014b). Nanomedicinal constructs are larger than the renal clearance threshold, circulate for a prolonged period of time in the blood and accumulate more efficiently at the pathological site compared to free low-molecular-weight chemotherapeutics (Nie, 2010, Peer et al., 2007, Theek et al., 2018).

The core concept for passive drug targeting to tumors is the enhanced permeability and retention (EPR) effect. This phenomenon is based on pathophysiological characteristics like hypervascularity, hyperpermeability and impaired lymphatic drainage and leads to a relatively effective gradual accumulation of nanomedicines at the malignant target site while avoiding healthy tissues (Bertrand et al., 2014, Maeda, 2012, Maeda et al., 2013, Matsumura et al., 1986, Theek et al., 2018). To date, the most progress, with the few nanomedicines approved for clinical use, has primarily been made in the reduction of adverse effects, e.g. decreased nausea, hair loss, anemia and cardiotoxicity (Bjornmalm et al., 2017, Shi et al., 2017, Stylianopoulos et al., 2015, von Roemeling et al., 2017). While this “site-avoidance drug delivery” is certainly important for patient tolerance, the key challenge, in form of response rates and survival times, e.g. “site-specific drug delivery”, remains insufficiently addressed (Jain et al., 2010, Lammers, 2013). The survival benefit of cancer nanomedicines has been modest in clinical trial, which is in stark contrast to the observed increase in survival in preclinical small animal studies (Bjornmalm et al., 2017, Petersen et al., 2016). This controversy gave rise to a whole debate questioning the relevance of the EPR effect for human tumors (Danhier, 2016,

Huynh et al., 2015, Lammers et al., 2016, Nakamura et al., 2015, Nakamura et al., 2016, Nichols et al., 2014, Prabhakar et al., 2013). In this context, the EPR effect should always be considered as a highly variable tumor feature in the first place, with differences from patient to patient, between primary tumor and metastasis in the same patient as well as within the same tumor microenvironment (Bjornmalm et al., 2017, Fang et al., 2011, Perry et al., 2017). Potential explanations for the heterogeneity are associated with the abnormal tissue environment, including the impaired blood flow, vascular permeability, stromal content, cellularity and IFP (Jain, 1990, Lammers et al., 2012). Consequently, the overall research focus has to shift from producing even more nanomedicines and drug delivery systems toward improving the monitoring and modulation of the EPR, in order to increase the chances of clinical success (Theek et al., 2016).

Furthermore, the field of nanomedicines has to recognize that cancer is certainly one of the most dreadful illnesses, but by no means the only one, and reach out to neighboring research areas (Bjornmalm et al., 2017). Presently, the majority of studies are focused on drug delivery to tumors, even though for example the global burden of CKD is dramatically increasing (82% increase in years of life lost over the past 2 decades) (De Nicola et al., 2016, Mitragotri et al., 2017). Recently, kidney diseases have been described as the most neglected chronic disease (Luyckx et al., 2018). A shift in the attention toward the implementation of nanomedicines in other diseases would be certainly beneficial. For the development of therapeutic strategies in CKD, the repurposing of drugs in form of nanomedicines has immense potential, because the pharmacokinetic properties and targetability are improved (Lin et al., 2017, Ramos et al., 2015).

In this regard, the most straightforward approach is the application of imaging for patient pre-selection. Naturally, a population is heterogeneous and therefore patients are likely to present various levels of responsiveness to nanomedicines (Ojha et al., 2015, Rizzo et al., 2013). In order to move forward, the microenvironmental features should be considered rather as advantages than challenges. The unique tissue composition can enable selective identification and novel biomarkers might create opportunities for treatment development.

1.3. Modulation of the microenvironment

In the past, many tumor-targeted nanomedicines have been assessed, however, the fewest provided convincing therapeutic performances. The accumulation and distribution is strongly affected by the highly heterogeneous microenvironment. Several pharmacological (vascular permeabilization, normalization, disruption and promotion) and physical (hyperthermia, radiotherapy, sonopermeation and phototherapy) modulation strategies have been explored for improving the EPR-mediated drug delivery (Ojha et al., 2017).

In this context, vascular normalization is a popular approach on the basis of counteracting pro-angiogenic signaling in the tissue (Carmeliet et al., 2011, Goel et al., 2011, Jain, 2005). During tumor development, the normally tightly controlled formation of new blood vessels is disturbed and the proliferating cancer cells as well as hypoxia cause an overproduction of vascular growth factors, such as Vascular Endothelial Growth Factor Receptor 2 (VEGFR2) (Theek et al., 2018). Already in the 1970s, strategies for the pharmacological inhibition of angiogenesis were proposed (Folkman, 1971). Vessel normalization in form of anti-angiogenic therapy aims for transient improvement of vascular function and structure by pruning away vessels, modifying the tumor microenvironment and thereby the outcome of the treatment. While anti-VEGF monotherapies were unsuccessful in clinical trials, a clear added value was reported in combination with chemo- and radio-therapeutic treatments (Jain et al., 2006, Willett et al., 2006). In HER2-negative breast cancer patients neoadjuvant treatment with bevacizumab, an anti-VEGF antibody, reduced the IFP and enhanced the pericyte-coverage on vessels. The better perfused vascular network leads to an improved drug delivery (Theek et al., 2018, Tolaney et al., 2015). Further chemotherapeutic drugs as well as nanomedicines have already been shown to benefit from vascular normalization (Chauhan et al., 2013, Jain et al., 2010, Khawar et al., 2015, Mpekris et al., 2017). However, the normalization of tumor blood vessels seems to improve the delivery of nanomedicines in a size-dependent manner, since the extravasation of 100 nm-sized Doxil® liposomes is impeded by the reduced pore size (Chauhan et al., 2012).

Tumor-associated macrophages (TAM), which are typically polarized toward a pro-angiogenic and immunosuppressive M2-like phenotype, can be a crucial factor in

vascular normalization (Huang et al., 2011). The histidine-rich glycoprotein (HRG), a highly abundant plasma protein, is the focus in one of the first studies investigating the effect of vascular normalization mediated via the repolarization of TAM (Rolny et al., 2011). HRG suppresses the expression of the placental growth factor (PlGF), which is overexpressed in several tumor types and acts pro-angiogenic by binding to VEGFR1 (Fischer et al., 2008, Olsson et al., 2004, Poon et al., 2011). HRG expression inhibits PlGF signaling and polarizes TAM from a pro-angiogenic M2-like phenotype toward the anti-angiogenic M1-like phenotype, which induces a priming of the vasculature that reduces tumor growth and metastasis (Jones et al., 2005, Theek et al., 2018, Tugues et al., 2012).

In order to systematically study the effect of macrophage-mediated tumor vessel normalization on the accumulation and penetration of a polymeric drug delivery system, HRG-knockout (KO) and wild type (WT) mice in combination with HRG-overexpressing or normal t241 fibrosarcoma cells were used (Figure 1). The 10-20 nm-sized polymers are based on pHPMA, poly(N (2 hydroxypropyl)methacrylamide) (Theek et al., 2018).

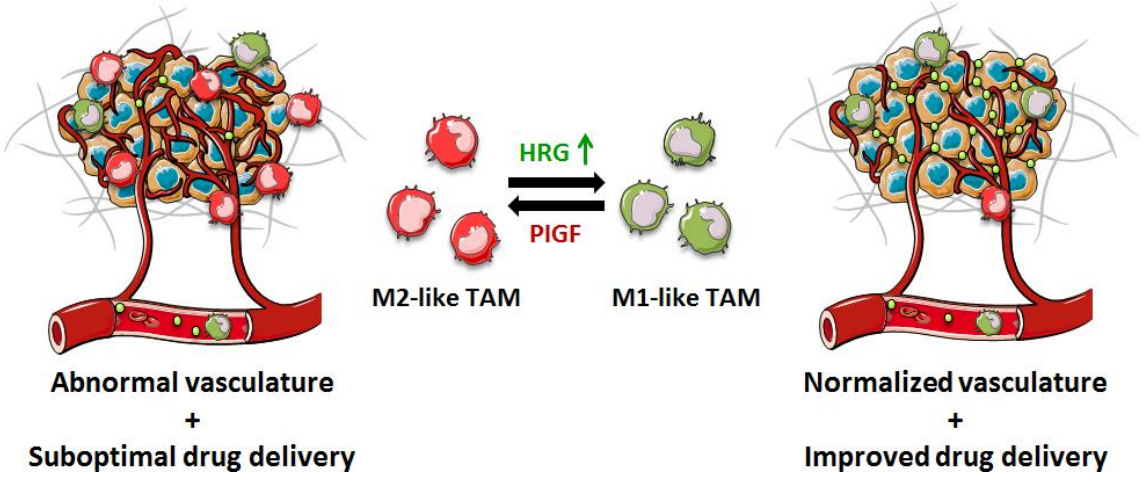

Figure 1: The expression of the histidine-rich glycoprotein (HRG) affects the polarization of tumor-associated macrophages (TAM) and induces a M1-like anti-angiogenic phenotype in tumors, which primes the vasculature by means of downregulation of the placental growth factor (PIGF) (Theek et al., 2018).

The combined use of ultrasound (US) and microbubbles (MB) received increasing attention in the last decade, as a promising approach to enhance drug extravasation and penetration (Kiessling et al., 2014a, Kooiman et al., 2014, Lammertink et al., 2015,

Lentacker et al., 2014, Mo et al., 2012). Originally, this strategy was referred to as sonoporation. However, Snipstad *et al.* propose the use of the broader term sonopermeation, which covers more biological effects than the formation of pores in cell membranes (Snipstad et al., 2018). Besides transient pore formation, sonopermeation describes additionally the opening of tight junctions in the vascular endothelium, stimulation of endocytosis, transcytosis and exocytosis, along with macroscopic changes in perfusion and the perivascular space (Hersh et al., 2016, Meijering et al., 2009, Rix et al., 2014, Ross et al., 2002, Sheikov et al., 2008, Snipstad et al., 2018, Yuana et al., 2017). Stable cavitation occurs at relatively low amplitudes and induces MB oscillation that results in streaming, generation of shear force and push-pull-effects which contribute in the transfer of drugs over membranes (Frenkel, 2008, Kooiman et al., 2014, Lentacker et al., 2014, Snipstad et al., 2018). Inertial cavitation derives from an increased acoustic pressure at larger amplitudes causing the MB to collapse, which creates shock waves and liquid jets (Husseini et al., 2014, Lentacker et al., 2014). Following the collapse of MB, both temporary and permanent pores of various sizes from 1-3000 nm are generated (Hu et al., 2013, Snipstad et al., 2018, Zhao et al., 2008).

Thus far, sonopermeation has been extensively used for nucleic acid delivery *in vitro* (Dewitte et al., 2014). One of the most developed and promising *in vivo* applications is the sonopermeation of the blood brain barrier for drug delivery into the brain (Lammers et al., 2015, Poon et al., 2017, Song et al., 2018). Beyond the sonopermeation of the brain or brain tumors, the majority of studies in other solid tumors has focused on drug delivery systems that are directly loaded onto the MB (Cochran et al., 2011, Li et al., 2012, Tinkov et al., 2010). The first clinical trial demonstrating the enhanced therapy efficiency was in patients suffering from inoperable pancreatic cancer and used a combination of free gemcitabine and sonopermeation (Dimcevski et al., 2016).

Therefore, the systematic analysis of the impact of sonopermeation on the accumulation and penetration of fluorophore-labeled liposomes is essential for the progression of this technology. Two types of MB formulations with different oscillation potential, i.e. phospholipid soft-shell and polymer-based hard-shell MB, are assessed in two tumor models (Figure 2). The highly cellular A431 epidermoid tumors as well as the extremely stromal adenocarcinoma BxPC-3 are both characterized by low levels of EPR.

Sonopermeation as a modulating strategy is an interesting method to improve the efficacy of nanomedical treatments (Theek et al., 2016).

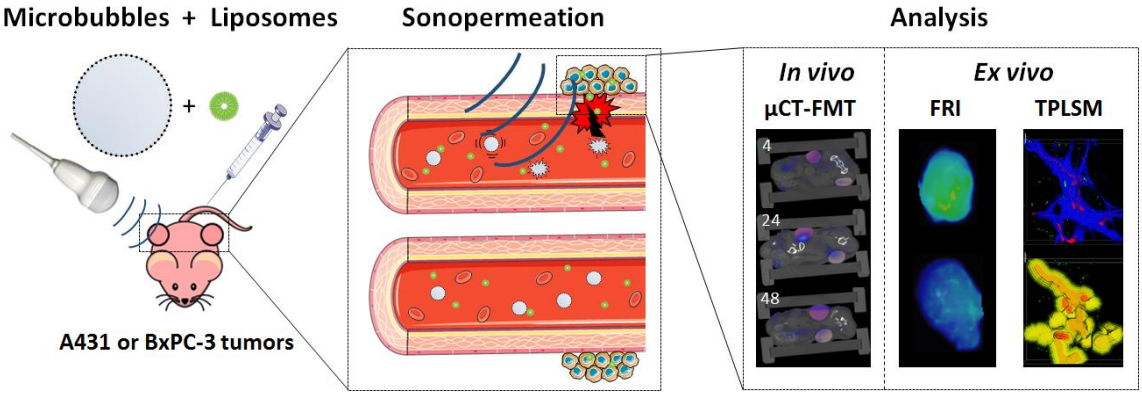

Figure 2: Sonopermeation, which is based on the combination of ultrasound (US) and microbubbles (MB), improves the accumulation and penetration of liposomes in tumors, characterized with low levels of Enhanced Permeability and Retention (EPR) effect (Theek et al., 2016).

Overall, the potential value of these modulating strategies depends also to a large extent on their availability and clinical acceptance. In this regard, neoadjuvant pharmacological priming of the microenvironment with clinically already approved pharmaceuticals may be an attractive and straightforward approach for improving the tumor accumulation and distribution of nanomedicines. A key consideration for these agents should also be the practicality of this therapeutic intervention for patients with metastases. Consequently, physical modulation strategies might be appealing because of their local and temporal confinement (Ojha et al., 2017). For a successful clinical translation, future research should try to combine these microenvironment modulating interventions with molecular biomarkers that allow for real-time feedback, non-invasive longitudinal monitoring and therapeutic outcome prediction.

1.4. Monitoring of the microenvironment

Besides strategies to address heterogeneity in drug delivery, the development of imaging biomarker to predict and monitor treatment effects are essential. Accurate diagnosis and staging of fibrosis is essential for proper prognosis and progression monitoring. The presence and severity of fibrosis actually is the best predictor for disease progression in CKD (Baues et al., 2017, Khwaja et al., 2007). Traditionally, needle-based biopsies have been the gold standard for fibrosis diagnosis and staging. At present, biopsies are still the only available means to specifically diagnose and stage renal fibrosis (Sun et al., 2019).

In case of tumors, a biopsy is the standard diagnostic procedure to determine the nature and stage of the tumor, as well as its malignant potential. Although the essential role of desmoplastic processes for tumor growth and metastasis has been recognized (Mahadevan et al., 2007), they are not considered in routine pathological assessments. Many studies have suggested that especially in invasive colorectal cancer (Park et al., 2015, Park et al., 2014, Ueno et al., 2002) and in pancreatic ductal adenocarcinoma (Bijlsma et al., 2015, Neesse et al., 2011, Wang et al., 2016), the desmoplastic reaction is a key hallmark determining therapeutic outcome. However, thus far, histopathological information on e.g. myxoid stroma as an indicator for epithelial-to-mesenchymal transition (Ueno et al., 2002), has not yet managed to become broadly accepted and implemented for disease differentiation, prognosis assessment and treatment selection (Baues et al., 2017, Ueno et al., 2015).

While needle-based biopsies play an important role, they are nevertheless faced with multiple limitations including their invasive nature, procedure associated risks, limited representativeness for the entire organ, and inter- and intra-observer sampling variability (Baues et al., 2017, Manning et al., 2008). Furthermore, biopsies are not suitable for longitudinal monitoring or therapy response assessment, i.a. due to the increasing risk of complications (Farrar et al., 2015, Hogan et al., 2016, Sun et al., 2019).

In tumors, biopsy-based diagnosis is particularly complicated, because of intrinsic heterogeneity in the primary tumor and (in)between metastases (Gerlinger et al., 2012). Also the accessibility of the pathological site and the risk of spreading/seeding cancer cells play an important role (Robertson et al., 2011). In light of these limitations, liquid biopsies are increasingly emerging in the field of cancer diagnosis as a refined and

non-invasive alternative or potential add-on to needle-based biopsies (Diaz et al., 2014). A liquid biopsy, in the form of a blood sample, can provide information on the genetic profile of cancerous lesions by means of analyzing circulating tumor cells or circulating cell-free tumor DNA (Alix-Panabieres et al., 2016, Baues et al., 2017, Crowley et al., 2013).

Because of their high applicability, reproducibility and widespread availability, liquid-based biopsies not only hold great promise for cancer diagnosis, but also for the assessment of other fibrotic diseases. In kidney fibrosis, liquid biopsy-based biomarkers can be measured in blood as well as in urine. In this regard, the correlation of transforming-growth factor-β and bone morphogenetic protein-7 levels in both blood and urine have been known to correlate well with the degree of fibrosis (Wong et al., 2013). Additionally, the urinary ratio of the N-terminal propeptide of collagen III to the matrix metallopeptidase-generated collagen III degradation fragment has been identified to reflect ECM turnover in multiple rat models as well as in patients suffering from IgA nephropathy (Genovese et al., 2016, Papasotiriou et al., 2015).

Shortcomings of liquid-based biomarkers are, that they may not be origin-specific enough, that they may be limited to the indication of impaired organ function or inflammatory state, and in particular that they may not specifically reflect the microenvironment or discriminate between different stages of fibrosis (Genovese et al., 2014, Sangwaiya et al., 2014). The abovementioned new biomarkers may help to provide more fibrosis-specific information, since they mostly assess molecules of the ECM. These novel microenvironment-based markers now require validation in large cohorts of patients and in long term studies (Genovese et al., 2014). In the future, such liquid biopsy techniques may be used in combination with other modalities, such as imaging, to improve the accuracy of diagnosis and staging (Baues et al., 2017).

In the last decade, non-invasive imaging has received a lot of attention for the assessment of cancer and fibrosis. Approaches typically include anatomical, functional and molecular imaging techniques that allow for the examination of the affected organ (or even the whole body) in a readily repeatable manner. This makes non-invasive imaging not only attractive for initial diagnosis, but especially also for staging and for monitoring disease progression. Several imaging modalities and protocols have been evaluated for this purpose over the years, ranging from the basic assessment of

morphological changes, over quantifiable differences in functional properties, to the identification of molecular adaptations and disease-specific changes. Importantly, non-invasive imaging can also be employed for treatment monitoring, thereby potentially facilitating the clinical translation of novel therapies (Baues et al., 2017).

Thus far, only a relatively small number of diagnostic methods have been evaluated and established for imaging the fibrotic tumor stroma. In most of these cases, anatomical and functional imaging techniques are employed. The identification of fibrotic tumors becomes complicated if the tumor is located within a fibrous organ or tissue, and in case of contrast-enhanced scans, if tumor perfusion is hindered (Erkan et al., 2012a). A typical example of this is pancreatic cancer, in which fibrosis of the tumor and of the surrounding non-malignant parts of the pancreas strongly influences which imaging technique can be employed and which surgical decisions have to be made in terms of intraoperative tumor border definition and resection strategy (Erkan et al., 2012b). Only a few imaging modalities (X-ray, MRI and US) have been employed to assess tumor fibrosis, and they have so far only focused on anatomical and functional information. Recently, the performance of the collagen type I targeted MRI contrast agent EP-3533, which had been previously tested for the visualization of liver fibrosis, was evaluated in an orthotopic pancreatic ductal adenocarcinoma model. Compared to a non-binding control MR agent, the uptake of EP-3533 was found to be specific and not the result of the leaky tumor vasculature (Yu et al., 2012). Considering the dynamic changes which are continuously going on in tumor microenvironment at the molecular level, targeted molecular imaging agents which are specific for stromal biomarkers in the tumor microenvironment may hold significant potential, not only for better diagnosis, staging and prognosis prediction, but also for individualizing and improving therapeutic interventions (Baues et al., 2017).

Several anatomical and functional imaging techniques, which originate either from standard clinical procedures to categorize a patient with abnormal kidney function or from the assessment of fibrosis in other organs, have been adapted over the years to monitor kidney fibrosis. Unfortunately, they have not really turned out to be useful for improving diagnosis, staging or treatment monitoring in patients with renal fibrosis and CKD. To improve the non-invasive assessment of kidney fibrosis, and to provide novel tools and technologies for assessing the efficacy of novel anti-fibrotic and anti-CKD

therapies, it therefore seems imperative to develop molecular imaging agents. These could be targeting biomarkers of the microenvironment, e.g. certain kidney cells or components within the ECM, which are able to report sensitively and specifically the progressions of renal fibrosis and CKD (Baues et al., 2017).

Based on the above mentioned insights and efforts, the aim is to establish molecular imaging agents for non-invasive assessment. Fibrosis is characterized by pathological production and accumulation of ECM, mainly comprising collagens. The collagen-binding agent (CNA35) is a bacterially derived protein fragment of 35 kDa, which binds specifically to fibril-forming collagens and which has already been shown to hold promise for visualizing cardiovascular fibrosis (Krahn et al., 2006, Megens et al., 2007, Sanders et al., 2011). Multimodal optical imaging is used to visualize and quantify collagen deposition in murine models of kidney fibrosis by means of CNA35 (Figure 3).

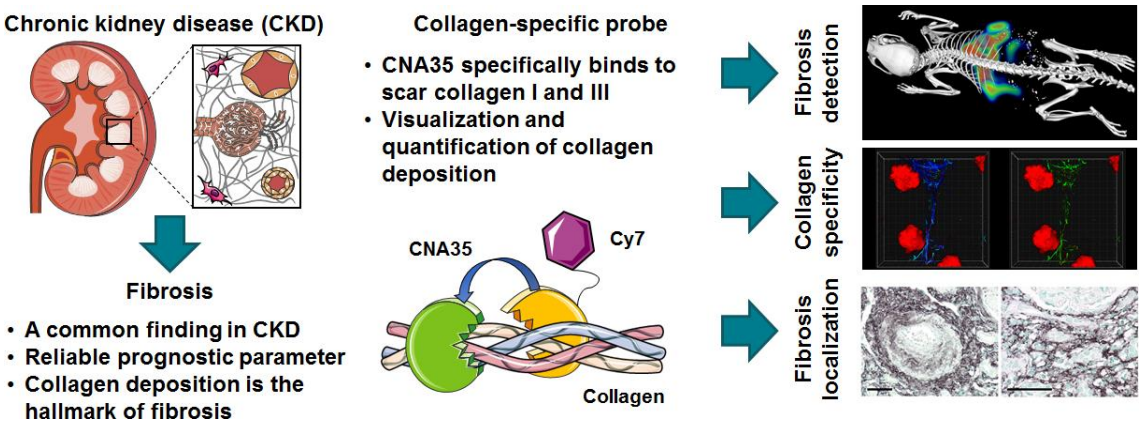

Figure 3: CNA35-based collagen-specific molecular imaging enables the non-invasive quantification of perivascular and interstitial renal fibrosis (Baues et al., 2019).

In comparison to collagen, elastin is present in even lower amounts in healthy tissue, which makes the molecular imaging of this ECM protein with the elastin-specific imaging agent (ESMA) interesting for staging and treatment monitoring of fibrosis (Figure 4). ESMA was initially shown to be useful for visualizing and quantifying elastin levels in atherosclerotic plaques (Makowski et al., 2011). The proof-of-principle for imaging liver fibrosis using ESMA was recently provided, demonstrating strong perivascular accumulation in the livers of mice exposed to CCl_4 for 6 weeks using delayed-enhancement magnetic resonance imaging (MRI) (Ehling et al., 2013).

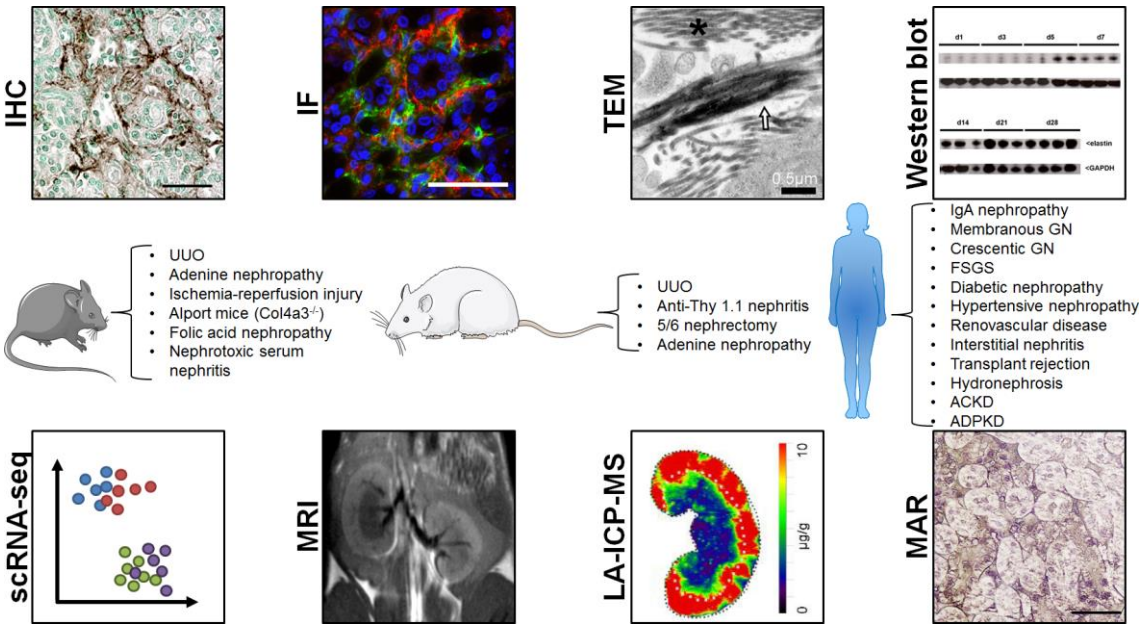

Figure 4: Elastin expression in kidney fibrosis and its potential as an imaging biomarker. The elastin deposition is assessed in 10 mouse and rat models as well as in >140 human samples from all major renal pathologies (Membranous GN: membranous glomerulonephritis; Crescentic GN: crescentic glomerulonephritis including Pauci-immune glomerulonephritis and lupus nephritis; FSGS: focal segmental glomerulosclerosis; Rejection: acute and chronic antibody and T cell-mediated renal rejection; ACKD: acquired cystic kidney disease; ADPKD: autosomal dominant polycystic kidney disease). The displayed methods evaluate elastin and elastin-based molecular MRI as non-invasive means to visualize, quantify and stage kidney fibrosis (IHC: Immunohistochemistry, IF: Immunofluorescence, TEM: Transmission electron microscopy, scRNA-seq: Single cell RNA sequencing, LA-ICP-MS: Laser ablation-inductively coupled plasma-mass spectrometry, MAR: microautoradiography) (Sun et al., 2019).

All things considered the recent advances in the clinical management of cancer and fibrosis have been relatively modest. An effective treatment substantially relies on strategies for diagnostic observation, in combination with patient selection and therapy response monitoring. The identification of innovative probes and protocols that are able to specifically visualize and quantify pathophysiological changes in the microenvironment should be part of the drug discovery process and help to establish diagnostic and therapeutic interventions for many severe diseases.

2. Objectives

The dynamic nature of the microenvironment is important in the progression of many diseases. An increased deposition of ECM components is observed in fibrotic conditions, in which it alters biochemical and mechanical properties, and compromises tissue function. Similarly, tumor cell invasion and metastasis are driven by the continuous and progressive remodeling of microenvironmental cues. The priming of the ECM by fibrosis can precede or follow tumor development. Therefore, the inherent plasticity should be harnessed for the development of diagnostic approaches to establish novel clinical endpoints and therapeutic strategies that reeducate the microenvironment.

In this thesis, two interventions modulating the EPR effect in tumors are evaluated regarding their impact on drug delivery. Firstly, the effect of HRG knockout and HRG overexpression on the accumulation and penetration of fluorophore-labeled polymeric drug carriers is assessed in t241 fibrosarcoma tumors. Increased expression of HRG drives TAM polarization toward an anti-angiogenic M1-like phenotype, resulting in normalized tumor blood vessels, which is intended to improve tumor-targeted drug delivery (Ch. 4.1). In addition, sonopermeation is applied to enhance the tumor macro-accumulation and micro-distribution of liposomal drug carriers. Sonopermeation is applied in highly cellular A431 xenografts and in highly stromal BxPC-3 xenografts, aiming to increase nanocarrier penetration into the tumor interstitium (Ch. 4.2).

Furthermore, the pathological microenvironment is explored for non-invasive staging and longitudinal treatment/progression monitoring in renal fibrosis with imaging probes specific for collagen and elastin. In Ch. 4.3, ECM deposition is visualized with the collagen-specific protein CNA35. Multimodal imaging is used to show specific CNA35 binding to fibril-forming collagens. Elastin expression is analyzed in mouse, rat and human kidneys at various CKD stages and ESMA-based MRI is applied to visualize anti-fibrotic therapy responses, fibrosis progression and reversal (Ch. 4.4). The diagnostic performance is also compared to clinical protocols assessing kidney function.

Overall, modulating the microenvironment improves EPR-mediated nanocarrier delivery in tumors and holds significant potential for individualizing therapeutic interventions. ECM monitoring as a novel and robust fibrosis-specific diagnostic tool, may provide feasible surrogate endpoints for clinical studies evaluating anti-fibrotic therapies.

3. Material and Methods

Polymer synthesis

For the synthesis of the 10-20 nm-sized polymeric pHPMA drug carrier based on poly(*N*-(2-hydroxypropyl)methacrylamide), a copolymer precursor was prepared by radical copolymerization of (*N*-2-hydroxypropyl)methacrylamide (HPMA, 85 mol %) and 3-(*N*-methacryloyl glycylglycyl) thiazolidine-2-thione (Ma-GG-TT, 15 mol %) in DMSO at 50 °C for 6 h, as previously described (Etrych et al., 2007, Rihova et al., 2000). The fluorophores ATTO 488-NH_2 and Dy750-NH_2 were dissolved with the synthesized poly(HPMA-co-Ma-GG-TT) in *N,N'*-dimethylacetamide and *N,N'*-diisopropylethylamine. The polymer was aminolyzed after 30 min with 1-aminopropan-2-ol and precipitated by using diethylether and centrifugation. Further purification was performed using high performance liquid chromatography with a Chromolith® SemiPrep RP18 encapped 100-10 mm column and then by gel filtration on a PD-10 desalting column containing Sephadex G-25 resin in water (GE Healthcare, Germany). The final molecular weight of the polymer was 67 kDa, the polydispersity index was 1.7 and the content of ATTO 488 was 2.1% (w/w) and of DY-750 1.6% (w/w) (Theek et al., 2018).

Liposome synthesis

Liposomes were prepared based on a post-insertion film-method (Bartneck et al., 2015, Ergen et al., 2019). PEG-PE micelles were prepared by mixing PEG(2000)-DSPE-NH_2 and PEG(2000)-DSPE (Avanti Polar Lipids, USA), and used for labeling the liposomes. Alexa Fluor 750 NHS (Invitrogen, USA) and NBD-PE (Molecular Probes, USA), which is fluorescent at 488 nm, were covalently linked to the micelles. During the mixture PEG(2000)-DSPE-NH2 was present in 5-fold excess compared to both fluorophores. During this process the mixture was heated to 60°C for 10 min. Subsequently, the labelled micelles were added to the liposomes and heated for 5 min at 60°C, followed by 10 min of mixing at room temperature. After extrusion through a polycarbonate filter a mean diameter of 133 nm and a polydispersity index of 0.04 were obtained (Theek et al., 2016).

Microbubble synthesis

Poly(butyl cyanoacrylate) (PBCA)-based microbubbles (MB) were synthesized as described previously (Fokong et al., 2011). *N*-Butyl cyanoacrylate monomers were titrated to an aqueous solution containing 1% (w/v) TritonX-100 at pH 2.5, under stirring at 10,000 rpm for 1 h using an Ultra-turrax (IKA-Werke, Germany). Following the synthesis, several washing steps were performed and the MB size was determined with a Multisizer 3 in ISOTON II at room temperature (Beckmann Coulter). The size distribution was 2.5 ± 1 µm (Appold et al., 2017, Theek et al., 2016).

CNA35 synthesis

CNA35 was produced as described previously (Krahn et al., 2006) and labeled with Cy7 for *in vivo* and with FITC for *ex vivo* optical imaging. A scrambled version of CNA35, i.e. with amino-acid substitution Y175K, rendering it unable to bind to collagen, was used as a control (Baues et al., 2019).

Animal experiments

All animal experiments were performed according to the regulations of the local and national ethics committee for animal welfare. Mice were housed under standard (specific pathogen-free) conditions with constant temperature and humidity under a 12-hour phase light-dark cycle with free access to drinking water (ozone-treated and acidified) and food. All *in vivo* imaging experiments were conducted under continuous inhalation anesthesia using 2% (vol/vol) isoflurane. To reduce background fluorescence in the FMT scans, the diet was changed to chlorophyll-free food (ssniff Spezialdiäten GmbH, Germany) three days prior to the imaging experiments. Every effort was made to minimize animal suffering.

Tumor models:

C57BL/6J mice (WT) were obtained from Charles River (The Netherlands). B6-(HRG33)tmwja1 mice (KO), a viable and fertile $HRG^{-/-}$ null mutation, have been provided by the Institute for Biomedical Engineering - Biointerface Laboratory and have been described previously (Tsuchida-Straeten et al., 2005). For both phenotypes, 5-8 week-old male and female mice were used. One million t241 cells (i.e. murine fibrosarcoma) or HRG-overexpressing t241 cells (t241-HRG^{+}) (Rolny et al., 2011) were

inoculated subcutaneously into the right flank of the mice, and tumors were allowed to grow to a diameter of 6-7 mm (Theek et al., 2018).

For the sonopermeation study, 6-8 week old female CD-1 nude mice were ordered from Charles River (The Netherlands). Four million A431 cells, i.e. human epidermoid, or five million BxPC-3 cells, i.e. human pancreatic adenocarcinoma, were inoculated subcutaneously into both flanks of each mouse, and tumors were allowed to grow to 6-8 mm in diameter (Theek et al., 2016).

Kidney fibrosis models:

For the fibrosis studies, all surgeries were performed under anesthesia by Ketamine (14 g/kg body weight) and Xylazine (8 g/kg body weight). Analgesia with Temgesic (0.05 mg/kg body weight) was used until 72 h post the operation. During the surgical period, body temperature was maintained between 35°C and 37.5°C using a temperature-controlled heating system. Mouse models applied in kidney fibrosis investigation include:

Unilateral ureteral obstruction (UUO), conducted in 10 week-old C57BL/6N mice, with kidneys from both obstructed and contralateral sides harvested at days 1, 3, 5, 7, 10, 14, 21 after UUO induction. I/R (ischemia-reperfusion injury) was performed in C57BL/6N mice. Here, the mice were sacrificed and kidneys excised on the 1, 3, 5, 7, 10, 14, 21 day after I/R induction, respectively. Adenine nephropathy was induced in 10 week-old C57BL/6N mice by feeding a 0.2% adenine diet. Kidneys were harvested on day 1, 3, 5, 7, 14, 21. In this case, healthy mice of day 1 were used as controls. Alport mice $Col4a3^{-/-}$ that are based on a 129/SvJ background, were analyzed at 4 and 8 weeks age. As a control for this model, wild type littermates of 8 weeks were used. Folic acid nephropathy (FAN) was induced in 10 week-old C57BL/6N mice by weekly i.p. injection of folic acid (250 mg/kg of body weight and dissolved in $NaHCO_3$) for 8 weeks in total. The model of nephrotoxic nephritis (NTN) was induced in 13 week-old male C57BL/6N mice by a single i.p. injection of 750 µl NTS and 40 µg CpG-oligonucleotide (Djudjaj et al., 2016, Ehling et al., 2016, Sun et al., 2019).

For the *in vivo* MR imaging studies in kidney fibrosis the UUO, I/R as well as the adenine nephropathy model were chosen. In case of the adenine nephropathy group healthy mice were used for the control cohort. In the UUO and I/R groups contralateral kidneys

were applied as controls. Further, the adenine nephropathy model was also employed to study the pharmacokinetics of ESMA. In order to monitor fibrosis progression MRI measurements were performed before as well as 24, 48 and 72 h after ESMA injection on day 0, day 14 and day 21 of the adenine diet (Sun et al., 2019).

To investigate whether ESMA can monitor therapeutic effects on renal fibrosis, mice with adenine nephropathy were treated with CRID3, an inhibitor of the nucleotide-binding domain, leucine-rich–containing family, pyrin domain–containing-3 (NLRP3) inflammasome and absent in melanoma 2 (AIM2) interferon-inducible protein (0.2 µg/g i.p daily), continuously over the course of the adenine diet. On day 21 MRI was performed before and 24 h after ESMA injection. In addition, the I/R model was also chosen to assess applicability of ESMA in monitoring anti-fibrotic therapy effects. From day 7 until day 21 I/R mice either received the tyrosine-kinase inhibitor Imatinib (50 mg/kg in H_2O, given daily via oral gavage) or normal H_2O as a control solution. On day 21 MRI was performed for both, before and 24 h after ESMA injection (Sun et al., 2019).

To study the detection sensitivity of elastin-based fibrosis imaging, in comparison to clinical standard kidney function assessment, a reversible model of adenine nephropathy was utilized. The mice were fed for 14 days with a 0.2% adenine diet and subsequently received normal food for 14 days. In this adenine recovery experiment MRI was performed on day 0, 14 and 21 with measurements before and 24 h after the injection of ESMA (Sun et al., 2019).

Further, the I/R model was used to confirm the binding specificity of ESMA to elastin in a competition experiment. On day 21, mice were injected i.v. with 25-fold excess of ^{69}Ga-ESMA (5 mmol/kg bodyweight). ^{69}Ga is a stable gallium isotope that does not alter signal intensities in MRI. After 4 h mice were additionally injected with the standard ^{153}Gd-ESMA (0.2 mmol/kg bodyweight) and MRI was performed 4 h and 24 h after ^{153}Gd-ESMA injection (Sun et al., 2019).

Human renal tissue

Kidney tissues provided by the Institute of Pathology of the RWTH Aachen University Clinic as well as the Institute of Pathology and Department of Nephropathology, both located at the University Erlangen, were used for immunohistochemical and

immunofluorescent stainings. The studies were approved by the local review boards of Aachen and Erlangen and are in line with the Declaration of Helsinki. Non-fibrotic, e.g. healthy, kidney tissue was obtained from 44-62 years old patients, including 2 males and 4 females. The nephrectomy specimens were received due to traumatic injury (n=2), discarded transplant kidney (n=1) and tumor-distant areas of tumor nephrectomies (n=3). Fibrotic kidney biopsies of patients age 49-74 years, in total 3 males and 3 females, were employed, including cases of chronic pyelonephritis (n=3), obstructive nephropathy with hydronephrosis (n=2) and nephrolithiasis (n=1). To comprehensively analyze the expression of elastin in different kidney diseases and different CKD stages, additional archival formalin-fixed paraffin-embedded (FFPE) kidney tissues were collected and stained (Sun et al., 2019).

Ultrasound sonopermeation

For the sonopermeation study, the VisualSonics Vevo2100 imaging system (Fujifilm Sonosite, The Netherlands) was employed. After the mice had been placed on the US table, the tumor mass was focused in B-mode and a tail vein catheter was inserted for liposome and non-targeted MB administration. Directly after the injection of 2 nmol of liposomes, either 5×10^8 PBCA (polymer-based hard-shell) MB or 4×10^8 Vevo Micromarker® (MM, VisualSonics, Toronto), which are phospholipid-based soft-shell MB, were injected. Subsequent to these bolus injections, the MB were continuously destroyed at the tumor location, by moving the transducer over the volume of interest, applying Power Doppler US (fz = 16 MHz; MI = 0.9) for 10 min (Theek et al., 2016).

Hybrid CT-FMT and FRI

Hybrid computed tomography-fluorescence molecular tomography (CT-FMT) and fluorescence reflectance imaging (FRI) were performed using an in-house optimized procedure (Gremse et al., 2015, Kunjachan et al., 2013). Anesthetized mice were placed onto a custom-made mouse bed enabling both CT (CT Imaging, Germany) and FMT (PerkinElmer, USA) imaging. CT scans with 720 projections in 1.1 full rotations on a flat panel detector with the size of 1032 × 1012 pixels were obtained. Mice were then transferred to the FMT and FRI device, to assess the biodistribution of the administered fluorescently-labelled drug delivery system or contrast agent. For a partial body scan covering the tumor region 45-60 FMT scan points and for a full body scan 100-120 FMT

scan points were acquired, while lying on a grid with an inter-individual distance of 3 mm, for top and bottom orientation of each mouse. CT-FMT imaging was done at multiple time points after the respective i.v. injection. At the end of the *in vivo* experiment, functional blood vessels were stained via i.v. injection of rhodamine-labeled lectin (Vector Laboratories, USA), to facilitate fluorescence microscopy and TPLSM. Organs were excised and imaged *ex vivo* in the fluorescence reflectance mode at 750 nm, to obtain an image of the accumulation on a whole organ level. Afterwards, the organs were embedded in TissueTek O.C.T. (Sakura Finetek Europe, The Netherlands) and cryopreserved at -80 °C (Theek et al., 2018, Theek et al., 2016). In case of the HRG experiment a mixture of TissueTek O.C.T. containing 1% (vol/vol) Imeron (Bracco, Konstanz, Germany) and 5% (vol/vol) Intralipid (Fresenius Kabi, India) was applied for embedding to allow additional *ex vivo* CT-FMT imaging (Theek et al., 2018).

MRI

The elastin-specific molecular imaging agent ESMA is a low molecular weight (855.95 Da) combination of ^{153}Gd-DTPA and the D-amino acid D-phenylalanine, which was previously extensively characterized to specifically bind elastin. Unbound ESMA has a longitudinal relaxivity of 4.7 ± 0.1 mM^{-1} s^{-1}, elastin-associated ESMA has a relaxivity of 8.7 ± 0.4 mM^{-1} s^{-1} at 3 T (Makowski et al., 2011). ESMA was solved in 100 µl physiologic saline. Commercially available unspecific Gd-DTPA (gadolinium-diethylenetriaminepentaacetic acid), Magnograf, (Bayer Pharma AG, Germany) was used as a control. Both ESMA and Gd-DTPA were administered in the same concentration of 0.2 mmol/kg bodyweight.

For *ex vivo* MRI of frozen human kidney tissue, the biopsy specimen were incubated for 1 h with ESMA or Gd-DTPA at room temperature. For both ESMA and Gd-DTPA the same concentration of 0.2 mmol/kg was used in physiologic saline, equally to the applied concentration in the animal experiments. Three washing steps in physiologic saline for 5 min followed, before all biopsy samples were embedded in 10% gelatin for MRI measurements (Sun et al., 2019).

All MRI measurements were performed at the 3.0-T clinical MR imaging system (Achieva 3.0 T TX, Philips Healthcare, The Netherlands) equipped with a standard clinical gradient system (30 mT/m, 200 mT/m per millisecond). A specialized 3 T solenoid mouse coil Rx of 127.728 MHz was used (Philips Medical System International B. V., The Netherlands).

The mice were imaged in prone position and MR scanning was performed prior to, 4 h and 24 h after contrast agent injection. The imaging protocol included a scout sequence, T1-weighted TSE (turbo spin echo) sequence, T2-weighted TSE sequence, T1-weighted inversion recovery TFE (turbo field echo) sequence as well as T1 relaxometry measurements. For the gelatin embedded human biopsy samples the MR scanning procedure was reduced to the scout sequences, T1-weighted TSE sequence as well as T1 relaxometry measurements (Sun et al., 2019).

T1-weighted TSE images were acquired with the following parameters: Repetition time (TR)/echo time (TE) = 500/20 ms, slice thickness = 0.7 mm, field-of-view (FOV) = 84 mm, water-fat shift (WFS) (pix) / Bandwidth (BW) (Hz) = 1.694/256.4, slices = 10, total scan duration ≈ 9 min.

T2-weighted TSE images were acquired with the following parameters: TR/TE = 2000/100 ms, slice thickness = 1 mm, FOV = 84 mm, WFS (pix) / BW (Hz) = 1.705/254.08, and slices = 9, a total scan duration ≈ 7 min.

T1-weighted inversion recovery TFE sequence parameters: TR/TE/inversion time (TI) = 27/8/500 ms, slice thickness = 0.5 mm, FOV = 30 mm, NSA (Number of Signal Averages) = 2, Act. (actual) WFS (pix) / BW (Hz) = 12.430/35.0, Echoes = 1, flip angle = 30° and slices = 9, total scan duration ≈ 20 min.

T1 relaxometry sequence: TR/TE = 6.5/3.4 ms, slice thickness = 1 mm, FOV = 42 mm, flip angle = 30°, TFE shots = 60, prepulse inversion time = 280ms, phase interval = 400ms, NSA = 1, Act. WFS (pix) / BW (Hz) = 1.126/385.8, and slices = 16, total scan duration ≈ 6 min.

Image analysis

The imaging data sets were analyzed using the Imalytics Preclinical software (Gremse-IT GmbH, Germany) (Gremse et al., 2016). In the hybrid CT-FMT measurements, organ and tumor segmentations are based on the anatomical CT data and were used to quantify fluorescence signal allocated to the tumors or other organs and expressed as % of the injected dose (%ID). For the CNA35 study the organ accumulation was normalized to the total fluorescence intensity measured at 3 h post injection. The fluorescence signals allocated to tumors were quantified and expressed as %ID per 250 mm^3 tumor

(corresponding to the average volume of the tumors used in the HRG and sonopermeation study) (Theek et al., 2018, Theek et al., 2016). In case of the FRI of 100 µm-thick sections, the periphery was defined as a 5-pixel wide outer zone of the slice segmentation (Theek et al., 2018).

The MRI image analysis was as well performed by using the Imalytics Preclinical software. To obtain the signal intensity for kidneys in the T1-weighted TSE images, areas were segmented in the medulla and cortex of each kidney. Contrast to noise ratio (CNR) was calculated according to the following equation: CNR = (ROI - muscle signals)/noise. The muscle signal was assessed in the erector muscle of the spine. Noise was determined as the standard deviation of the air lateral to the mouse body at the level of the kidneys. To estimate the T1 relaxometry based on the R1 map, an exponential curve *beta*abs(0.5-exp(-R1*t))* was fitted to the voxel intensities over time. ΔCNR and ΔR1 were calculated via value post- minus pre- contrast agent injection (Sun et al., 2019).

TPLSM

Image stacks of 50 images with a step size of 1 µm were acquired using a 25× water-immersed objective mounted on the Olympus FV1000MPE multiphoton microscopy system (Olympus, Germany) and processed as described previously (Theek et al., 2016). In each image stack, the fluorescent liposomes, polymers or CNA35 and perfused blood vessels (via rhodamine-lectin staining) as well as collagen I and III fibers (via second-harmonic generation imaging) were imaged. TPLSM images were analyzed using the Imaris Software versions 7.4 and 9.2 (Bitplane AG, Switzerland).

The micro-distribution of the ATTO 488-containing fluorescent polymers or NBD-labeled liposomes, i.e. their extravasation from blood vessels into the tumor interstitium, was analyzed using a modified version of the “Dilate Surface” XTension in Imaris. For this purpose, initial thresholding was applied on the basis of the rhodamine-lectin signal (to create a 3D vessel segmentation). The vessel segmentation was then automatically dilated, at step-sizes of 10, 30 and 50 µm. Finally, the total amount of polymers or liposomes detected within a 50 µm radius around the vessels was quantified by multiplying the relative drug carrier volume and the signal intensity. The relative micro-distribution was calculated by determining the relative amount of carrier material detected in each individual 3D segmentation (Theek et al., 2018, Theek et al., 2016). The

collagen fiber thickness and spacing was calculated using the trabecular thickness feature of the BoneJ plugin in the image processing package Fiji (Doube et al., 2010, Schindelin et al., 2012).

Histology

Immunohistochemistry

Mouse kidney tissues for immunohistochemistry and light microscopy were harvested and fixed in methyl Carnoy's solution and embedded in paraffin. Human archive samples were formalin fixed and paraffin embedded. 1 µm sections were cut and stained as previously described (Boor et al., 2015). Periodic acid-Schiff (PAS) staining was used to assess renal morphology. Stainings against alpha-smooth muscle actin (α-SMA) (Dako, Denmark), PDGFR-β (Abcam, USA), Fibronectin (Merck Millipore, Germany) were performed as described previously (Buhl et al., 2016, Djudjaj et al., 2016, Ehling et al., 2016, Papasotiriou et al., 2015). Collagen type I, III and IV antibodies (Southern Biotechnology Associates, USA) were diluted 1:100 in phosphate-buffer saline containing 1% bovine serum albumin (Sigma-Aldrich, Germany). An anti-goat secondary antibody was purchased from Vector Laboratories (USA). DAB (3,3'-Diaminobenzidine) (Sigma-Aldrich, Germany) was used as HRP substrate and formed a brown precipitate after oxidation. Methyl green (Sigma-Aldrich, Germany) was used for nuclear counterstaining (Sun et al., 2019).

For immunohistochemistry staining against elastin, the samples were deparaffinized and rehydrated, endogenous peroxidase activity was blocked with 3% H_2O_2 in distilled water for 10 min at room temperature. All sections were blocked using the avidin-biotin blocking kit (Vector Laboratories, USA). Polyclonal rabbit anti-elastin antibody (ab21610 for mouse and rat tissue or HPA018111 for human tissue) was used in a dilution of 1:500 and incubated for 2 h. The biotinylated goat anti-rabbit IgG secondary antibody (Vector Laboratories, USA) was diluted 1:300 and incubated for 30 min. Nuclei were counterstained with methyl. All sections were analyzed with the BZ-9000 fluorescence microscope (Keyence, Japan) (Sun et al., 2019).

Stained tissue slides were scanned using the NanoZoomer 2.0-HT digital whole slide scanner (Hamamatsu Photonics, Japan) and analyzed using imaging software NDP.view

(Hamamatsu Photonics, Japan) and the computer based morphometry feature in ImageJ (National Institutes of Health, USA) (Sun et al., 2019).

Fluorescence

8 µm-thick tumor cryosections were fixed with 80% methanol (v/v) aqueous solution for 5 min and afterwards with -20 °C cold acetone for 2 min. Immunofluorescent stainings were performed with the following primary monoclonal antibodies: rat anti-mouse CD31 (PECAM-1) antibody (BD Biosciences, Germany); biotin anti-α-SMA antibody (Progen Biotechnik, Germany); rat anti-mouse F4-80 antibody (AbD Serotec, Germany); and rat anti-mouse CD206/Mrc-1 antibody (Acris Antibodies, Germany). Secondary antibodies were obtained from Dianova (Germany). DAPI (4'-6-diamidine-2'-phenylindole dihydrochloride) (Sigma Aldrich, Germany) was used for nuclear counterstaining and sections were embedded with Mowiol® 4-88 (Roth, Karlsruhe). For the sonopermeation study, cellularity of the A431 and BxPC-3 tumors were assessed by applying a 1:10 mixture of DAPI in Mowiol® 4-88. Images were acquired using the Axio Imager M2 microscopy system (Carl Zeiss AG, Germany).

Double stainings using CNA35-FITC and antibodies against collagen type I, III and IV (Southern Biotechnology Associates, USA) were performed on methyl Carnoy's fixed 1 µm-thick paraffin sections of mouse and human renal tissues. Sections were first incubated with CNA35-FITC overnight at 4°C followed by the incubation with collagen type I (1:100), III (1:100) or IV (1:200) antibodies for 1 h (Southern Biotechnology Associates, USA). Secondary antibodies (Alexa Fluor 647, anti-goat, 1:100) were applied for 30 minutes at room temperature. DAPI (Roche diagnostics, Germany) was used as nuclear counter stain. Stained slides were viewed and photographed with a digital fluorescence microscope (BZ-9000, Keyence, Japan). On 5 µm thick cryosections of renal tissues, from UUO mice injected with CNA35-FITC and sacrificed at 0.5, 4 and 24 h after i.v. administration, a mix of DAPI (1:50, Sigma Aldrich, Germany) in Mowiol® 4-88 (Roth, Germany) was applied for nuclear counterstaining (Baues et al., 2019, Mohammadkhah et al., 2017). Images were acquired using the Axio Imager M2 fluorescence microscopy system (Carl Zeiss AG, Germany).

The immunofluorescence staining against elastin included deparaffinization, rehydration and endogenous peroxidase activity blocking with 3% H_2O_2 in distilled water

for 10 min at room temperature. Afterwards, the sections were treated using the avidin-biotin blocking kit (Vector Laboratories, USA). The polyclonal rabbit anti-elastin antibody (ab21610 for mouse and rat tissue or HPA018111 for human tissue) was diluted 1:500 and incubated for 2 h. The donkey anti-rabbit IgG conjugated with Alexa Fluor 647 (Jackson ImmunoResearch Laboratories, USA) was diluted 1:200 and incubated for 30 min. Nuclei were counterstained with methyl green for immunohistochemistry and DAPI for immunofluorescence. All sections were analyzed with the BZ-9000 fluorescence microscope (Keyence, Japan).

Elastin staining of the patient cohort samples were scored as follows: 0 = positive vasculature and eventually very few elastin spots in perivascular areas; 1 = elastin bundles accumulating around vessels; 2 = larger areas of elastin-bundles around vessels and focal spots in the interstitium; 3 = strong staining of larger areas with perivascular elastin-bundles and multiple focal spots in the interstitium; 4 = massive elastin bundles in the interstitium; 5 = diffuse and strong elastin staining in more than 50% of the interstitium (Sun et al., 2019).

Statistical analysis

Statistical analysis was performed using GraphPad Prism versions 5, 6 and 8. All results are presented as mean ± standard deviation. *In vivo* CT-FMT analysis of polymer accumulation was evaluated with one-way analysis of variance (ANOVA) including a multiple comparisons correction (Bonferroni). *In vivo* CT-FMT analysis of liposome accumulation was analyzed using the paired *t*-test and two-way ANOVA. In case of the sonopermeation and collagen fibrosis imaging study, e*x vivo* 2D-FRI measurements were analyzed using the paired *t*-test, corrected for multiple comparisons. For the HRG experiments, the *ex vivo* FRI analyses were done by applying one-way ANOVA including the Bonferroni correction. Paired *t*-tests were used to compare fibrotic and contralateral kidneys in one animal. The unpaired *t*-test was used for comparison between two groups in the kidney studies. One-way ANOVA followed by Bonferroni correction was used for comparing more than two groups. In the HRG study, US and immunofluorescence analysis were performed using one-way ANOVA including Bonferroni correction. For the polymer penetration analysis in TPLSM, the two-way ANOVA with Bonferroni post-test was applied to investigate the interaction between the groups and the distance from

the vessel surface. In the sonopermeation setting, TPLSM and immunohistochemistry analysis were performed using unpaired *t*-test. Statistical significance was defined as a *p*-value of less than 0.05 (Sun et al., 2019, Theek et al., 2018, Theek et al., 2016).

4. Results

4.1. Vascular priming via macrophage re-education enhances drug delivery

To study the role of HRG-mediated vascular normalization on EPR-mediated tumor targeting of 67 kDa-sized HPMA copolymer-based drug delivery systems, the HRG levels in the three different mouse models, i.e. KO + t241, WT + t241 and WT + t241-HRG$^+$, were analyzed first. Significant differences in the HRG expression were found via immunofluorescence (Figure 5). As expected, the WT + t241-HRG$^+$ group expressed significantly higher levels of HRG in tumors compared to the KO + t241 and WT + t241 groups (Theek et al., 2018).

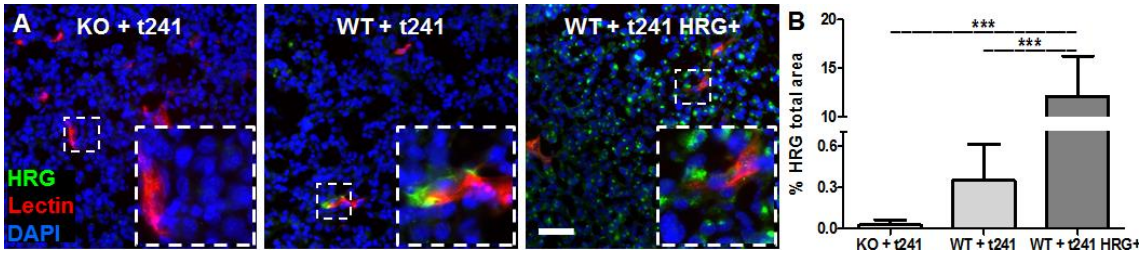

Figure 5: Differences in HRG expression in the tumor tissue of the three used mouse phenotype and t241 cell combinations. (A) Representative fluorescence microscopy images of the HRG expression, which is visualized in green, perfused blood vessels with rhodamine-lectin in red and cell nuclei stained with DAPI (blue). Scale bar: 50 µm. (B) The HRG immunostaining indicates the strongest HRG expression for the HRG-overexpressing t241 tumors in WT mice. Values represent average ± standard deviation based on quantifying n=3-4 sections in n=3-6 different tumors. ***p<0.001 (Theek et al., 2018).

In order to investigate the effect of HRG expression on the tumor vasculature, multiple blood vessel features were characterized via immunofluorescence (Figure 6). The staining of the endothelial cell marker CD31 (platelet-endothelial cell adhesion molecule 1; PECAM-1) showed that the average vessel density was significantly higher in t241 tumors grown in KO mice in comparison to both other groups, the t241 tumors grown in WT mice and the HRG-overexpressing t241 tumors in WT mice (Figure 6B). To examine the blood vessel functionality, the relative fraction of lectin-perfused vasculature was determined. The lectin/CD31 positive fraction in the KO + t241 group was 46 ± 17% (Figure 6C). In the WT + t241-HRG$^+$ group, this double positive area was found to be significantly higher (61 ± 21%), whereas tumor tissue of the WT + t241 group had a lectin/CD31 positive fraction of 58 ± 18%. For the vessel maturity, the pericyte coverage is considered an essential measure. In case of the α-smooth muscle actin (αSMA) staining in tumors grown in WT mice, we observed generally higher levels of αSMA compared to mice lacking the expression of HRG (Figure 6D). The highest αSMA

mean value (0.2 ± 0.1%) was assessed for the WT + t241-HRG^{+} group. This tendency was also reflected in the vessel maturity score (Figure 6E), in which the αSMA/CD31 positive fraction was substantially higher for the WT mice implanted with t241 overexpressing HRG (24 ± 18%) in comparison to the mice and tumor combination, which was missing HRG expression completely (KO + t241 group, 15 ± 11%) (Theek et al., 2018).

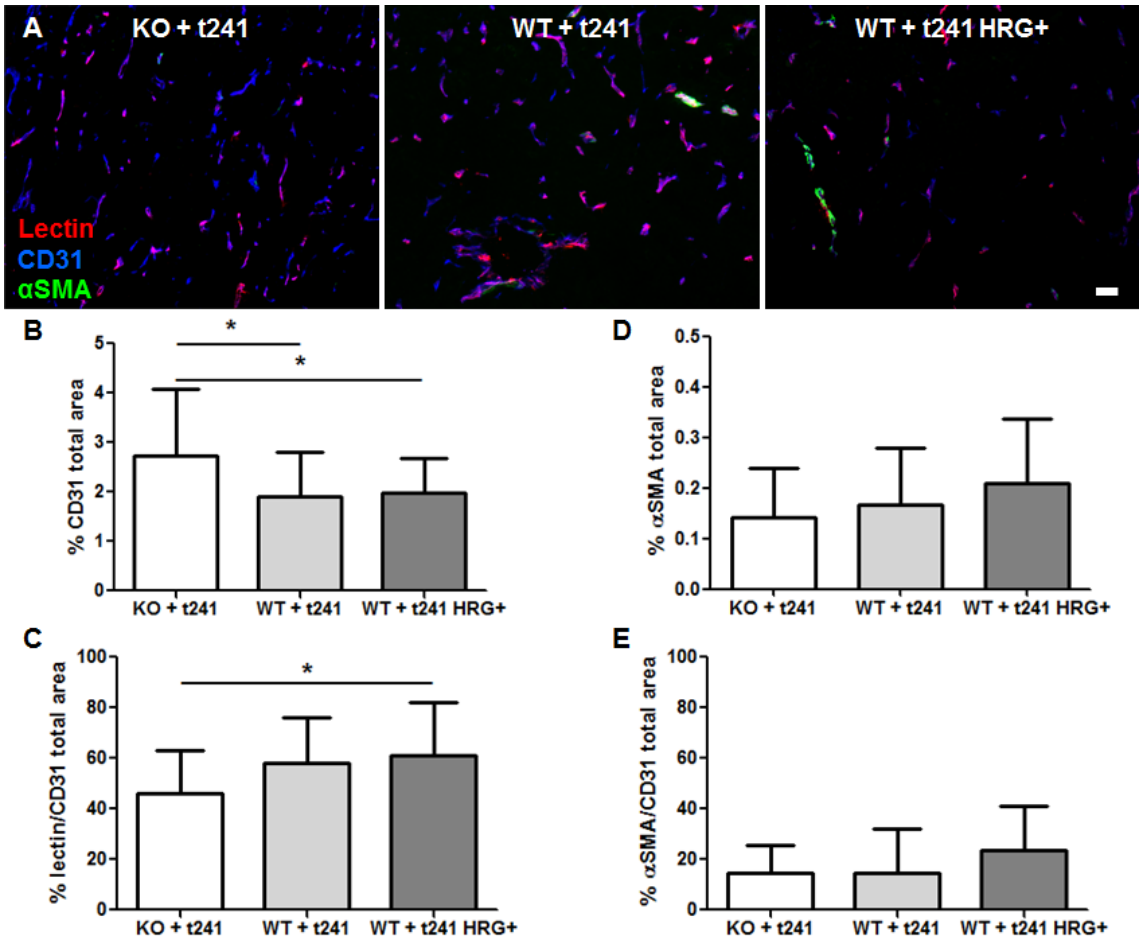

Figure 6: Assessment of the HRG induced changes in the tumor blood vasculature. (A) Representative fluorescence microscopy images of the vasculature in t241 tumor of HRG-KO and WT mice, as well as in HRG-overexpressing t241 tumors, which were excised from WT mice. Endothelial cells are stained with CD31 (blue), perfused blood vessels with rhodamine-lectin (red) and pericytes with αSMA (green). Scale bar: 50 µm. (B) The microvessel density, corresponding to the CD31 positive area fraction, was significantly lower with a higher degree of HRG expression. (C) Vessel functionality, depicted as % of rhodamine-lectin positive area / CD31 positive vessel area, increased with HRG presence. (D, E) Quantification of the pericyte marker αSMA showed a tendency towards more mature blood vessels, when HRG levels were elevated. Values represent average ± standard deviation based on quantifying n=4 sections in n=3-6 tumors. *p<0.05 (Theek et al., 2018).

The subsequent assessment of the quantity and polarization status of tumor-associated macrophages (TAM) was done via staining the murine macrophage marker F4-80 and the macrophage mannose receptor-1 (Mrc-1), which is specifically expressed by pro-angiogenic M2-like macrophages (Figure 7A). As shown in Figure 7B and C, no

significant differences in the overall number of TAM were observed in the three different groups. In t241 tumors grown in HRG-knockout mice, however, a significantly higher fraction of the Mrc-1-positive M2-like macrophages (65 ± 17%) was detected than for the WT + t241-HRG$^+$ group (52 ± 17%) (Theek et al., 2018).

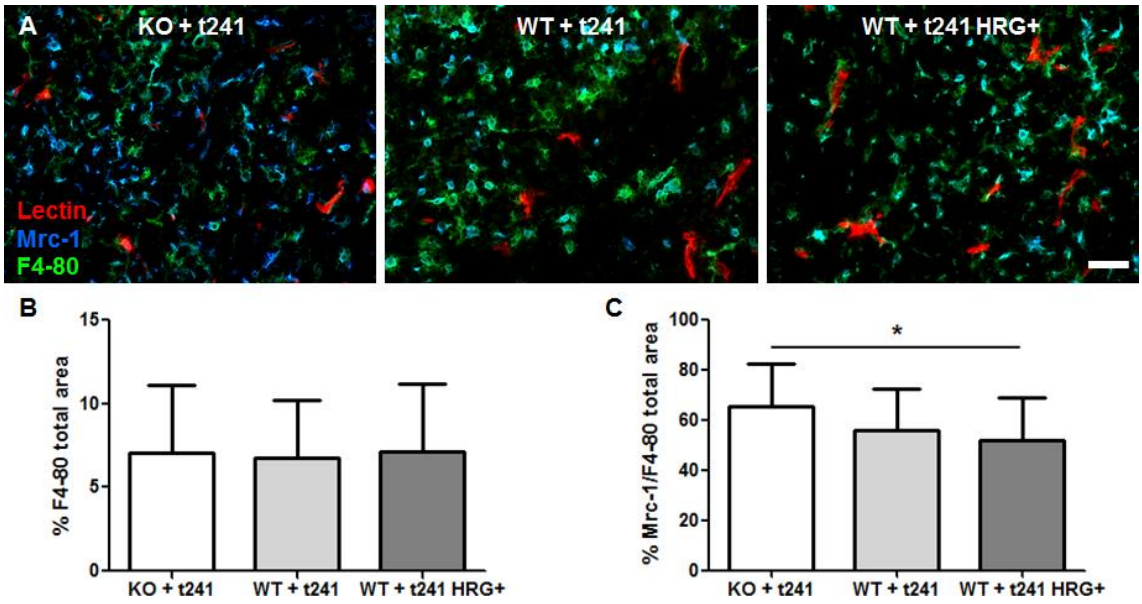

Figure 7: The effect of HRG expression on the tumor-associated macrophages. (A) Representative fluorescence microscopy images of lectin-stained perfused blood vessels (red), of tumor-associated macrophages (TAM; via F4-80$^+$ staining, depicted in green) and of pro-angiogenic M2-like TAM (via Mrc-1$^+$ staining, depicted in blue). Scale bar: 50 µm. (B, C) The F4-80 and Mrc-1 staining revealed similar amounts of TAM for the three groups (B), but a significantly higher ratio of Mrc-1$^+$ pro-angiogenic M2-like TAM in tumors characterized by low levels of HRG (C). Values represent average ± standard deviation based on quantifying n=4 sections in n=3-6 tumors. *p<0.05 (Theek et al., 2018).

To investigate the effect of HRG-mediated vascular priming on the tumor accumulation of 10-20 nm-sized polymeric drug carriers, hybrid CT-FMT imaging was performed (Figure 8A). In agreement with the previous findings on the vascular normalization status, the maximum value for polymer accumulation was found in the WT + t241-HRG$^+$ group, with 2.0 ± 0.6% of the injected dose (ID) per 250 mm^3 tumor 48 h after the i.v. injection of the polymers (Figure 8B). A moderate nanocarrier accumulation was detected in the tumors of the WT + t241 group, with 1.8 ± 1.1% ID per 250 mm^3. For the most angiogenic combination, i.e. KO + t241, the least efficient tumor accumulation was determined, with 1.2 ± 0.2% ID per 250 mm^3. Subsequently, *ex vivo* 3D-FMT and 2D-FRI measurements (Figure 8C-H) were performed to confirm the *in vivo* results. The polymer accumulation was significantly improved for the WT + t241-HRG$^+$ combination, with values being up to 70% higher ($p<0.05$), as compared to the KO + t241 group. FRI on 100 µm-thick tissue sections made it possible to differentiate between a peripheral and

a core zone of the tumor and it revealed the highest polymer accumulation in the peripheral zone of HRG-overexpressing tumors (Figure 8G, H) (Theek et al., 2018).

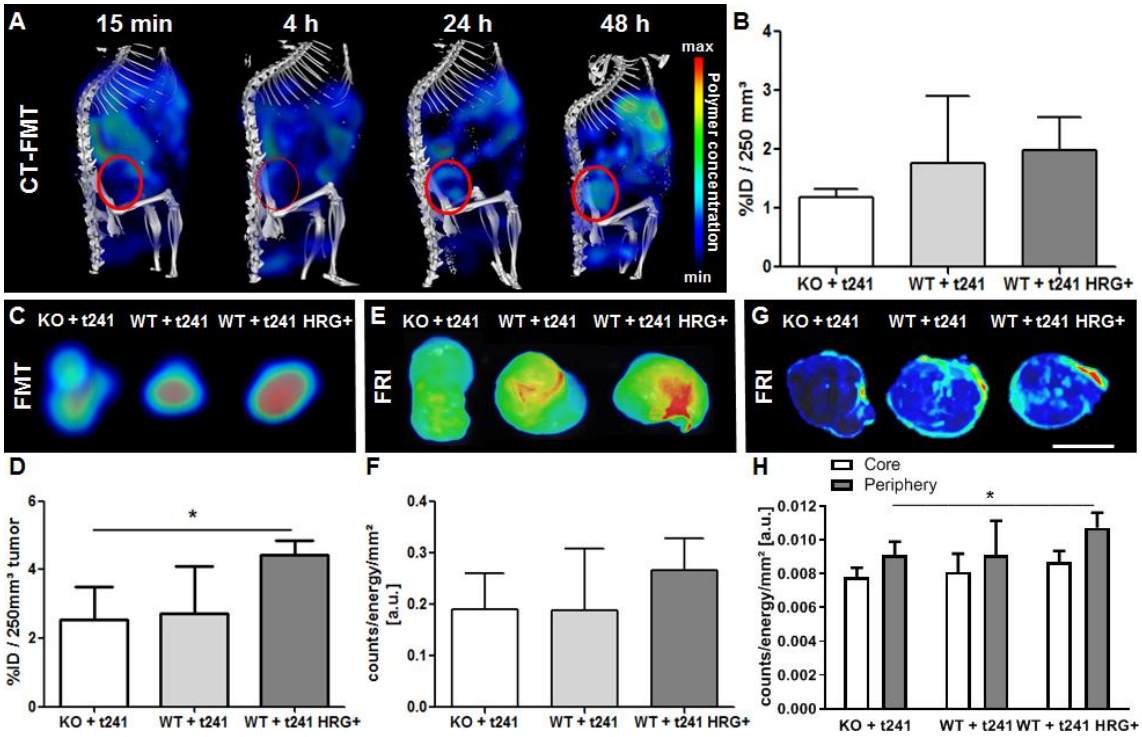

Figure 8: *In vivo* and *ex vivo* imaging of the effect HRG has on the tumor accumulation of polymers. (A) Representative CT-FMT images of polymer accumulation in a WT mouse bearing a t241 tumor at several different time points after i.v. injection. The tumor region on the right flank is encircled in red. (B) Quantification of the tumor accumulation of the polymeric drug carrier at the final measurement time point 48 h post i.v. administration in KO and WT mice implanted with t241 tumors and in WT mice injected with HRG-overexpressing t241 tumors. The evaluation indicated a tendency toward higher accumulation in tumors with normalized blood vessels. (C-F) *Ex vivo* FMT (C, D) and FRI (E, F) images plus the respective quantifications revealed a higher polymer accumulation in tumors expressing higher levels of HRG. (G, H) FRI analysis of 100 µm-thick sections of these tumors, demonstrated improved polymer accumulation particularly in the periphery of tumors expressing higher amounts of HRG. Values represent average ± standard deviation of n=3-6 tumors. Scale bar: 5 mm. *p<0.05 (Theek et al., 2018).

Besides improving the tumor accumulation of polymers macroscopically, HRG-mediated vascular priming was also assumed to affect the extravasation of polymers from the vasculature into the tumor interstitium. In addition, the impact on the local distribution pattern inside the tumor had to be assessed. The polymer penetration depth was analyzed using fluorescence and two-photon scanning microscopy (TPLSM). The microscopic polymer accumulation was analyzed with standard (2D) fluorescence microscopy (Figure 9A). The quantification indicated that the normalization of the blood vessel network was proportionally related to the polymer accumulation (Figure 9C). The polymer-positive area percentage was in tumors of the WT + t241 HRG^{+} group (0.5% for

488 nm; 0.8% for 750 nm) more than twice as high compared to the accumulation for the KO + t241 combination (0.2% for 488 nm; 0.3% for 750 nm).

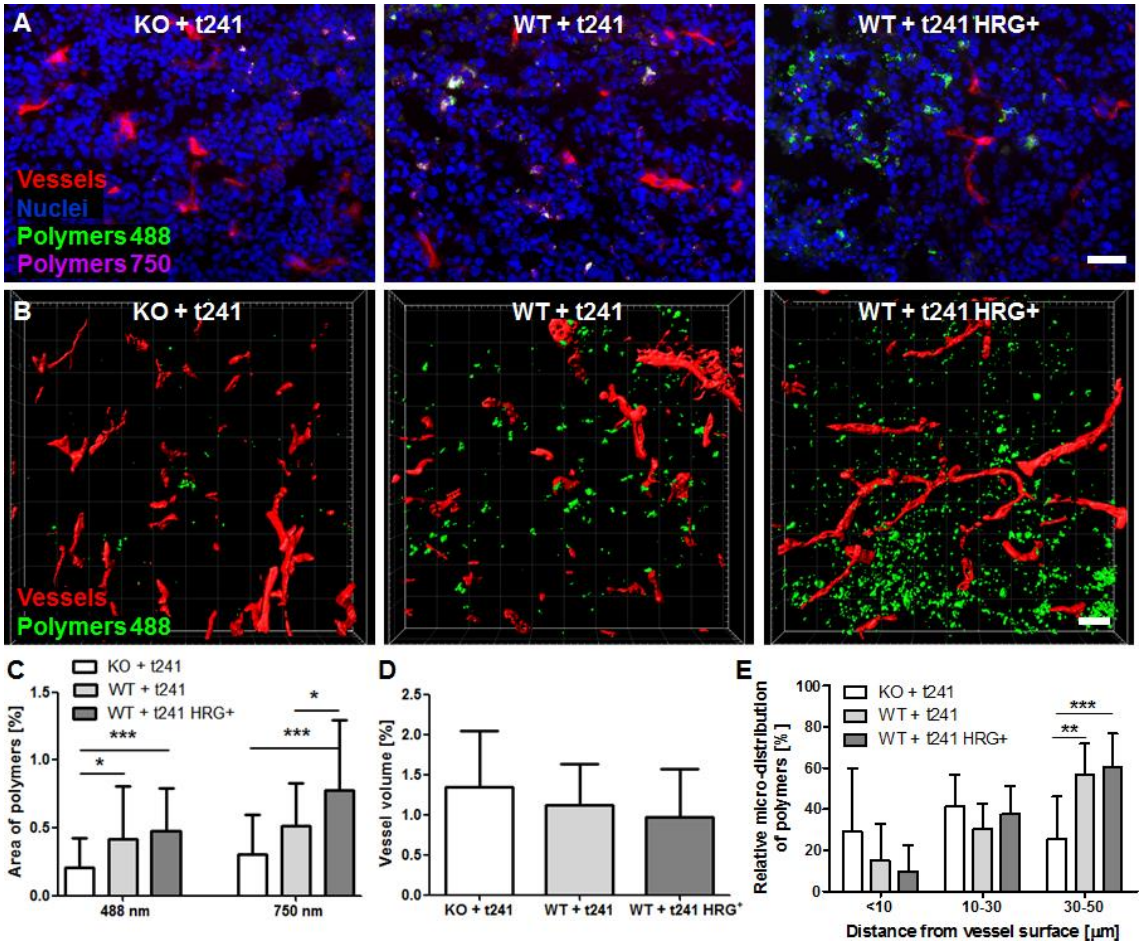

Figure 9: Effect of HRG-mediated vascular priming on the tumor penetration of polymeric drug carrier. (A) Exemplary immunofluorescence images showing the amount of blood vessels (red), cell nuclei (blue), ATTO 488-labeled (green) and Alexa-750-labeled (violet) polymers. Scale bar: 50 µm. (B) Surface-rendered two-photon laser scanning microscopy (TPLSM) image stacks with perfused blood vessels depicted in red and polymers in green. Scale bar: 50 µm. (C) A good correlation between the accumulation of polymers labeled with ATTO 488 and Alexa-750 was observed in both cases, indicating that polymer accumulation increases as a result of HRG-mediated vascular normalization. (D) TPLSM-based quantification indicates a tendency towards a reduced blood volume upon HRG-mediated vascular normalization. (E) The penetration of polymers out of the blood vessels deep into the tumor interstitium significantly increases as a result of HRG-mediated vessel priming. Values represent average ± standard deviation based on quantifying n=3-4 sections in n=3-6 different tumors. *p<0.05, **p<0.01, ***p <0.001 (Theek et al., 2018).

TPLSM allowed the visualization and quantification of the polymer distribution and penetration in a three-dimensional approach (Figure 9B). In agreement with the previous microscopic analysis, the volume of rhodamine-lectin-perfused vasculature decreased upon HRG-mediated macrophage polarization (Figure 9D). Importantly, the TPLSM evaluation of polymer distribution within 50 µm around the tumor blood vessels revealed that primed vessels improved the polymer penetration depth substantially

(Figure 9E). In the KO + t241 group the relative polymer accumulation in the tumor tissue located 30-50 µm away from the nearest blood vessel was only half as high as the polymer volume for the WT + t241 HRG^+ and WT + t241 combinations (Theek et al., 2018). These results illustrated the impact of macrophage-mediated vascular priming in tumors on the biodistribution of a 67 kDa-sized HPMA copolymer based drug delivery system.

4.2. Sonopermeation improves liposome delivery into tumors with low EPR

Passive drug targeting to tumors relies on the highly variable EPR effect, which makes effective delivery challenging and precludes sufficient therapy. Sonopermeation, which is the combined application of US and MB, is able to make the tumor tissue more accessible for the accumulation and penetration of liposomes. The impact of sonopermeation on the distribution of double-fluorophore–labeled liposomes was evaluated, using different types of MB (phospholipid soft-shelled and polymeric hard-shelled), in two tumor models characterized by low levels of EPR (the extreme cellular epidermoid A431 and the highly stromal pancreatic carcinoma BxPC-3).

Hybrid CT-FMT imaging was performed to assess the influence of sonopermeation on the longitudinal biodistribution of liposomes *in vivo* (Figure 10A-B). The highest accumulation values were detected 24 h after the sonopermation in the A431 + PBCA group, with 2.3±0.7% ID per 250 mm^3 tumor, and for the BxPC-3 + MM combination, with 1.9±0.3% ID per 250 mm^3 tumor tissue. In the respective control groups the tumor accumulation remained significantly lower, with 1.3% ID in each (Figure 10C-F). However, for the other two sonopermation-treated comparisons, i.e. A431 + MM and BxPC-3 + PBCA, general tendencies toward enhanced liposome accumulation were detected (Theek et al., 2016).

2D-FRI acquisition of excised control and sonopermeated A431 and BxPC-3 tumors confirmed the enhancement on the tumor accumulation of liposomes (Figure 11). For the majority of tumors, the 2D-FRI results reflected the *in vivo* observed positive effect of sonopermeation on the liposome accumulation. Increases of 20-50% are detected in both A431 treatment combinations as well as in the BxPC-3 + PBCA group (Figure 11B).

In order to investigate the observed differences in macro-accumulation of liposomes further, the phenotypic properties of the two tumor models were characterized in more detail (Figure 12). For the evaluation, histological features, such as vessels, collagen fibers and nuclei, were assessed using TPLSM (Figure 12A, C-E) and fluorescence microscopy (Figure 12B, F). Functional blood vessels are stained via i.v. injection of rhodamine-lectin. The relative blood volume (rBV) determined for A431 tumor sections was comparably low with just 1.8%, whereas in BxPC-3 an almost 50% higher rBV value of 2.7% was estimated (Figure 12A, C).

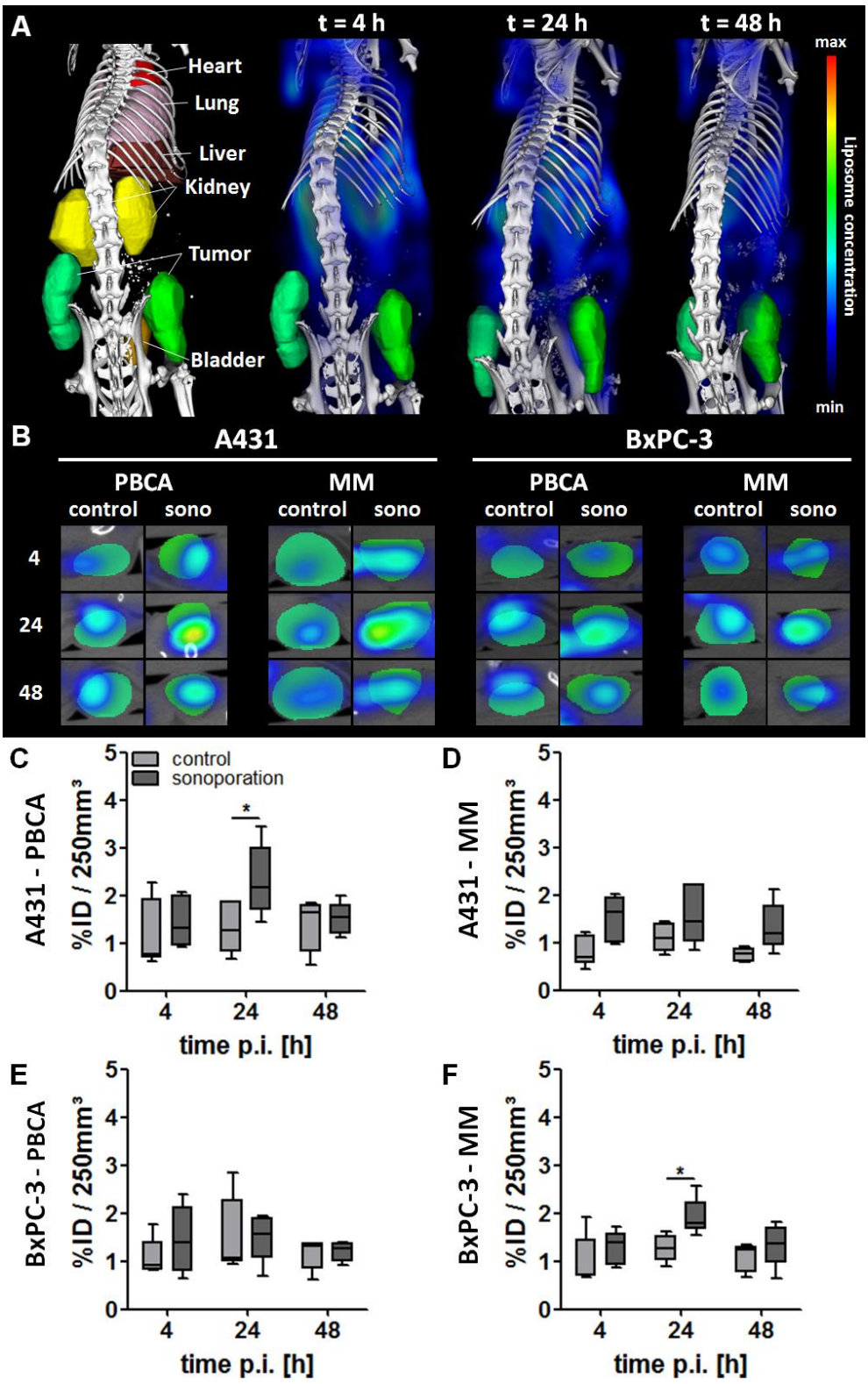

Figure 10: Characterizing the *in vivo* tumor accumulation of liposomes upon sonopermeation. (A) Representative 3D CT-FMT images of segmented tissues and the fluorescent overlap of the liposome distribution in one mouse over time. (B) Transversal slice through a control (left) and the respective sonopermeated tumor (right). (C-F) The evaluated liposome accumulation for both A431 and BxPC-3 tumors upon sonopermeation with either type of MB, indicated a general tendency toward an enhanced accumulation when sonopermeation was applied. Significant differences were observed only at 24 h p.i. for the combination A431 + PBCA and BxPC-3 + MM. *p<0.05 (Theek et al., 2016).

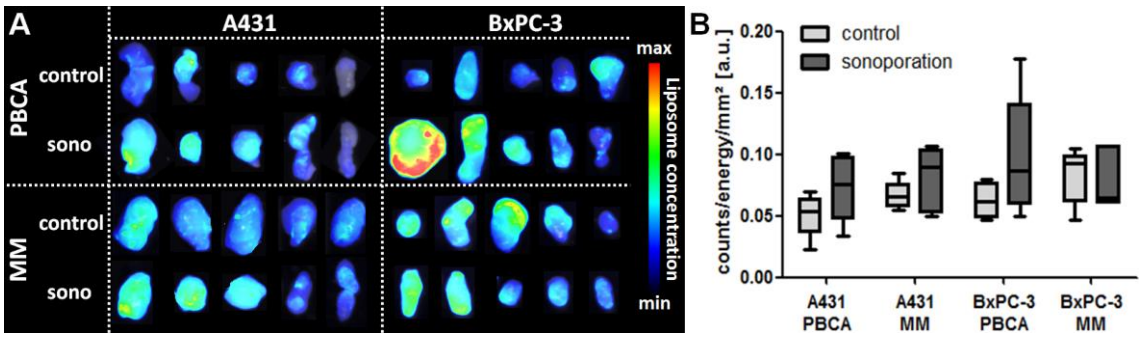

Figure 11: *Ex vivo* optical imaging of the tumor accumulation of liposomes. (A) FRI imaging of excised control and sonopermeation-treated A431 and BxPC-3 tumors confirmed the trend of increased liposome accumulation upon sonopermeation. (B) The quantification of the mean signal intensity of the liposome accumulation also indicated a high variability in between the groups (Theek et al., 2016).

The collagen type I and III content detected by means of second harmonic generation (SHG) was only 3% in A431 (Figure 12D), half of the fibers were found in close proximity (<50 µm) to the blood vessels (Figure 12E). In the BxPC-3 samples, 6 times more collagen was present, which was furthermore closely surrounding the vasculature (Figure 12D, E). On the other hand, the nuclear staining with DAPI revealed an immense cellular density for the A431 tumors (Figure 12B, F).

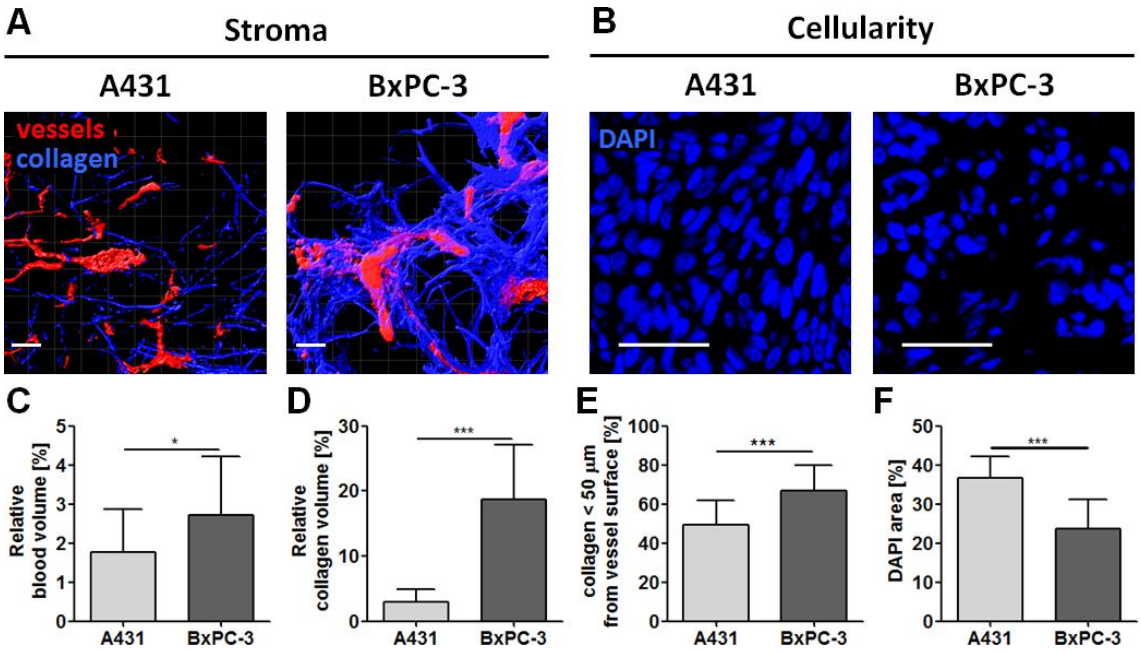

Figure 12: Histological evaluation of the tumor stroma and cellularity. (A) Representative TPLSM images of A431 and BxPC-3 tumor sections showing rhodamine-lectin-perfused blood vessels (red) and collagen fibers generated by SHG (blue). (C-E) Corresponding quantification of the relative blood volume (C), the stromal collagen content (D) and fiber distribution (E) revealed significant differences in between both tumor models. (B, F). Nuclear staining (blue) of tumor sections with DAPI visualized the differences in cellular density (B), the analysis revealed significantly higher values for the A431 tumors (E). *p<0.05, ***p<0.001 Scale bars: 50 µm (Theek et al., 2016).

In addition to these tumor type specific microenvironmental characteristics, the stromal differences in regard to collagen fiber structures of A431 and BxPC-3 were quantified in detail (Figure 13). The fiber thickness is a key feature of the collagen morphology, as a dense ECM is considered a main limiting factor in the context of sufficient drug delivery. Collagen fibers in A431 sections were thin (max. 5 µm) and evenly distributed, while in BxPC-3 the fibers were arranged to thick bundles of threefold the diameter and unequally distributed over the section (Figure 13). The provided insight on the tumor microenvironment (i.e. relative blood volume, collagen content and cellularity) was fundamental for the systematic analysis of sonopermeation effects, especially in regard to the following liposome penetration analysis (Theek et al., 2016).

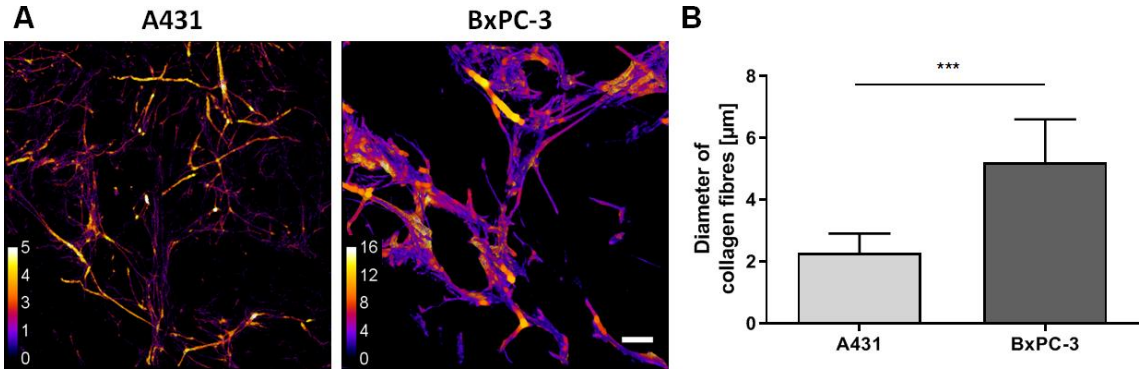

Figure 13: Characterization of the collagen fiber thickness differences. (A, B) Collagen fibers type I and III vary significantly in their location and bundle arrangement in between the two tumor models, A431 and BxPC-3. *p<0.05, ***p<0.001. Scale bar: 50 µm (Theek et al., 2016).

The micro-distribution and tissue penetration of liposomes is tremendously influenced by the characteristics of the tumor microenvironment. The combination of TPLSM and semi-automated image analysis allowed to evaluate the liposome localization upon sonopermeation. The fluorescent signal of the liposomes was visualized and quantified within a radius of 50 µm from the perfused blood vessels, thereby the distance was subdivided into three segments. The different fractions were less than 10 µm, 10-30 µm and 30-50 µm, respectively, far away from each individual segmented vessel surface. For untreated, control A431 tumors approximately two-third (67%) of the liposomes were localized in the first compartment, in direct proximity to the vasculature (Figure 14). By means of sonopermeation, the concentration of liposomes in direct vicinity to the vessels was decreased to 53% (PBCA) and 46% (MM). Therefore, higher amounts of liposomes were detected in greater distance to the vasculature for both PBCA and MM:

within the 10-30 µm segment the liposome penetration enhanced by 8%, while in the 30-50 µm area the liposome amount doubled (Theek et al., 2016).

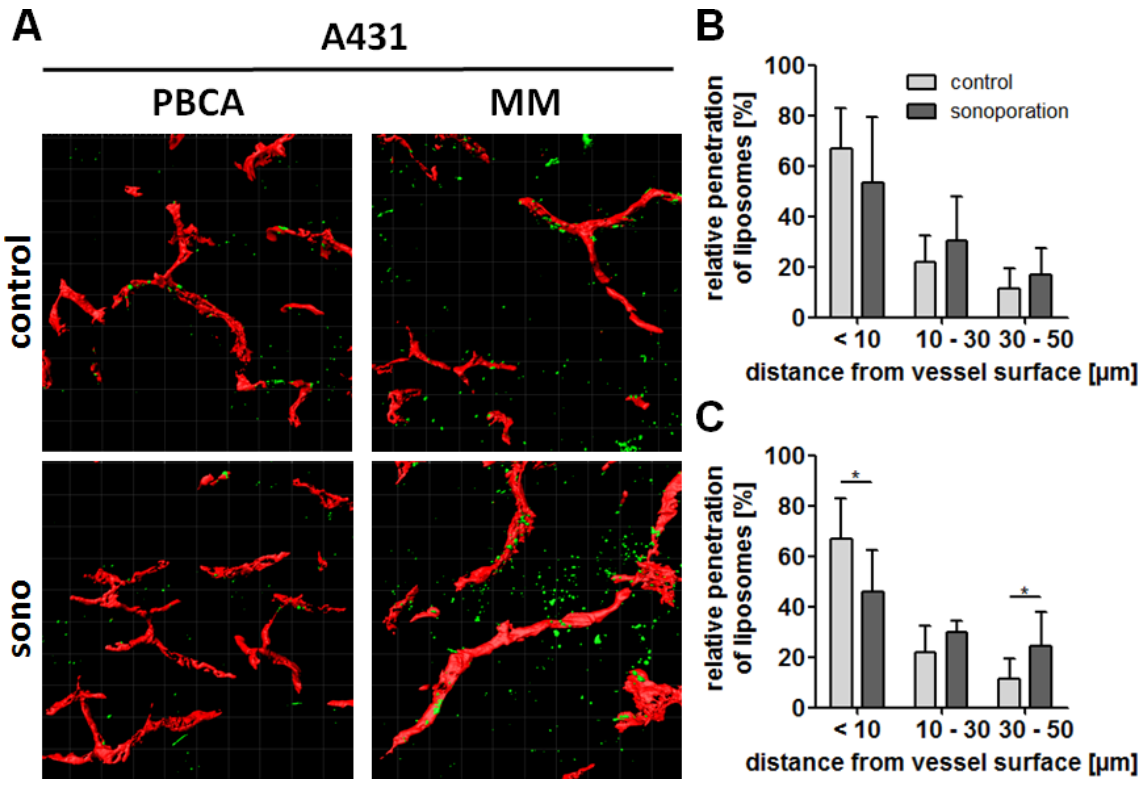

Figure 14: Sonopermeation improves the penetration of liposomes in A431 tumors. (A) Exemplary TPLSM images showing blood vessels (red), and liposomes (green) in control and sonopermeated A431 tumors. (B, C) The relative distribution of liposomes is analyzed for the sonopermeation with PBCA (B) and MM (C) microbubbles. *p<0.05 (Theek et al., 2016).

For the collagen-rich BxPC-3 samples the native liposome penetration without sonopermeation is even lower than in A431 tumors (Figure 15). Practically 80% of the liposomes were stuck next to the vasculature. When sonopermeation was applied, liposomes were able to penetrate significantly further into the interstitium. In case of PBCA MB 18% less liposomes were detected within the distance of 10 µm to the vasculature (Figure 15B), for MM the amount of liposomes in this area closest to the vessels was reduced by 15% (Figure 15C). Overall, the accumulation and penetration of liposomes in tumors with low EPR was enhanced by means of sonopermeation, with either soft- or hard-shelled MB (Theek et al., 2016).

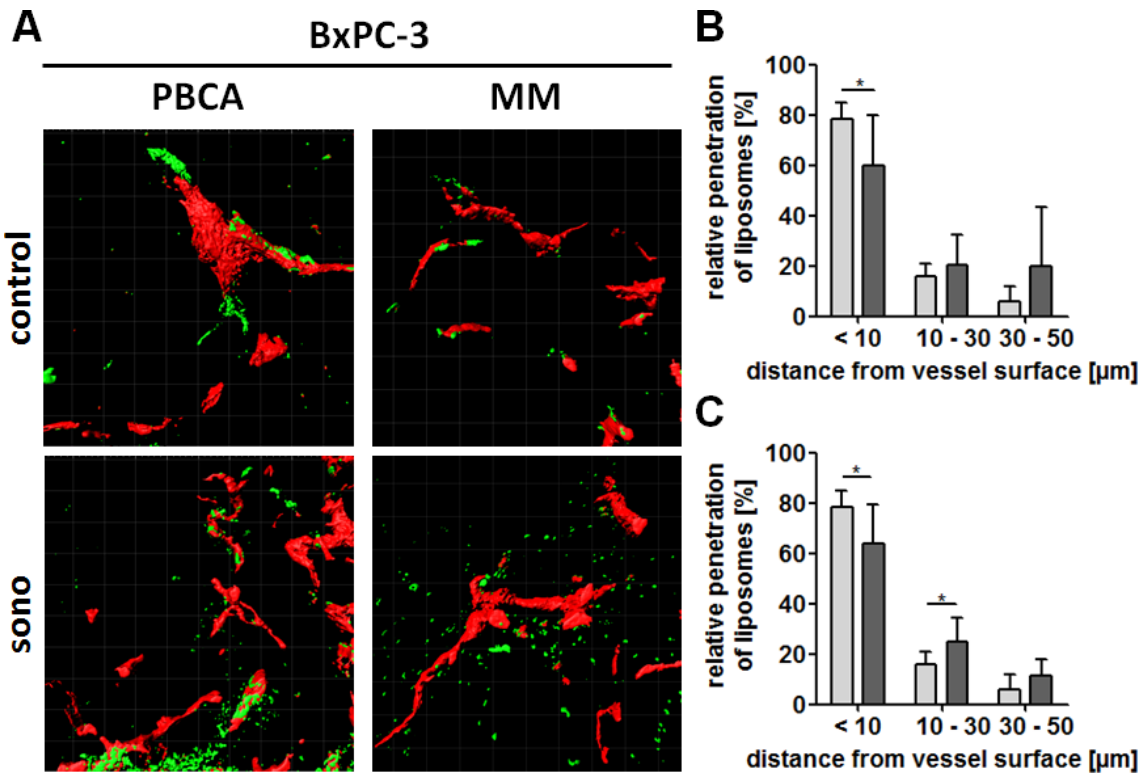

Figure 15: Enhanced liposome penetration into the interstitium of BxPC-3 tumors upon sonopermeation. (A) Representative TPLSM surface-rendered image stacks of BxPC-3 tumors with perfused blood vessels displayed in red and liposomes shown in green. (B, C) Improved relative distribution of liposomes in different tumor compartments upon sonopermeation with PBCA (B) and MM (C) microbubbles. *p<0.05 (Theek et al., 2016).

4.3. Collagen as an imaging biomarker of renal fibrosis

The pathological production of ECM components, like collagen fibers, is a hallmark of renal fibrosis. Multimodal optical imaging was employed to visualize and quantify this deposition using the collagen-binding agent CNA35 in two murine models of kidney fibrosis. After the i.v. injection of 1 nmol Cy7-labeled CNA35, longitudinal CT-FMT imaging showed significantly higher CNA35 accumulation in the kidney with I/R-induced fibrosis (Figure 16A, B). In regard to the overall biodistribution, off-target accumulation of CNA35 was observed in liver and spleen, which likely results from capture and clearance by the reticuloendothelial system (Figure 17A). However, similar findings for the *in vivo* accumulation were observed, when a higher dose of 5 nmol CNA35 was applied (Figure 17B, C) (Baues et al., 2019).

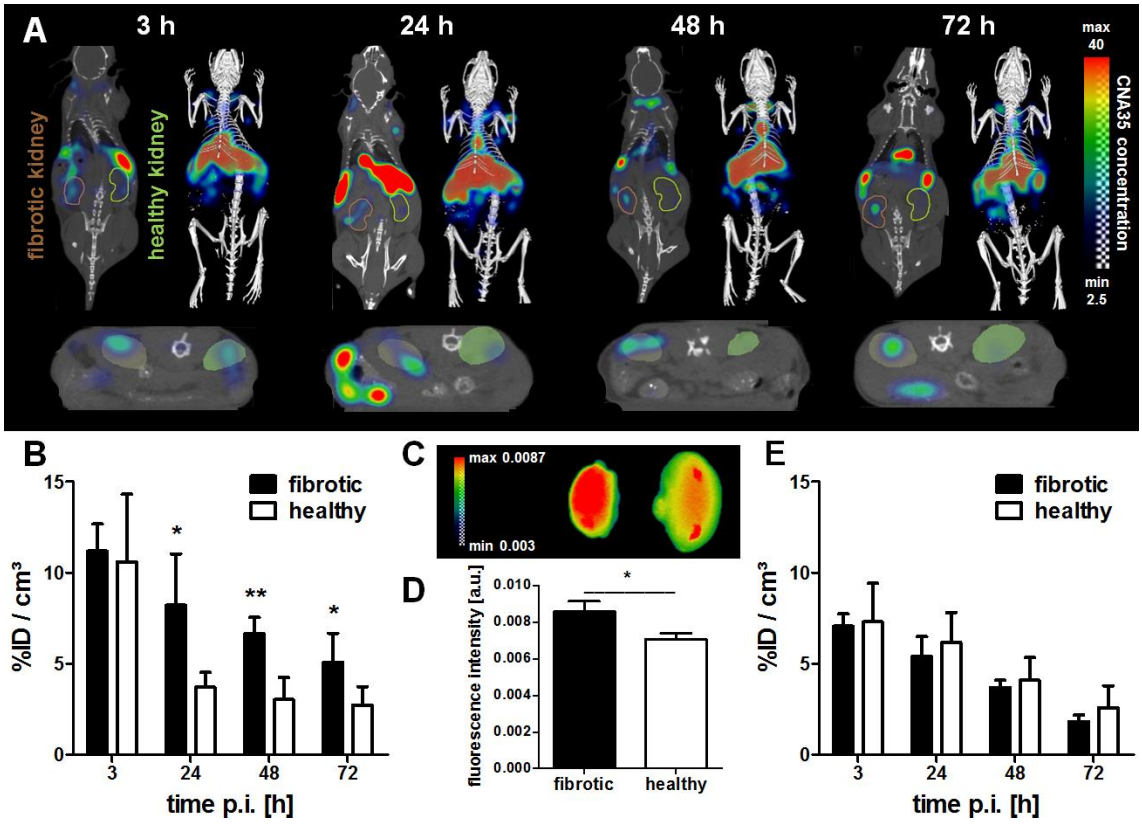

Figure 16: *In vivo* and *ex vivo* optical imaging of collagen deposition kidneys with I/R induced fibrosis using CNA35-Cy7. (A) Coronal and transversal slices as well as 3D renderings for hybrid computed tomography fluorescence molecular tomography (CT-FMT) imaging of CNA35 biodistribution in a mouse with I/R-induced renal fibrosis at different time points after the i.v. injection of 1 nmol CNA35-Cy7. The fibrotic kidney is encircled in brown (left) and the healthy kidney in green (right) in the 2D view. (B) Quantification of the *in vivo* CT-FMT images shows prominent accumulation of CNA35-Cy7 in fibrotic kidneys at 24, 48 and 72 h after probe administration. (C, D) *Ex vivo* fluorescence reflectance imaging (FRI) at 72 h post injection confirms higher CNA35 accumulation in fibrotic kidneys (left). (E) Quantification of the kidney accumulation of scrambled CNA35-Cy7, demonstrating no specific accumulation in fibrotic vs. healthy kidneys. Values represent mean ± SD based on quantifying n=4 mice. *p<0.05, **p<0.01 (Baues et al., 2019).

The *ex vivo* FRI acquisition confirmed the *in vivo* findings for CNA35-Cy7, showing significantly increased probe retention in fibrotic kidneys compared to the healthy controls, for both the 1 nmol (Figure 16C, D) and 5 nmol (Figure 17D, E) dose. To demonstrate that CNA35 specifically targets collagen in fibrotic kidneys, we injected a Cy7-labeled scrambled version of CNA35. The scrambled CNA35 version is not able to bind to collagen fibers due to a change in the amino acid sequence at the binding site. As opposed to CNA35-Cy7, the scrambled probe did not specifically accumulate in fibrotic kidneys and it was cleared equally fast from both kidneys (Figure 16E).

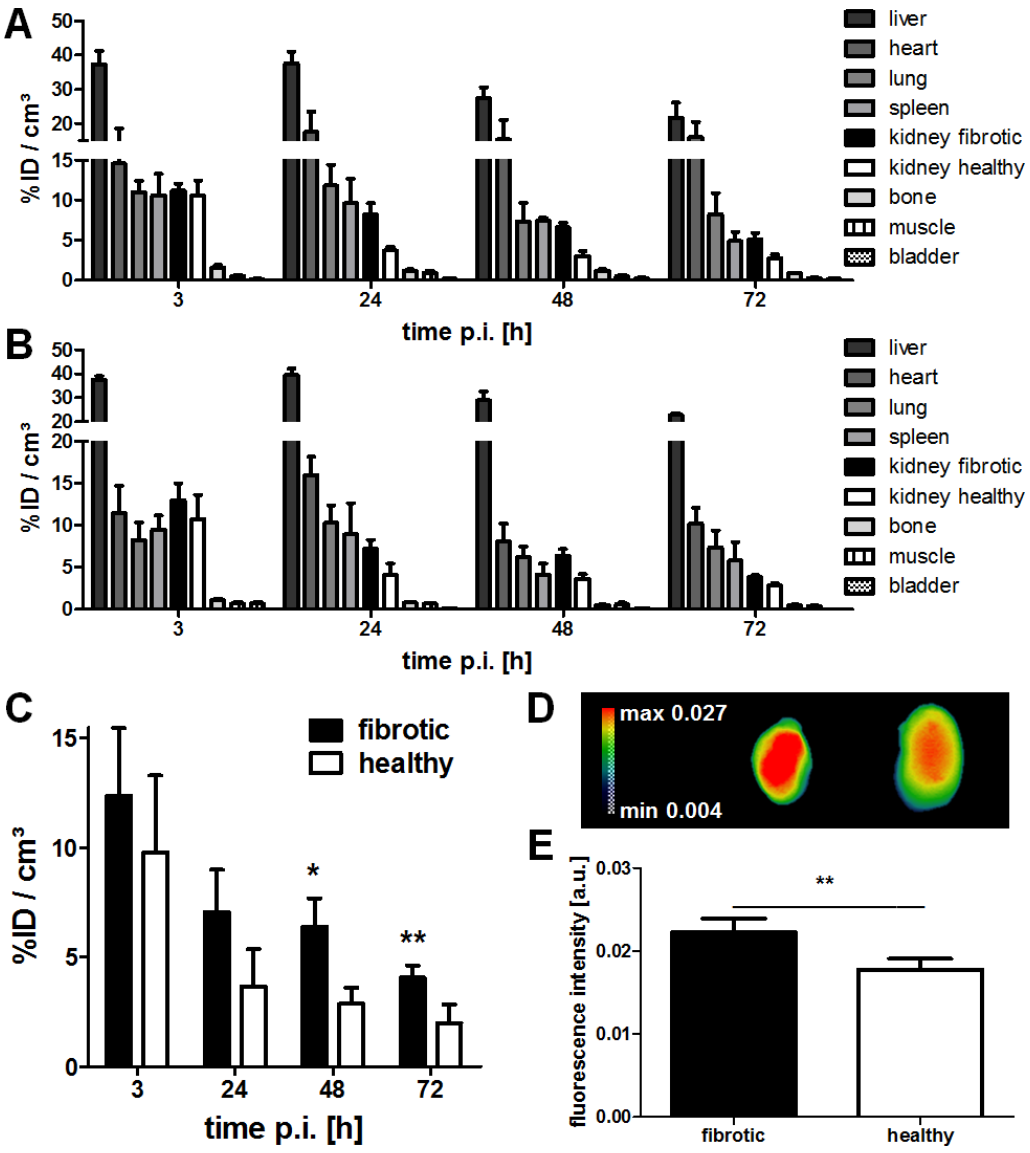

Figure 17: Optical imaging of collagen deposition in renal fibrosis using Cy7 fluorophore-labeled CNA35. (A-C) Biodistribution of CNA35 over time in mice after i.v. injection of 1 nmol (A) or 5 nmol (B) on day 14 after unilateral I/R. Hybrid CT-FMT imaging indicated a significantly higher accumulation of CNA35 in fibrotic kidneys compared to the healthy kidneys, when 5 nmol are administered (C). (D, E) *Ex vivo* FRI analysis 72 h post injection confirmed the *in vivo* findings for the 5 nmol injection. Values represent mean ± SD based on quantifying n=4 mice. *p<0.05, **p<0.01 (Baues et al., 2019).

For the microscopic confirmation of the collagen-binding specificity of CNA35, co-stainings with FITC-labeled CNA35 and different types of collagen were performed on renal tissue sections from healthy and UUO mice (Figure 18). CNA35-FITC showed high co-localization with the scar type collagens I and III in fibrotic mouse kidneys, but overlapped minimally with the basement membrane collagen type IV (Figure 18A). *Ex vivo* analyses of renal tissues from UUO mice, injected with CNA35-FITC and sacrificed after 0.5, 4 or 24 h post i.v. administration, confirmed the specificity of the contrast agent, showing significantly stronger accumulation in fibrotic than in healthy kidneys (Figure 18B-D), and a staining pattern that clearly reflected perivascular and specific binding to fibrillar collagen (Figure 18D). In this TPLSM-based characterization the specific binding to collagen fibers of type I and III was visualized via SHG. The CNA35 distribution in the kidneys overlapped with collagen and demonstrated a specific binding beyond the perivascular area. Molecular imaging of collagen using CNA35 enabled specific non-invasive quantification of renal fibrosis (Baues et al., 2019).

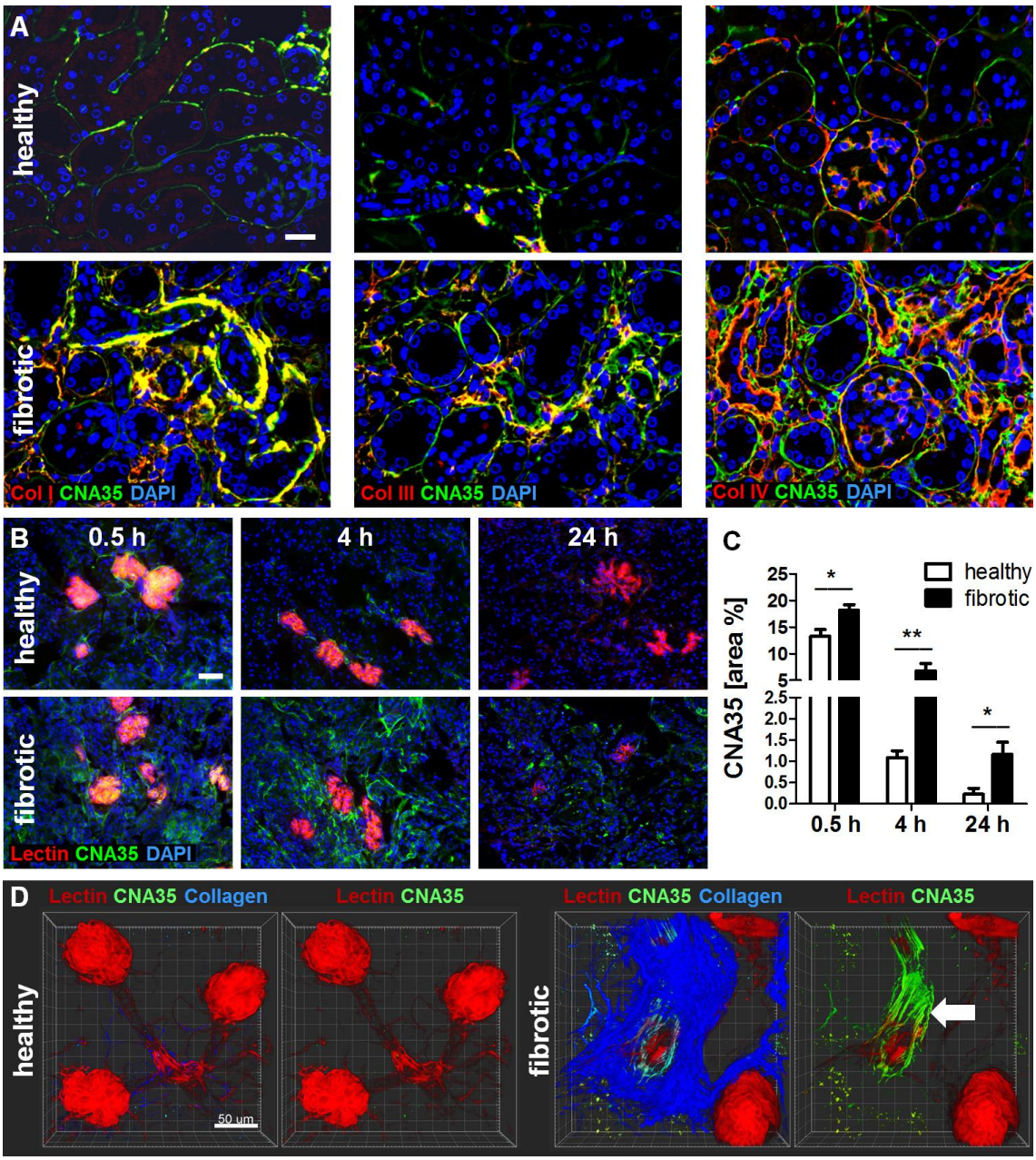

Figure 18: Microscopy imaging of collagen deposition in fibrotic kidneys using CNA35-FITC. (A) Fluorescence microscopy analysis showing the co-localization of FITC-labeled CNA35 (green; upon incubation of tissue sections) with collagen fibers of type I, III and IV (all in red) in renal tissue from healthy mice and UUO mice. Nuclei are counterstained using DAPI (blue). (B) Representative immunofluorescence images showing the accumulation of FITC-labeled CNA35 (green) in healthy and fibrotic kidneys at 0.5, 4 and 24 h after i.v. injection. Perfused blood vessels are counterstained using rhodamine-lectin (red), cell nuclei using DAPI (blue). (C) Quantification of CNA35-FITC accumulation in fibrotic vs. healthy kidneys upon i.v. injection. (D) Two-photon laser scanning microscopy (TPLSM) indicated specific co-localization with collagen fibers (visualized using second harmonic generation) and much stronger enrichment of CNA35-FITC in fibrotic kidneys than in contralateral healthy kidneys, particularly around blood vessels (arrow). Scale bars: 50 µm. Values represent mean ± SD based on n=6 sections. *p<0.05, **p<0.01 (Baues et al., 2019).

4.4. Elastin imaging enables noninvasive staging and treatment monitoring

The best predictor for CKD progression is the assessment of fibrosis, since it is a common endpoint in CKD. Fibrogenesis is characterized by disease state-specific ECM composition, which makes molecular imaging agents that specifically recognize ECM proteins, such as elastin, most suited for diagnosis, staging and treatment monitoring in renal fibrosis. Based on these notions, the elastin expression was analyzed in several rodent models with progressive fibrosis and in patients suffering from multiple kidney diseases at various CKD stages (Sun et al., 2019).

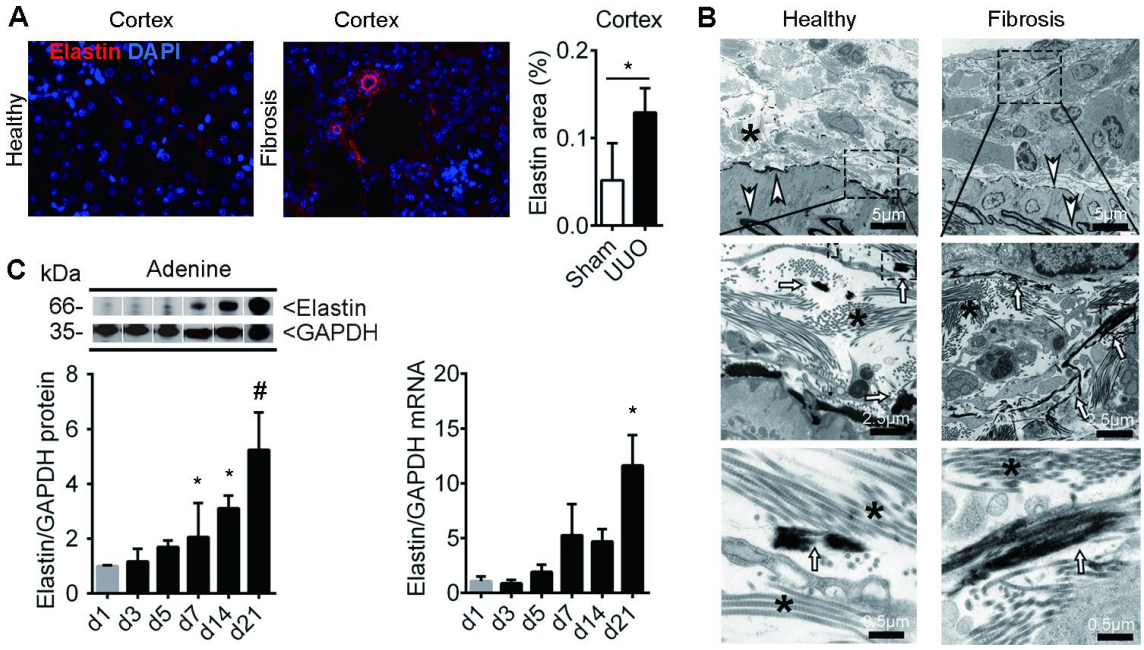

Figure 19: Elastin expression is increased in renal fibrosis. (A) Representative elastin immunofluorescence staining in healthy and fibrotic kidneys showing increased elastin deposition in fibrosis for the rat UUO model. Quantification of elastin positive area in the cortex showed significant increase during fibrosis. (B) Transmission electron microscopy displayed that elastin is mainly located in vessel walls (arrowhead). The region enclosed by the dashed box is shown at a higher magnification. Discontinued and rigid elastin fibers (open arrow) can be seen in the interstitium between collagen bundles (asterisk). (C) Time-course study of elastin expression, at protein and mRNA level, using Western blot and qRT-PCR during progression of renal fibrosis. Both methods further confirmed the significant upregulation of elastin in fibrosis in the murine model of adenine nephropathy. *p<0.05, #p<0.0001 (Sun et al., 2019).

The elastin expression was evaluated in samples from healthy and fibrotic mouse, rat and human kidneys, applying immunofluorescence, immunohistochemistry, transmission electron microscopy (TEM) as well as determining the mRNA and protein concentration. Independent of the species, the elastin expression in healthy tissue was confined to arterial blood vessels and focally to the medullary interstitium. Elastin was neither detected in the cortical interstitium nor associated with tubular or glomerular

cells. On the contrary, in fibrosis the expression of elastin was elevated (Figure 19A). In between collagen bundles, TEM revealed large elastin fiber clusters in the interstitium and within as well as around vessels of fibrotic tissues (Figure 19B). Time-course analysis of the murine adenine-induced nephropathy model identified progressive increases in protein and mRNA amounts (Figure 19C).

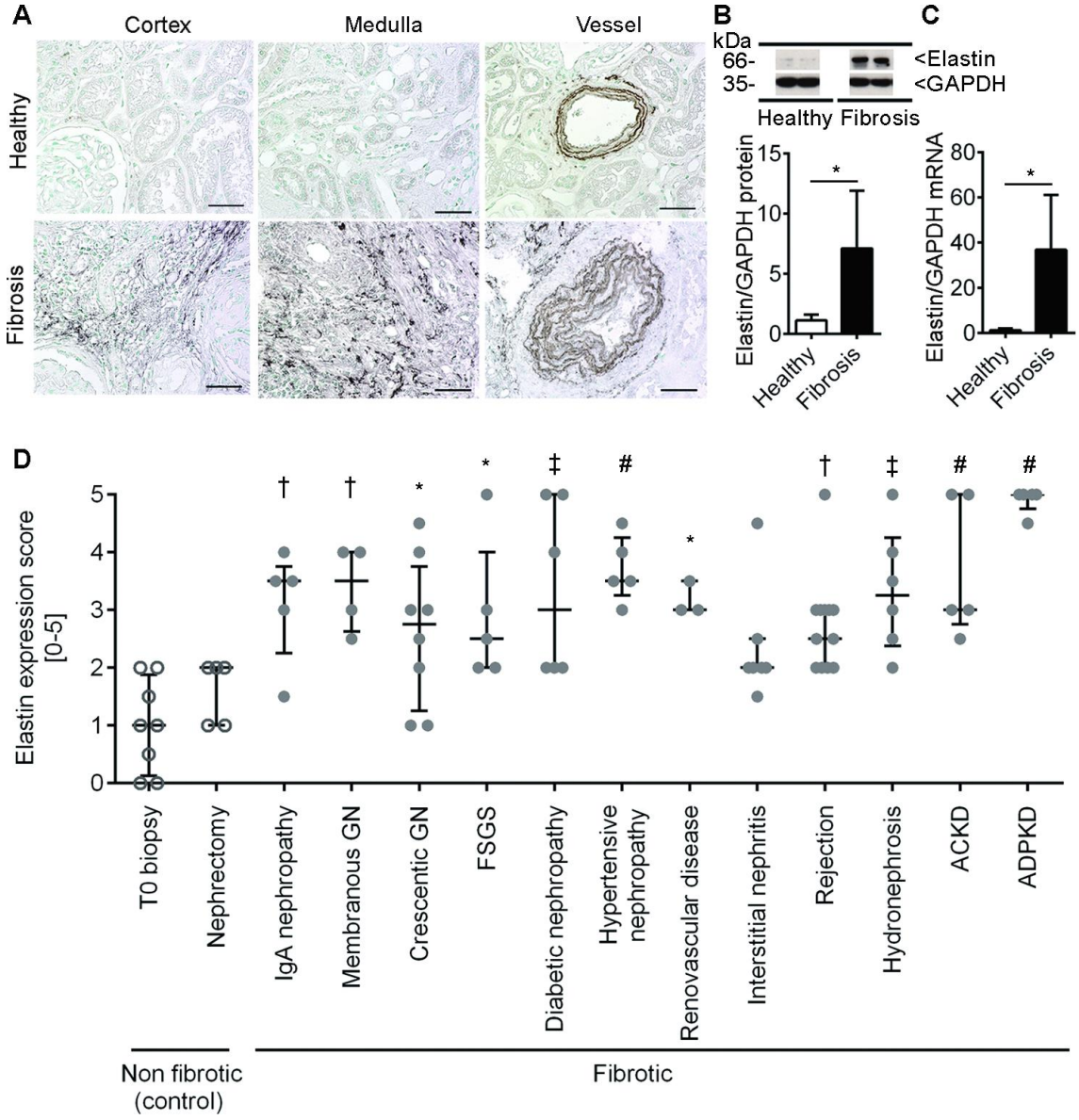

Figure 20: Elastin expression in human kidneys is increased independent of the disease etiology. (A) Immunohistochemistry and (B) Western blot analysis of human biopsies from healthy and fibrotic kidneys showed increased elastin expression in renal fibrosis. (C) qRT-PCR confirmed elastin upregulation in fibrotic kidneys. (D) Renal elastin expression is significantly increased in all major renal diseases independently of the underlying cause of the disease. [T0: protocol time zero biopsy of transplanted kidneys, Nephrectomy: non-affected tissue from tumor resection, Membranous GN: membranous glomerulonephritis, Crescentic GN: crescentic glomerulonephritis including Pauci-immune glomerulonephritis and Lupus nephritis, FSGS: focal segmental glomerulosclerosis, Rejection: including acute and chronic antibody and T-cell mediated renal rejection, ACKD: acquired cystic kidney disease and ADPKD: autosomal dominant polycystic kidney disease]. Scale bars: 50 µm. *p<0.05, †p<0.01, ‡p<0.001, #p<0.0001 (Sun et al., 2019).

Complementary to the elastin up-regulation in mice and rats, elastin overexpression was similar on renal tissue obtained from CKD patients (Figure 20). Immunohistochemistry revealed a prominent elastosis of the vasculature (Figure 20A). The significant overexpression of elastin during fibrosis was as well confirmed on a protein and mRNA level (Figure 20B, C). The biopsies from the 146 patients included all major renal diseases and emphasized that the strong elastin upregulation was independent of the underlying disease etiology (Figure 20D). This verifies the practicability of elastin as a target for specific molecular imaging of renal fibrosis (Sun et al., 2019).

For the molecular imaging of elastin expression in kidney fibrosis, the elastin-specific MRI contrast agent ESMA was applied in comparison with the nonspecific, clinical routine contrast agent Gd-DTPA. T1-weighted TSE imaging ($T1_WI$) and T1 relaxometry provided optimal signal/echo time differences 24 h after the contrast agent injection. These signal differences were normalized to the signal of the spinal erector muscle and expressed either as ΔCNR or as ΔR_1, respectively. $T1_WI$ revealed significantly higher ESMA accumulation in kidneys with adenine-diet induced crystal-nephropathy than in healthy kidneys as well as stronger signal enhancement by ESMA administration compared to standard Gd-DTPA (Figure 21A, B). In both cortex and medulla the signal intensities for ESMA were up to 2.8-fold enhanced (Figure 21C, D). For further confirmation of the MRI results, the gadolinium (Gd) concentration was assessed in kidney tissue applying inductively coupled plasma-mass spectrometry (ICP-MS) and laser ablation ICP-MS (LA-ICP-MS). A quantification of the metal concentrations closely reflected the previous MRI findings. The highest Gd concentration was measured in fibrotic kidneys of mice that had been injected with ESMA (Figure 21E-G). In order to extend these results and to confirm the specificity of ESMA binding, healthy and fibrotic human kidney biopsy samples were incubated with ESMA or Gd-DTPA (Figure 21H-L). With $T1_WI$ and ICP-MS the highest contrast agent accumulation was detected in fibrotic kidneys incubated with ESMA (Sun et al., 2019).

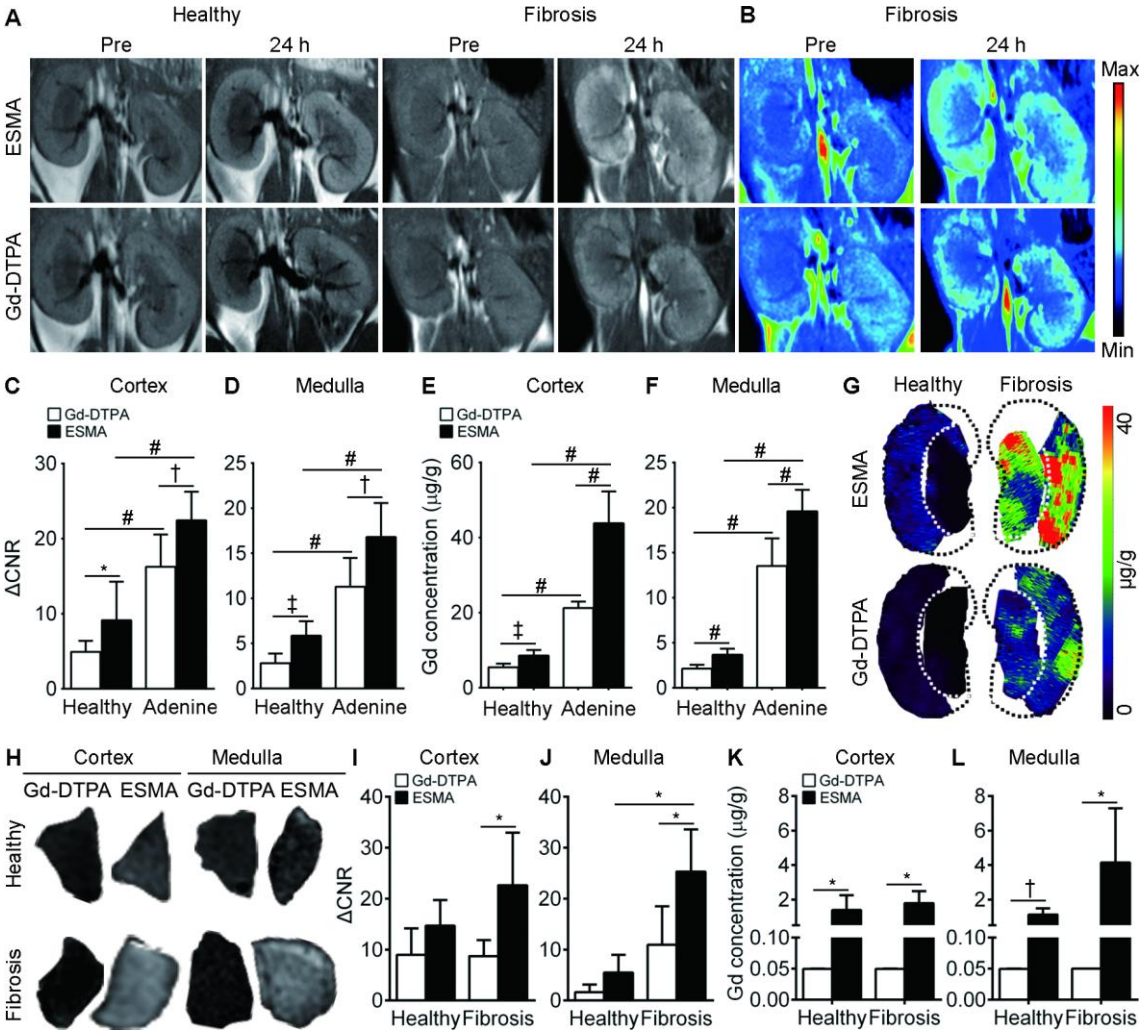

Figure 21: Elastin imaging captures renal fibrosis in adenine nephropathy and reflects elastin content in human kidney samples. (A) Coronal T1-weighted images and (B) pseudo color-coded images showed detectable changes 24 h after i.v. injection of ESMA and Gd-DTPA in healthy and adenine-induced fibrotic kidneys. (C, D) Quantification of normalized MRI signal intensities in cortex and medulla showed significant differences between the ESMA and Gd-DTPA groups in healthy and fibrotic kidneys. (E, F) Gd quantification in cortex and medulla reflected the binding of ESMA to fibrotic kidneys. (G) Gd distribution by LA-ICP-MS showed highest Gd accumulation in fibrotic kidneys of the ESMA group. (H) Representative $T1_{wI}$ images of gelatin-embedded human kidney biopsies showed increased signals in cortex as well as medulla after incubation with ESMA compared to Gd DTPA. (I, J) Quantification of normalized MR signal intensities reveals differences between the ESMA and Gd-DTPA group in healthy non-fibrotic and fibrotic kidneys. (K, L) Gd quantification reflected the *ex vivo* binding of ESMA in fibrotic human kidneys. *p<0.05, †p<0.01, ‡p<0.001, #p<0.0001 (Sun et al., 2019).

An *in vivo* competition experiment was performed in the I/R model to confirm the specific binding of ESMA to elastin. Therefore, a 25-fold excess of ^{69}Gd-labeled ESMA was administered, which does not alter MRI signal intensities, followed 4 h later by the injection of standard ^{153}Gd-ESMA. In comparison, mice that did receive the blocking ^{69}Gd-ESMA showed significantly lower MRI signal intensities, which supported the specificity of ESMA (Figure 22A, B). This competition study did not impair the expression of fibrotic ECM components in any way (Figure 22C-E).

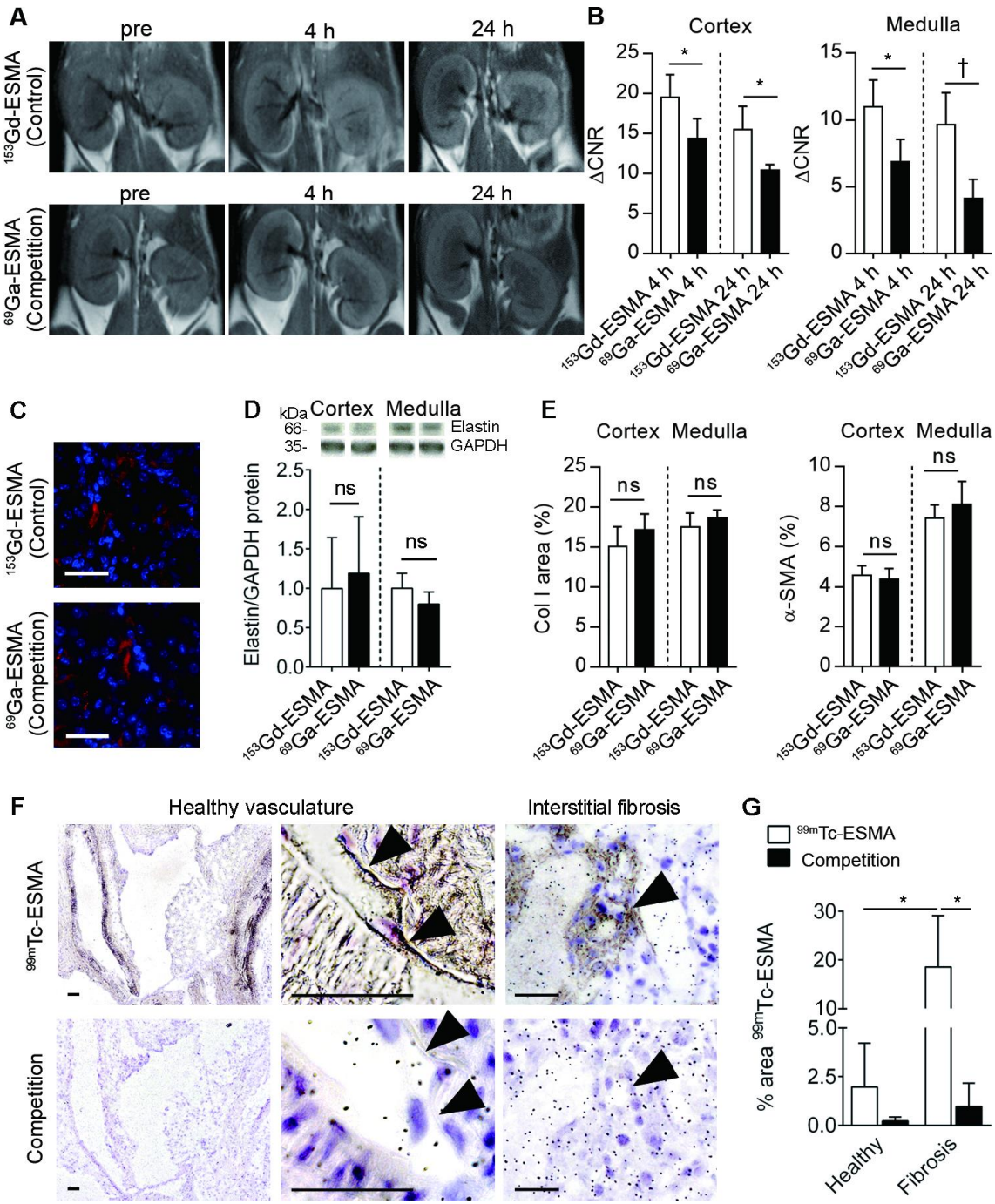

Figure 22: Confirmation of the specificity of ESMA binding to elastin in a competition experiment. (A, B) Representative T1-weighted MR images and quantification of normalized MR signal intensities of kidneys of I/R mice that either got one standard ^{153}Gd-ESMA injection (control) or a pre-injection of 25-fold excess of ^{69}Ga-ESMA, followed by an additional standard ^{153}Gd-ESMA injection (competition). ^{69}Ga-ESMA competition resulted in significantly reduced signals in cortex and medulla at 4 and 24 h after injection. (C, D) Immunofluorescence and Western blot showed no differences in elastin expression in mice with ^{153}Gd-ESMA and mice with pre-injection of 25x ^{69}Ga-ESMA. (E) Quantification of collagen I and α-SMA in both kidneys confirmed an equal extend of renal fibrosis for both groups. (F) Representative images and (G) quantification of binding of radiolabeled ^{99}Tc-EMSA to murine kidney sections *ex vivo*. ESMA detected elastin expression at arteries in healthy kidneys and showed increased binding at the interstitium of fibrotic kidneys (arrowheads). This binding was completely blocked by co-incubation of slides with 10 000-fold excess of ^{69}Ga-ESMA confirming the *in vivo* competition effect. Scale bars: 50 µm. *p<0.05, †p<p0.01, ns: not significant (Sun et al., 2019).

In addition, the binding of radiolabeled ^{99m}Tc-ESMA to elastin in fibrotic kidneys was analyzed in the vasculature and interstitium. On murine renal tissue sections the *ex vivo* binding of ^{99m}Tc-ESMA to elastin was efficiently inhibited upon competitive binding with the nonradioactive ^{153}Gd-ESMA (Figure 22F, G) (Sun et al., 2019).

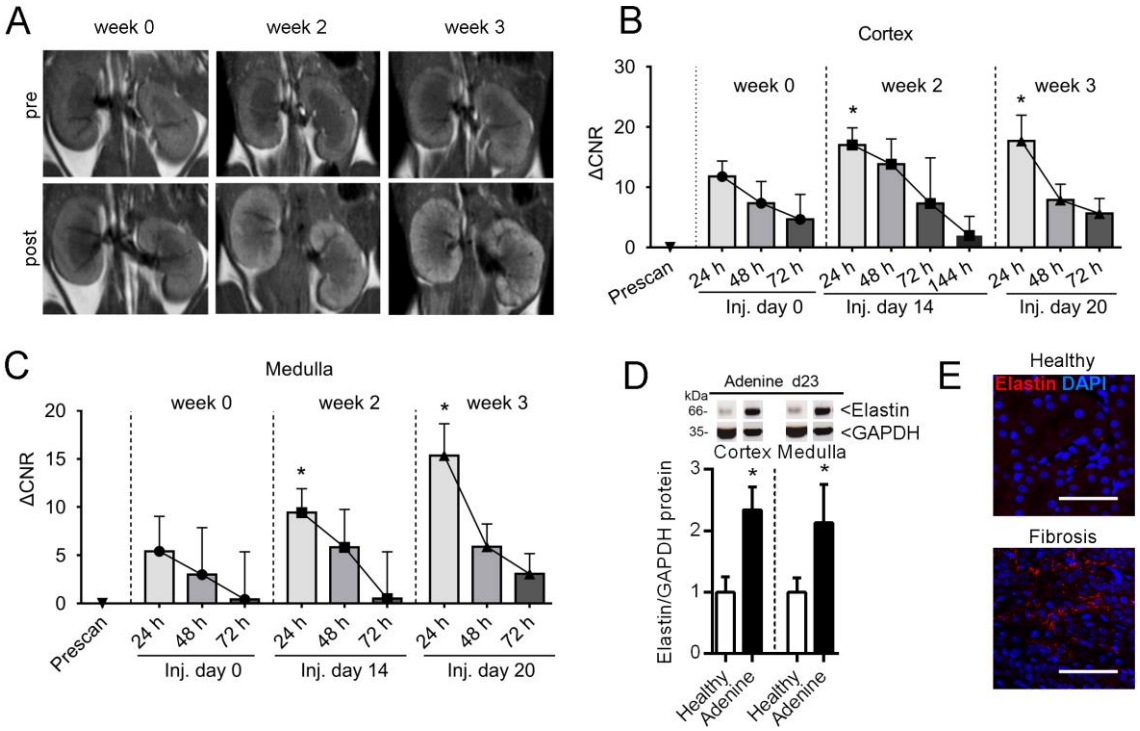

Figure 23: Elastin imaging enables longitudinal monitoring of fibrosis progression in mice with adenine diet–induced nephropathy. (A) Representative T1-weighted MR images in renal fibrosis before disease induction (week 0) as well as at the second and third week of adenine diet. Scans were acquired before (pre) and 24 h after injection of the contrast agent. (B, C) MR signal quantification in cortex and medulla showed highest ΔCNR peak at 24 h after ESMA injection, and a gradual decrease within 48 and 72 h. (D) Representative Western blot quantification confirmed the upregulation of elastin in adenine nephropathy-related fibrosis. (E) Immunofluorescence images showed increase of elastin in renal fibrosis. Scale bars: 50 µm. *p<0.05 (Sun et al., 2019).

Over 3 weeks the development of renal fibrosis was non-invasively monitored using ESMA in the adenine-induced nephropathy model, in order to evaluate if ESMA is able to accurately capture the disease progression. The normalized MRI signal intensities reflected the elastin expression and fibrosis extent in cortex and medulla (Figure 23A-C). The expression degree of elastin was confirmed by Western blot and microscopic analysis (Figure 23D, E). Most importantly, the MRI signal intensities showed a peak at 24 h after ESMA injection and after this a gradual decrease in ΔCNR. About 95% of the ESMA were eliminated from the kidneys within 72 h after administration (Sun et al., 2019).

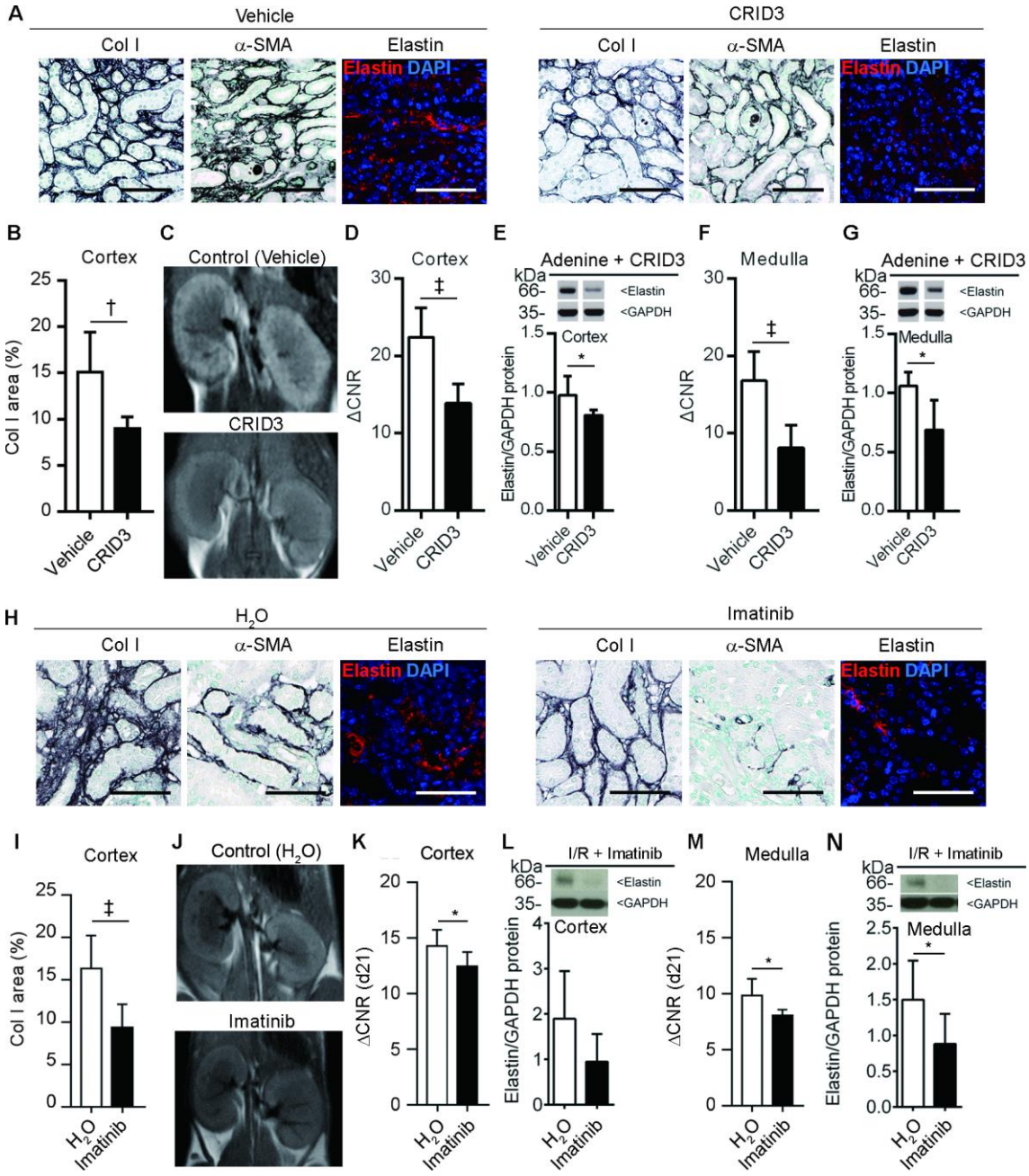

Figure 24: Elastin imaging enables monitoring of anti-fibrotic therapy response. (A) Representative immunohistochemical and immunofluorescent staining of collagen (Col) I, α-SMA and elastin in kidneys from vehicle and CRID3-treated mice with adenine-induced nephropathy confirmed decreased renal fibrosis and elastin expression in CRID3-treated mice. (B) Quantification of Col I positive area in the cortex supported the significant decrease of renal fibrosis in CRID3-treated mice. (C) MR images 24 h after injection of ESMA showed decreased signals in CRID3-treated kidneys compared to the vehicle control kidneys. (D, F) Quantification of signal intensities of the cortex (D) and the medulla (F) showed decreased normalized signal intensities for the CRID3 group. (E, G) Representative Western blot and quantification in cortex (E) and medulla (G) indicated decreased elastin expression in kidneys treated with CRID3. (H) Immunohistochemical and immunofluorescent stainings of Col I, α-SMA and elastin confirmed decreased renal fibrosis and elastin expression in Imatinib treated I/R mice. (I) Quantification of Col I positive area in the cortex supported the significant decrease of renal fibrosis in Imatinib treated mice compared to controls, (J) which was reflected by decreased MRI signals 24 h after injection ESMA. (K, M) Quantification of ΔCNR values in cortex (K) and medulla (M) confirmed this decrease. (L, N) In addition Western blot analysis validated the decrease of elastin expression in I/R kidneys treated with Imatinib. Scale bar: 50 µm. *p<0.05, †p<0.01, ‡p<0.001 (Sun et al., 2019).

The development of anti-fibrotic treatments depends tremendously on the defined clinical readouts and monitoring possibilities available. The treatment response visualization of two inhibitors was assessed using ESMA for elastin specific molecular imaging. Inflammasome inhibition by means of daily CRID3 administration diminished renal fibrosis and reduced significantly the ECM deposition in the adenine nephropathy model (Figure 24A, B, E, G). The significantly reduced MRI signal intensities demonstrated the suitability of visualizing the treatment effects of CRID3 by means of ESMA (Figure 24C, D, F). The second evaluated therapeutic was the tyrosine kinase inhibitor Imatinib, which was applied between day 7 and day 21 in an I/R model with already established fibrosis. ECM deposition and elastin expression were reduced in kidneys by means of Imatinib (Figure 24H, I, L, N). The MRI signal intensities in Imatinib-treated kidneys were significantly reduced and resembled the treatment efficacy (Figure 24J, K, M). ESMA-based molecular imaging enabled treatment monitoring in renal fibrosis (Sun et al., 2019).

In a reversible model of adenine nephropathy the sensitivity and precision of elastin-based imaging was investigated in relation to the clinical routine assessment of kidney functionality, in form of serum creatinine and creatinine clearance (Figure 25). For the regression monitoring the mice had 14 days to recover, after an initial fibrosis induction period of 14 days (Figure 25A). After this recovery phase the renal function was found to be normalized (Figure 25B-E), although renal fibrosis persisted and elastin levels remained increased (Figure 25F-J). The molecular imaging of elastin captured the persistent morphological damage by means of high MRI signal intensities that reflect the remaining fibrosis (Figure 25K-M). Elastin imaging was able to detect the ensuing fibrosis that was not identifiable via routine assessment. Overall, elastin-targeted molecular MRI allowed for non-invasive, quantitative and longitudinal assessment of renal fibrosis and regression (Sun et al., 2019).

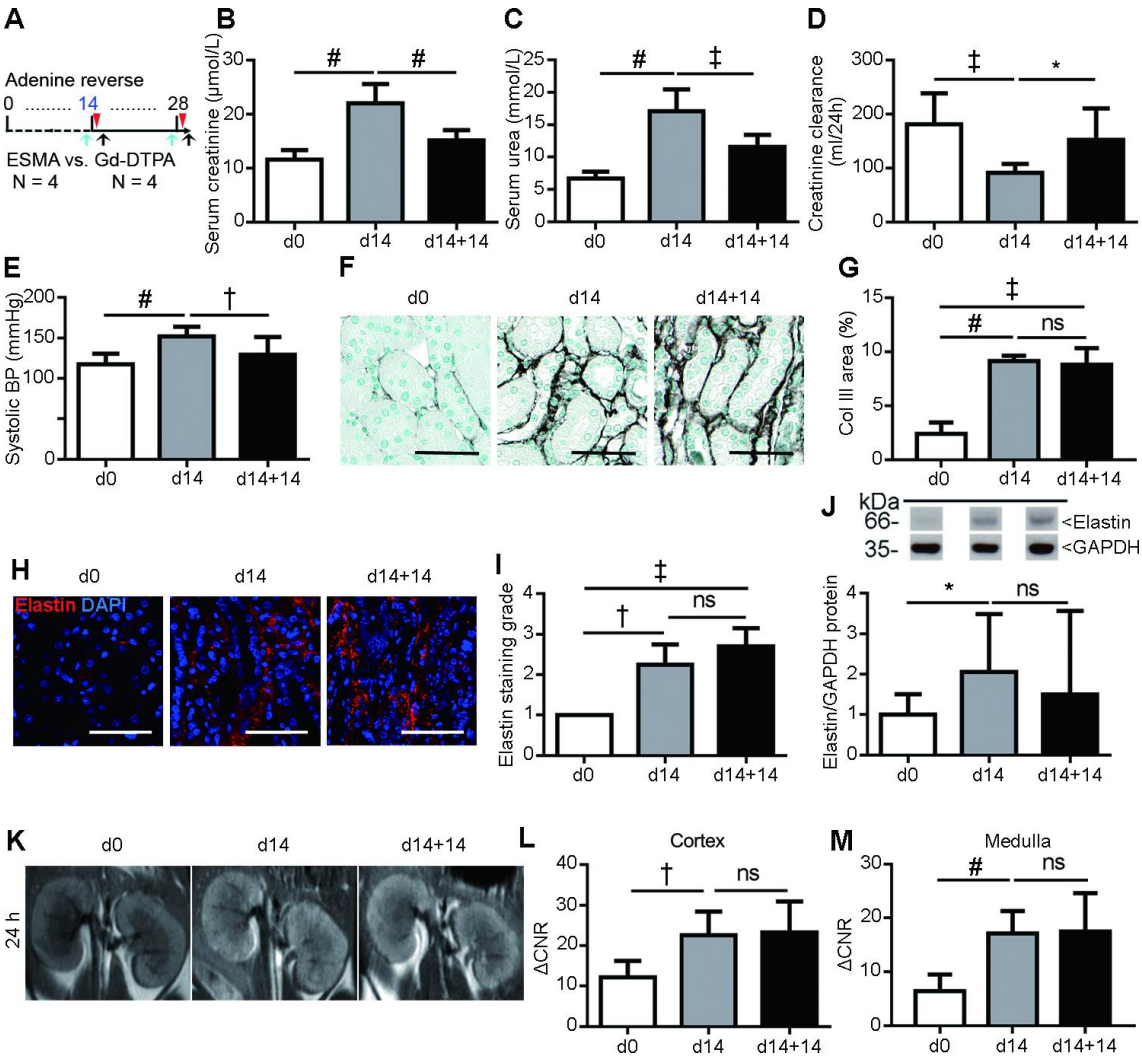

Figure 25: Elastin imaging identifies residual renal fibrosis that is not detectable using routine kidney function measurement. (A) Scheme of the adenine reversal experiment: After 14 days of adenine diet, the animals received normal chow for 14 days in the "regeneration" phase. Red triangles represent injection of contrast agents, blue and black arrow show MRI scanning before and 24 h after injection, respectively. (B-E) Serum creatinine (B), serum urea (C), creatinine clearance (D) and systolic blood pressure (BP) (E) indicated recovery after terminating the adenine diet. (F, G) Representative immunohistochemical images and quantification of collagen type III positively stained areas in the cortex showed fibrosis induction after 14 days, which remained in the subsequent regeneration phase. (H, I) Immunofluorescent staining of elastin fibers as well as their quantification confirmed the ensuing fibrosis that remained consistently high in the subsequent regeneration phase even after stopping the adenine diet. (J) The elevated elastin levels were confirmed by Western blot analysis. (K) The trend of remaining fibrosis was reflected by the MR images, which indicated increased signals in week 2 of the adenine diet and similar high signals even after its termination. (L, M) Quantification of the normalized signal intensities confirmed increased ΔCNR in the first 2 weeks of adenine diet and the period of 2 weeks after stopping the adenine diet. Scale bars, 50 µm. *p<0.05, †p<0.01, ‡p<0.001, #p<0.0001 (Sun et al., 2019).

5. Discussion

5.1. Vascular priming via macrophage re-education enhances drug delivery

The abnormal tumor microenvironment creates challenges for the development of treatments, including vascular and interstitial barriers that impede drug delivery and penetration. Modulating strategies, like the priming of tumor blood vessels, are promising neoadjuvant interventions (Huang et al., 2013). However, the effects of anti-angiogenic approaches are highly dose- and time-dependent, complicating any investigations concerning the vascular normalization window. To avoid these limitations, a genetically normalized setup appears to be well suited to systematically study the effect of macrophage-mediated vascular normalization on the accumulation and penetration of a 10-20 nm-sized prototypic drug carrier. In this regard, HRG-knockout and wild type mice are combined with HRG-overexpressing or normal t241 fibrosarcoma cells.

First of all, the (over)expression of HRG ensures a less dense vascular network in the tumor with a lower angiogenic potential. The key to these HRG-mediated vascular changes are the TAM and their polarization status (Rolny et al., 2011, Tugues et al., 2012). The connection between HRG expression and macrophage skewing toward the anti-tumor M1-like phenotype is in line with previous studies (Olsson et al., 2004, Rolny et al., 2011, Tugues et al., 2012). The overall amount of TAM is not decreased, only the M2-like macrophage population is reduced. The stability in TAM recruitment could even be considered beneficial, in light of a polymer study, in which TAM have served as cellular drug reservoirs that gradually released their payload to neighboring tumor cells (Miller et al., 2015). Interestingly, a TAM polarization directed toward a more M1-like provokes a strong delay in tumor growth, which is in contrast to tumor progression reported in cases of complete macrophage depletion (Rolny et al., 2011).

Multimodal and multiscale optical imaging confirms that HRG-mediated priming of the tumor vasculature improves polymer accumulation. 2D-FRI indicates that the accumulation is most prominent in the peripheral tumor zone, which is due to the large and well-perfused blood vessels and a low IFP in the tumor periphery (Chen et al., 2017, Stapleton et al., 2015, Stylianopoulos et al., 2013). For an efficient polymeric drug delivery a homogenous distribution, extravasation from the vasculature and deep penetration into the tumor interstitium are substantial. Otherwise, inadequate

penetration implies insufficient therapy, which is a major difficulty in drug delivery (Dreher et al., 2006). Fluorescence microscopy and TPLSM confirm that the penetration of polymers out of the vasculature into the tumor tissue increases as a result of HRG-mediated vascular priming.

Overall, the increased expression of HRG causes a re-education of TAM toward a more anti-angiogenic M1-like phenotype that results in a primed microenvironment, improving ultimately the drug delivery into and inside the tumor (Theek et al., 2018). This is in agreement with several clinical studies where standard chemotherapeutics, metronomically administered anticancer drugs or radiotherapy have benefited from vascular normalization (Jain et al., 2006, Mpekris et al., 2017, Tolaney et al., 2015, Willett et al., 2006). Consequently, neoadjuvant therapies, that modulate the tumor microenvironment by means of vascular priming, hold the potential to improve the delivery and efficacy of nanomedicines (Theek et al., 2018).

5.2. Sonopermeation improves liposome delivery into tumors with low EPR

Sonopermeation has the potential to enhance drug delivery and improve the efficiency of treatments in tumors with impaired EPR characteristics. The shown increase in both the macro-accumulation as well as the micro-distribution of liposomes provides the basis for the further translation of this technology. Thereby, the observed high inter-individual variability is most likely due to the relatively low number of animals per experimental group (n=5) and experimental baseline fluctuations in the EPR effect itself, which causes outcome relativization (Lammers et al., 2007, Rapoport et al., 2013, Sanches et al., 2014, Theek et al., 2016). Partially, the discrepancies in EPR effect manifestation are caused by differences in tumor perfusion, which substantially also affects the impact of sonopermeation. For example, if the number of MB entering the tumor is limited in the first place, then naturally their availability for sonopermeation is confined (Ekdawi et al., 2015, Theek et al., 2014a).

Phenotypical tumor characteristics that cause a low EPR effect, and further its variability, differ between A431 and BxPC-3. A431 originates from an epidermoid carcinoma, which is known in the literature for tiny and immature blood vessels, but a dense cellular network resulting in extremely limited intercellular space (Ehling et al., 2014). The high cellularity accounts for the poor EPR in A431 tumors. For the pancreatic adenocarcinoma cell line, BxPC-3, large and mature vessels as well as a high stromal content are characteristic. There the dense collagen network impairs the distribution of nanocarrier into and throughout the tumor interstitium (Brown et al., 2003, Netti et al., 2000). Therefore, the liposome penetration without sonopermeation is worse in BxPC-3 tumors than in A431 control tumors. Independent of the applied MB type, the penetration of the relatively large model nanocarrier is significantly enhanced. No clear differences with regard to the MB type, soft-shelled MM or hard-shelled PBCA, are observed. Further studies have to address possible distinctions in physical and mechanical MB behavior. However, in both tumor types the liposome penetration is enhanced upon sonopermeation with either MB class. In the future, studies have to comprehend the mechanistic aspects of sonopermeation and the effect on other drug delivery systems, which will enable protocols in additional tissues and pathologies (Snipstad et al., 2018, Theek et al., 2016).

5.3. Collagen as an imaging biomarker of renal fibrosis

Combining the fluorophore-labeled contrast agent CNA35 and optical imaging, specific and non-invasive assessment of collagen deposition in renal fibrosis is enabled. This provides the first proof-of-concept for molecular imaging of collagen content in fibrotic kidneys, extending previous studies with CNA35 in cardiovascular fibrosis (Megens et al., 2007). *Ex vivo* and histological analyses revealed that CNA35 mainly binds to the fibrillar scar collagens type I and III, which are the main components of the ECM in fibrotic kidneys, whereas only a low degree of co-localization was observed with non-fibrillar type IV collagen in basement membranes, consistent with solid phase binding assays (Krahn et al., 2006). Further, the *ex vivo* optical imaging, assessing CNA35-FITC distribution after i.v. injection, highlighted a prominent perivascular fibrosis (Baues et al., 2019).

Collagen is upregulated early in the disease course and extremely abundant in fibrotic tissue, making it a convenient target. Conversely, however, the high baseline abundance of collagens in healthy kidneys and other tissues or organs results in higher background signal. Measurements distinguishing various degrees of fibrosis should be performed in the future to create a solid framework for molecular imaging biomarker in renal fibrosis. In addition, for a successful translation into the clinic, further contrast agent adaptation is needed before first in human studies, since optical imaging approaches are not very suitable in kidney fibrosis. Future systematic experiments should enable the optimization of the target, probes and imaging protocols for the translation of a non-invasive but quantitative diagnosis, staging and treatment monitoring of kidney fibrosis (Baues et al., 2019).

5.4. Elastin imaging enables noninvasive staging and treatment monitoring

ESMA-based molecular MRI noninvasively visualizes elastin expression and allows for repetitive and reproducible assessment of renal fibrosis. Elastin imaging enables longitudinal monitoring of therapeutic interventions and reflects fibrosis more faithfully compared to current clinical measurements that focus on functional renal parameters, e.g. GFR. First of all, elastin is largely absent in healthy kidney tissue but dynamically up-regulated in fibrosis. The expression of elastin is increased independently of the underlying pathological trigger, which is shown by the evaluation of 10 rodent models and more than 140 patient biopsies, including all major renal diseases (Sterzel et al., 2000, Thongboonkerd et al., 2004). This broad applicability suggests that elastin is a suitable biomarker for imaging and monitoring of CKD. Elastin imaging is even more sensitive and precise in detecting ensuing fibrosis, which is not detected by measurements of kidney function. Renal performance might recover via hyperfiltration by remaining intact nephrons, which can obscure the actual persistent morphological damage. Additionally, the imaging of elastin applying ESMA reflects the fibrotic disease stage and progression precisely. The given pharmacokinetics and excretion rate from the body within 72 h indicate the possibility of longitudinal and repetitive assessment using ESMA-enhanced molecular MRI. However, the potential risk of inducing nephrogenic systemic fibrosis has to be considered for clinical translation of ESMA-based molecular imaging. This complication, in regard to the use of a gadolinium-labeled contrast agent, concerns especially dialysis patients or patients with very advanced CKD stage 5. Presumably, the imaging of elastin is clinically more useful in earlier CKD stages, for which repetitive administration of Gd-containing contrast agents is generally considered to be safe (Chrysochou et al., 2010). Potential safety concerns could also be resolved by an alternative labeling of ESMA. Radioisotopes, such as ^{68}Ga or ^{111}In, could be tested with ESMA in positron electron tomography (PET) and single-photon emission computed tomography (SPECT). Accordingly, elastin imaging is a novel, robust fibrosis-specific diagnostic tool and a potential surrogate endpoint for clinical studies evaluating anti-fibrotic therapies.

Summary: Modulating and monitoring the microenvironment in cancer and renal fibrosis (Modulation und Monitoring der Mikroumgebung in Krebs und Nierenfibrose)

by Maike Baues

The dysregulation of microenvironmental homeostasis, particularly of the extracellular matrix (ECM), is a common driving force in various diseases, including renal fibrosis and cancer. A pathological microenvironment, together with an abnormal vascular network and dysfunctional lymphatic system, form the basis for the enhanced permeability and retention (EPR) effect, which is the underlying mechanism for passive tumor targeting with nanomedicine formulations. The EPR effect, however, is a highly variable phenomenon, in animal models and in patients. In this thesis, pharmacological and physical strategies to modulate EPR-based nanomedicine delivery to tumors are assessed, including vascular normalization and sonopermeation (i.e. the combination of ultrasound (US) and microbubbles (MB)). Elevated expression of the histidine-rich glycoprotein (HRG) polarizes tumor-associated macrophages toward an anti-tumor M1-like phenotype, thereby inducing vascular normalization and enhancing the EPR effect. Hard- and soft-shelled MB formulations are used in this thesis to study the impact of sonopermeation on the EPR-mediated accumulation and penetration of liposomes into highly cellular A431 and highly stromal BxPC-3 carcinoma xenografts. Our work demonstrates that both vascular normalization and sonopermeation improve the tumor accumulation, tumor penetration and the intra-tumoral distribution of nanomedicine-based drug delivery systems.

Excessive ECM deposition in the kidney impairs renal function, contributing to incidence and severity of chronic kidney disease (CKD). As an alternative to needle-based biopsies, collagen- and elastin-specific molecular imaging were explored in this thesis for non-invasively diagnosing and staging renal fibrosis. The collagen-binding protein CNA35 accumulated significantly stronger in fibrotic kidneys, and specifically detected collagen types I and III on murine and human sections. Elastin was found to be *de novo* overexpressed in fibrotic renal tissues of mice, rats and patients. The elastin-specific molecular imaging agent ESMA captured fibrotic areas in human kidney samples. Fibrosis progression and anti-fibrotic therapy responses were visualized and quantified by means of ESMA-MRI.

Taken together, these findings indicate that the modulation of the microenvironment improves EPR-mediated tumor targeting and demonstrate that ECM monitoring enables specific and repetitive assessment of renal fibrosis. Nanomedicines and molecular imaging hold the potential to substantially transform the diagnosis and treatment of cancer and CKD.

Zusammenfassung: Modulation und Monitoring der Mikroumgebung in Krebs und Nierenfibrose (Modulating and monitoring the microenvironment in cancer and renal fibrosis) von Maike Baues

Die Dysregulation der Mikroumgebungshomöostase, insbesondere der extrazellulären Matrix (ECM), ist ein häufiger Antriebsfaktor bei Krankheiten, einschließlich Nierenfibrose und Krebs. Eine pathologische Mikroumgebung bildet, zusammen mit einem abnormalen Gefäßnetzwerken und unfunktionalen lymphatischen System, die Prämisse für den Effekt der erhöhten Permeabilität und Retention (EPR), welcher der zugrunde liegende Mechanismus für passives Tumor-Targeting von Nanowirkstoffen ist. Der EPR-Effekt ist jedoch ein sehr variables Phänomen. Daher werden in der vorliegenden Dissertation verschiedene pharmakologische und physikalische Strategien zur Modulation des EPR-vermittelten Wirkstofftransports untersucht, u.a. Gefäßnormalisierung und Sonopermeation (Kombination aus Ultraschall (US) und Mikrobläschen (MB)). Erhöhte Expression des Histidin-reichen Glykoproteins (HRG) polarisiert tumorassoziierte Makrophagen in Richtung des tumorhemmenden M1-ähnlichen Phänotypen, was eine Gefäßnormalisierung und Verstärkung des EPR Effektes herbeiführt. Hart- und weichschalige MB wurden in dieser Doktorarbeit zur Untersuchung der Auswirkungen von Sonopermeation, in Bezug auf EPR-vermittelter Liposomenakkumulation und -penetration, im A431 Karzinom und BxPC-3 Pankreastumor eingesetzt. Unsere Forschung zeigt, dass Gefäßnormalisierung und Sonopermeation sowohl die Anreicherung als auch die Verteilung von nanomedizinischen Wirkstoffträgersystemen in Tumoren verbessern.

Übermäßige Ablagerung von ECM beeinträchtigt die Nierenfunktion und trägt zu Inzidenz von chronischer Niereninsuffizienz (CKD) bei. Alternativ zu Nadelbiopsien wurden in dieser Arbeit kollagen- und elastinbasierte Bildgebungsverfahren zur nichtinvasiven Diagnose und Einstufung von Nierenfibrose erforscht. Das kollagen-bindende Protein CNA35 sammelte sich stärker in fibrotischen Nieren an und erkannte spezifisch die Kollagentypen I und III auf murinen und menschlichen Schnitten. Für Elastin wurde im fibrotischen Nierengewebe von Mäusen, Ratten und Patienten eine *de novo* Überexpression festgestellt. Das Elastin-spezifische Kontrastmittel ESMA erfasste Fibrose in menschlichen Proben. Progression sowie Therapieansprechen wurden mittels ESMA-MRT visualisiert und quantifiziert.

Insgesamt zeigen diese Ergebnisse, dass die Modulation der Mikroumgebung das EPR-vermittelte Tumor Targeting verbessert sowie dass das ECM Monitoring spezifische und wiederholte Beurteilung von Nierenfibrose ermöglicht. Nanowirkstoffe und molekulare Bildgebung besitzen Potential die Diagnose und Behandlung von Krebs und CKD maßgeblich zu verändern.

6. References

Alix-Panabieres C, Pantel K (2016) Clinical Applications of Circulating Tumor Cells and Circulating Tumor DNA as Liquid Biopsy. Cancer Discov 6: 479-91

Allen TM, Cullis PR (2004) Drug delivery systems: entering the mainstream. Science 303: 1818-22

Appold L, Shi Y, Rutten S, Kuhne A, Pich A, Kiessling F, Lammers T (2017) Physicochemical Characterization of the Shell Composition of PBCA-Based Polymeric Microbubbles. Macromol Biosci 17

Aydin S, Signorelli S, Lechleitner T, Joannidis M, Pleban C, Perco P, Pfaller W, Jennings P (2008) Influence of microvascular endothelial cells on transcriptional regulation of proximal tubular epithelial cells. Am J Physiol Cell Physiol 294: C543-54

Bachem MG, Schunemann M, Ramadani M, Siech M, Beger H, Buck A, Zhou S, Schmid-Kotsas A, Adler G (2005) Pancreatic carcinoma cells induce fibrosis by stimulating proliferation and matrix synthesis of stellate cells. Gastroenterology 128: 907-21

Balkwill FR, Capasso M, Hagemann T (2012) The tumor microenvironment at a glance. J Cell Sci 125: 5591-6

Bartneck M, Scheyda KM, Warzecha KT, Rizzo LY, Hittatiya K, Luedde T, Storm G, Trautwein C, Lammers T, Tacke F (2015) Fluorescent cell-traceable dexamethasone-loaded liposomes for the treatment of inflammatory liver diseases. Biomaterials 37: 367-82

Baues M, Dasgupta A, Ehling J, Prakash J, Boor P, Tacke F, Kiessling F, Lammers T (2017) Fibrosis imaging: Current concepts and future directions. Adv Drug Deliv Rev 121: 9-26

Baues M, Klinkhammer BM, Ehling J, Gremse F, van Zandvoort MA, Reutelingsperger CPM, Daniel C, Amann K, Babickova J, Kiessling F, Floege J, Lammers T, Boor P (2019) A collagen-binding protein enables molecular imaging of kidney fibrosis in vivo. Kidney Int in press

Bertrand N, Wu J, Xu X, Kamaly N, Farokhzad OC (2014) Cancer nanotechnology: the impact of passive and active targeting in the era of modern cancer biology. Adv Drug Deliv Rev 66: 2-25

Bijlsma MF, van Laarhoven HW (2015) The conflicting roles of tumor stroma in pancreatic cancer and their contribution to the failure of clinical trials: a systematic review and critical appraisal. Cancer Metastasis Rev 34: 97-114

Bissell MJ, Hines WC (2011) Why don't we get more cancer? A proposed role of the microenvironment in restraining cancer progression. Nat Med 17: 320-9

Bjornmalm M, Thurecht KJ, Michael M, Scott AM, Caruso F (2017) Bridging Bio-Nano Science and Cancer Nanomedicine. ACS Nano 11: 9594-9613

Boor P, Babickova J, Steegh F, Hautvast P, Martin IV, Djudjaj S, Nakagawa T, Ehling J, Gremse F, Bucher E, Eriksson U, van Roeyen CR, Eitner F, Lammers T, Floege J, Peutz-Kootstra CJ, Ostendorf T (2015) Role of platelet-derived growth factor-CC in capillary rarefaction in renal fibrosis. Am J Pathol 185: 2132-42

Boor P, Ostendorf T, Floege J (2010) Renal fibrosis: novel insights into mechanisms and therapeutic targets. Nat Rev Nephrol 6: 643-56

Brown E, McKee T, diTomaso E, Pluen A, Seed B, Boucher Y, Jain RK (2003) Dynamic imaging of collagen and its modulation in tumors in vivo using second-harmonic generation. Nat Med 9: 796-800

Buhl EM, Djudjaj S, Babickova J, Klinkhammer BM, Folestad E, Borkham-Kamphorst E, Weiskirchen R, Hudkins K, Alpers CE, Eriksson U, Floege J, Boor P (2016) The role of PDGF-D in healthy and fibrotic kidneys. Kidney Int 89: 848-61

Carmeliet P, Jain RK (2011) Principles and mechanisms of vessel normalization for cancer and other angiogenic diseases. Nat Rev Drug Discov 10: 417-27

Chauhan VP, Jain RK (2013) Strategies for advancing cancer nanomedicine. Nat Mater 12: 958-62

Chauhan VP, Stylianopoulos T, Martin JD, Popovic Z, Chen O, Kamoun WS, Bawendi MG, Fukumura D, Jain RK (2012) Normalization of tumour blood vessels improves the delivery of nanomedicines in a size-dependent manner. Nat Nanotechnol 7: 383-8

Chen H, Zhang W, Zhu G, Xie J, Chen X (2017) Rethinking cancer nanotheranostics. Nat Rev Mater 2

Chrysochou C, Power A, Shurrab AE, Husain S, Moser S, Lay J, Salama AD, Kalra PA (2010) Low risk for nephrogenic systemic fibrosis in nondialysis patients who have chronic kidney disease and are investigated with gadolinium-enhanced magnetic resonance imaging. Clin J Am Soc Nephrol 5: 484-9

Cochran MC, Eisenbrey JR, Soulen MC, Schultz SM, Ouma RO, White SB, Furth EE, Wheatley MA (2011) Disposition of ultrasound sensitive polymeric drug carrier in a rat hepatocellular carcinoma model. Acad Radiol 18: 1341-8

Condeelis J, Segall JE (2003) Intravital imaging of cell movement in tumours. Nat Rev Cancer 3: 921-30

Cox TR, Erler JT (2011) Remodeling and homeostasis of the extracellular matrix: implications for fibrotic diseases and cancer. Dis Model Mech 4: 165-78

Cox TR, Erler JT (2014) Molecular pathways: connecting fibrosis and solid tumor metastasis. Clin Cancer Res 20: 3637-43

Crowley E, Di Nicolantonio F, Loupakis F, Bardelli A (2013) Liquid biopsy: monitoring cancer-genetics in the blood. Nat Rev Clin Oncol 10: 472-84

Danhier F (2016) To exploit the tumor microenvironment: Since the EPR effect fails in the clinic, what is the future of nanomedicine? J Control Release 244: 108-121

de Groot AE, Roy S, Brown JS, Pienta KJ, Amend SR (2017) Revisiting Seed and Soil: Examining the Primary Tumor and Cancer Cell Foraging in Metastasis. Mol Cancer Res 15: 361-370

De Nicola L, Minutolo R (2016) Worldwide growing epidemic of CKD: fact or fiction? Kidney Int 90: 482-4

Decleves AE, Sharma K (2014) Novel targets of antifibrotic and anti-inflammatory treatment in CKD. Nat Rev Nephrol 10: 257-67

Dewitte H, Van Lint S, Heirman C, Thielemans K, De Smedt SC, Breckpot K, Lentacker I (2014) The potential of antigen and TriMix sonoporation using mRNA-loaded microbubbles for ultrasound-triggered cancer immunotherapy. J Control Release 194: 28-36

Diaz LA, Jr., Bardelli A (2014) Liquid biopsies: genotyping circulating tumor DNA. J Clin Oncol 32: 579-86

Dimcevski G, Kotopoulis S, Bjanes T, Hoem D, Schjott J, Gjertsen BT, Biermann M, Molven A, Sorbye H, McCormack E, Postema M, Gilja OH (2016) A human clinical trial using ultrasound and microbubbles to enhance gemcitabine treatment of inoperable pancreatic cancer. J Control Release 243: 172-181

Djudjaj S, Boor P (2019) Cellular and molecular mechanisms of kidney fibrosis. Mol Aspects Med 65: 16-36

Djudjaj S, Papasotiriou M, Bulow RD, Wagnerova A, Lindenmeyer MT, Cohen CD, Strnad P, Goumenos DS, Floege J, Boor P (2016) Keratins are novel markers of renal epithelial cell injury. Kidney Int 89: 792-808

Doube M, Klosowski MM, Arganda-Carreras I, Cordelieres FP, Dougherty RP, Jackson JS, Schmid B, Hutchinson JR, Shefelbine SJ (2010) BoneJ: Free and extensible bone image analysis in ImageJ. Bone 47: 1076-9

Dreher MR, Liu W, Michelich CR, Dewhirst MW, Yuan F, Chilkoti A (2006) Tumor vascular permeability, accumulation, and penetration of macromolecular drug carriers. J Natl Cancer Inst 98: 335-44

Duffield JS (2014) Cellular and molecular mechanisms in kidney fibrosis. J Clin Invest 124: 2299-306

Dvorak HF (1986) Tumors: wounds that do not heal. Similarities between tumor stroma generation and wound healing. N Engl J Med 315: 1650-9

Egeblad M, Nakasone ES, Werb Z (2010a) Tumors as organs: complex tissues that interface with the entire organism. Dev Cell 18: 884-901

Egeblad M, Rasch MG, Weaver VM (2010b) Dynamic interplay between the collagen scaffold and tumor evolution. Curr Opin Cell Biol 22: 697-706

Ehling J, Babickova J, Gremse F, Klinkhammer BM, Baetke S, Knuechel R, Kiessling F, Floege J, Lammers T, Boor P (2016) Quantitative Micro-Computed Tomography Imaging of Vascular Dysfunction in Progressive Kidney Diseases. J Am Soc Nephrol 27: 520-32

Ehling J, Bartneck M, Fech V, Butzbach B, Cesati R, Botnar R, Lammers T, Tacke F (2013) Elastin-based molecular MRI of liver fibrosis. Hepatology 58: 1517-8

Ehling J, Theek B, Gremse F, Baetke S, Mockel D, Maynard J, Ricketts SA, Grull H, Neeman M, Knuechel R, Lederle W, Kiessling F, Lammers T (2014) Micro-CT imaging of tumor angiogenesis: quantitative measures describing micromorphology and vascularization. Am J Pathol 184: 431-41

Ekdawi SN, Stewart JM, Dunne M, Stapleton S, Mitsakakis N, Dou YN, Jaffray DA, Allen C (2015) Spatial and temporal mapping of heterogeneity in liposome uptake and microvascular distribution in an orthotopic tumor xenograft model. J Control Release 207: 101-11

Ergen C, Niemietz PM, Heymann F, Baues M, Gremse F, Pola R, van Bloois L, Storm G, Kiessling F, Trautwein C, Luedde T, Lammers T, Tacke F (2019) Liver fibrosis affects the targeting properties of drug delivery systems to macrophage subsets in vivo. Biomaterials 206: 49-60

Erkan M, Hausmann S, Michalski CW, Fingerle AA, Dobritz M, Kleeff J, Friess H (2012a) The role of stroma in pancreatic cancer: diagnostic and therapeutic implications. Nat Rev Gastroenterol Hepatol 9: 454-67

Erkan M, Hausmann S, Michalski CW, Schlitter AM, Fingerle AA, Dobritz M, Friess H, Kleeff J (2012b) How fibrosis influences imaging and surgical decisions in pancreatic cancer. Front Physiol 3: 389

Etrych T, Mrkvan T, Rihova B, Ulbrich K (2007) Star-shaped immunoglobulin-containing HPMA-based conjugates with doxorubicin for cancer therapy. J Control Release 122: 31-8

Fang J, Nakamura H, Maeda H (2011) The EPR effect: Unique features of tumor blood vessels for drug delivery, factors involved, and limitations and augmentation of the effect. Adv Drug Deliv Rev 63: 136-51

Farrar CT, DePeralta DK, Day H, Rietz TA, Wei L, Lauwers GY, Keil B, Subramaniam A, Sinskey AJ, Tanabe KK, Fuchs BC, Caravan P (2015) 3D molecular MR imaging of liver fibrosis and response to rapamycin therapy in a bile duct ligation rat model. J Hepatol 63: 689-96

Fischer C, Mazzone M, Jonckx B, Carmeliet P (2008) FLT1 and its ligands VEGFB and PlGF: drug targets for anti-angiogenic therapy? Nat Rev Cancer 8: 942-56

Fokong S, Siepmann M, Liu Z, Schmitz G, Kiessling F, Gatjens J (2011) Advanced characterization and refinement of poly N-butyl cyanoacrylate microbubbles for ultrasound imaging. Ultrasound Med Biol 37: 1622-34

Folkman J (1971) Tumor angiogenesis: therapeutic implications. N Engl J Med 285: 1182-6

Frenkel V (2008) Ultrasound mediated delivery of drugs and genes to solid tumors. Adv Drug Deliv Rev 60: 1193-208

Genovese F, Boor P, Papasotiriou M, Leeming DJ, Karsdal MA, Floege J (2016) Turnover of type III collagen reflects disease severity and is associated with progression and microinflammation in patients with IgA nephropathy. Nephrol Dial Transplant 31: 472-9

Genovese F, Manresa AA, Leeming DJ, Karsdal MA, Boor P (2014) The extracellular matrix in the kidney: a source of novel non-invasive biomarkers of kidney fibrosis? Fibrogenesis Tissue Repair 7: 4

Gerlinger M, Rowan AJ, Horswell S, Math M, Larkin J, Endesfelder D, Gronroos E, Martinez P, Matthews N, Stewart A, Tarpey P, Varela I, Phillimore B, Begum S, McDonald NQ, Butler A, Jones D, Raine K, Latimer C, Santos CR et al. (2012) Intratumor

heterogeneity and branched evolution revealed by multiregion sequencing. N Engl J Med 366: 883-892

Goel S, Duda DG, Xu L, Munn LL, Boucher Y, Fukumura D, Jain RK (2011) Normalization of the vasculature for treatment of cancer and other diseases. Physiol Rev 91: 1071-121

Gremse F, Doleschel D, Zafarnia S, Babler A, Jahnen-Dechent W, Lammers T, Lederle W, Kiessling F (2015) Hybrid microCT-FMT imaging and image analysis. J Vis Exp: e52770

Gremse F, Stark M, Ehling J, Menzel JR, Lammers T, Kiessling F (2016) Imalytics Preclinical: Interactive Analysis of Biomedical Volume Data. Theranostics 6: 328-41

Heldin CH, Rubin K, Pietras K, Ostman A (2004) High interstitial fluid pressure - an obstacle in cancer therapy. Nat Rev Cancer 4: 806-13

Hersh DS, Nguyen BA, Dancy JG, Adapa AR, Winkles JA, Woodworth GF, Kim AJ, Frenkel V (2016) Pulsed ultrasound expands the extracellular and perivascular spaces of the brain. Brain Res 1646: 543-550

Hill NR, Fatoba ST, Oke JL, Hirst JA, O'Callaghan CA, Lasserson DS, Hobbs FD (2016) Global Prevalence of Chronic Kidney Disease - A Systematic Review and Meta-Analysis. PLoS One 11: e0158765

Hogan JJ, Mocanu M, Berns JS (2016) The Native Kidney Biopsy: Update and Evidence for Best Practice. Clin J Am Soc Nephrol 11: 354-62

Hu Y, Wan JM, Yu AC (2013) Membrane perforation and recovery dynamics in microbubble-mediated sonoporation. Ultrasound Med Biol 39: 2393-405

Huang Y, Goel S, Duda DG, Fukumura D, Jain RK (2013) Vascular normalization as an emerging strategy to enhance cancer immunotherapy. Cancer Res 73: 2943-8

Huang Y, Snuderl M, Jain RK (2011) Polarization of tumor-associated macrophages: a novel strategy for vascular normalization and antitumor immunity. Cancer Cell 19: 1-2

Hui L, Chen Y (2015) Tumor microenvironment: Sanctuary of the devil. Cancer Lett 368: 7-13

Husseini GA, Pitt WG, Martins AM (2014) Ultrasonically triggered drug delivery: breaking the barrier. Colloids Surf B Biointerfaces 123: 364-86

Huynh E, Zheng G (2015) Cancer nanomedicine: addressing the dark side of the enhanced permeability and retention effect. Nanomedicine (Lond) 10: 1993-5

Hynes RO (2009) The extracellular matrix: not just pretty fibrils. Science 326: 1216-9

Jacobs TW, Byrne C, Colditz G, Connolly JL, Schnitt SJ (1999) Radial scars in benign breast-biopsy specimens and the risk of breast cancer. N Engl J Med 340: 430-6

Jain RK (1990) Vascular and interstitial barriers to delivery of therapeutic agents in tumors. Cancer Metastasis Rev 9: 253-66

Jain RK (2001) Delivery of molecular and cellular medicine to solid tumors. Adv Drug Deliv Rev 46: 149-68

Jain RK (2005) Normalization of tumor vasculature: an emerging concept in antiangiogenic therapy. Science 307: 58-62

Jain RK, Duda DG, Clark JW, Loeffler JS (2006) Lessons from phase III clinical trials on anti-VEGF therapy for cancer. Nat Clin Pract Oncol 3: 24-40

Jain RK, Stylianopoulos T (2010) Delivering nanomedicine to solid tumors. Nat Rev Clin Oncol 7: 653-64

Jones AL, Hulett MD, Parish CR (2005) Histidine-rich glycoprotein: A novel adaptor protein in plasma that modulates the immune, vascular and coagulation systems. Immunol Cell Biol 83: 106-18

Khawar IA, Kim JH, Kuh HJ (2015) Improving drug delivery to solid tumors: priming the tumor microenvironment. J Control Release 201: 78-89

Khwaja A, El Kossi M, Floege J, El Nahas M (2007) The management of CKD: a look into the future. Kidney Int 72: 1316-23

Kiessling F, Fokong S, Bzyl J, Lederle W, Palmowski M, Lammers T (2014a) Recent advances in molecular, multimodal and theranostic ultrasound imaging. Adv Drug Deliv Rev 72: 15-27

Kiessling F, Mertens ME, Grimm J, Lammers T (2014b) Nanoparticles for imaging: top or flop? Radiology 273: 10-28

Kim H, Oda T, Lopez-Guisa J, Wing D, Edwards DR, Soloway PD, Eddy AA (2001) TIMP-1 deficiency does not attenuate interstitial fibrosis in obstructive nephropathy. J Am Soc Nephrol 12: 736-48

Klemm F, Joyce JA (2015) Microenvironmental regulation of therapeutic response in cancer. Trends Cell Biol 25: 198-213

Klinkhammer BM, Goldschmeding R, Floege J, Boor P (2017) Treatment of Renal Fibrosis-Turning Challenges into Opportunities. Adv Chronic Kidney Dis 24: 117-129

Kooiman K, Vos HJ, Versluis M, de Jong N (2014) Acoustic behavior of microbubbles and implications for drug delivery. Adv Drug Deliv Rev 72: 28-48

Krahn KN, Bouten CV, van Tuijl S, van Zandvoort MA, Merkx M (2006) Fluorescently labeled collagen binding proteins allow specific visualization of collagen in tissues and live cell culture. Anal Biochem 350: 177-85

Kunjachan S, Gremse F, Theek B, Koczera P, Pola R, Pechar M, Etrych T, Ulbrich K, Storm G, Kiessling F, Lammers T (2013) Noninvasive optical imaging of nanomedicine biodistribution. ACS Nano 7: 252-62

Lammers T (2013) Smart drug delivery systems: back to the future vs. clinical reality. Int J Pharm 454: 527-9

Lammers T, Kiessling F, Ashford M, Hennink W, Crommelin D, Storm G (2016) Cancer nanomedicine: Is targeting our target? Nat Rev Mater 1

Lammers T, Kiessling F, Hennink WE, Storm G (2012) Drug targeting to tumors: principles, pitfalls and (pre-) clinical progress. J Control Release 161: 175-87

Lammers T, Koczera P, Fokong S, Gremse F, Ehling J, Vogt M, Pich A, Storm G, van Zandvoort M, Kiessling F (2015) Theranostic USPIO-Loaded Microbubbles for Mediating and Monitoring Blood-Brain Barrier Permeation. Adv Funct Mater 25: 36-43

Lammers T, Peschke P, Kuhnlein R, Subr V, Ulbrich K, Debus J, Huber P, Hennink W, Storm G (2007) Effect of radiotherapy and hyperthermia on the tumor accumulation of HPMA copolymer-based drug delivery systems. J Control Release 117: 333-41

Lammertink BH, Bos C, Deckers R, Storm G, Moonen CT, Escoffre JM (2015) Sonochemotherapy: from bench to bedside. Front Pharmacol 6: 138

Langer R (1998) Drug delivery and targeting. Nature 392: 5-10

Lentacker I, De Cock I, Deckers R, De Smedt SC, Moonen CT (2014) Understanding ultrasound induced sonoporation: definitions and underlying mechanisms. Adv Drug Deliv Rev 72: 49-64

Levental KR, Yu H, Kass L, Lakins JN, Egeblad M, Erler JT, Fong SF, Csiszar K, Giaccia A, Weninger W, Yamauchi M, Gasser DL, Weaver VM (2009) Matrix crosslinking forces tumor progression by enhancing integrin signaling. Cell 139: 891-906

Li P, Zheng Y, Ran H, Tan J, Lin Y, Zhang Q, Ren J, Wang Z (2012) Ultrasound triggered drug release from 10-hydroxycamptothecin-loaded phospholipid microbubbles for targeted tumor therapy in mice. J Control Release 162: 349-54

Lin YF, Lee YH, Hsu YH, Chen YJ, Lin YF, Cheng FY, Chiu HW (2017) Resveratrol-loaded nanoparticles conjugated with kidney injury molecule-1 as a drug delivery system for potential use in chronic kidney disease. Nanomedicine (Lond) 12: 2741-2756

Luyckx VA, Tonelli M, Stanifer JW (2018) The global burden of kidney disease and the sustainable development goals. Bull World Health Organ 96: 414-422D

Maeda H (2012) Macromolecular therapeutics in cancer treatment: the EPR effect and beyond. J Control Release 164: 138-44

Maeda H, Nakamura H, Fang J (2013) The EPR effect for macromolecular drug delivery to solid tumors: Improvement of tumor uptake, lowering of systemic toxicity, and distinct tumor imaging in vivo. Adv Drug Deliv Rev 65: 71-9

Mahadevan D, Von Hoff DD (2007) Tumor-stroma interactions in pancreatic ductal adenocarcinoma. Mol Cancer Ther 6: 1186-97

Makowski MR, Wiethoff AJ, Blume U, Cuello F, Warley A, Jansen CH, Nagel E, Razavi R, Onthank DC, Cesati RR, Marber MS, Schaeffter T, Smith A, Robinson SP, Botnar RM (2011) Assessment of atherosclerotic plaque burden with an elastin-specific magnetic resonance contrast agent. Nat Med 17: 383-8

Manning DS, Afdhal NH (2008) Diagnosis and quantitation of fibrosis. Gastroenterology 134: 1670-81

Mantovani A, Allavena P, Sica A, Balkwill F (2008) Cancer-related inflammation. Nature 454: 436-44

Matsumura Y, Maeda H (1986) A new concept for macromolecular therapeutics in cancer chemotherapy: mechanism of tumoritropic accumulation of proteins and the antitumor agent smancs. Cancer Res 46: 6387-92

Megens RT, Oude Egbrink MG, Cleutjens JP, Kuijpers MJ, Schiffers PH, Merkx M, Slaaf DW, van Zandvoort MA (2007) Imaging collagen in intact viable healthy and

atherosclerotic arteries using fluorescently labeled CNA35 and two-photon laser scanning microscopy. Mol Imaging 6: 247-60

Meijering BD, Juffermans LJ, van Wamel A, Henning RH, Zuhorn IS, Emmer M, Versteilen AM, Paulus WJ, van Gilst WH, Kooiman K, de Jong N, Musters RJ, Deelman LE, Kamp O (2009) Ultrasound and microbubble-targeted delivery of macromolecules is regulated by induction of endocytosis and pore formation. Circ Res 104: 679-87

Miller MA, Zheng YR, Gadde S, Pfirschke C, Zope H, Engblom C, Kohler RH, Iwamoto Y, Yang KS, Askevold B, Kolishetti N, Pittet M, Lippard SJ, Farokhzad OC, Weissleder R (2015) Tumour-associated macrophages act as a slow-release reservoir of nano-therapeutic Pt(IV) pro-drug. Nat Commun 6: 8692

Mills KT, Xu Y, Zhang W, Bundy JD, Chen CS, Kelly TN, Chen J, He J (2015) A systematic analysis of worldwide population-based data on the global burden of chronic kidney disease in 2010. Kidney Int 88: 950-7

Mitragotri S, Lammers T, Bae YH, Schwendeman S, De Smedt S, Leroux JC, Peer D, Kwon IC, Harashima H, Kikuchi A, Oh YK, Torchilin V, Hennink W, Hanes J, Park K (2017) Drug Delivery Research for the Future: Expanding the Nano Horizons and Beyond. J Control Release 246: 183-184

Mo S, Coussios CC, Seymour L, Carlisle R (2012) Ultrasound-enhanced drug delivery for cancer. Expert Opin Drug Deliv 9: 1525-38

Mohammadkhah M, Simms CK, Murphy P (2017) Visualisation of Collagen in fixed skeletal muscle tissue using fluorescently tagged Collagen binding protein CNA35. J Mech Behav Biomed Mater 66: 37-44

Mortality GBD, Causes of Death C (2015) Global, regional, and national age-sex specific all-cause and cause-specific mortality for 240 causes of death, 1990-2013: a systematic analysis for the Global Burden of Disease Study 2013. Lancet 385: 117-71

Mossman BT, Churg A (1998) Mechanisms in the pathogenesis of asbestosis and silicosis. Am J Respir Crit Care Med 157: 1666-80

Mpekris F, Baish JW, Stylianopoulos T, Jain RK (2017) Role of vascular normalization in benefit from metronomic chemotherapy. Proc Natl Acad Sci U S A 114: 1994-1999

Murray LA (2015) Editorial: The Cell Types of Fibrosis. Front Pharmacol 6: 311

Nakamura H, Fang J, Maeda H (2015) Development of next-generation macromolecular drugs based on the EPR effect: challenges and pitfalls. Expert Opin Drug Deliv 12: 53-64

Nakamura Y, Mochida A, Choyke PL, Kobayashi H (2016) Nanodrug Delivery: Is the Enhanced Permeability and Retention Effect Sufficient for Curing Cancer? Bioconjug Chem 27: 2225-2238

Neesse A, Michl P, Frese KK, Feig C, Cook N, Jacobetz MA, Lolkema MP, Buchholz M, Olive KP, Gress TM, Tuveson DA (2011) Stromal biology and therapy in pancreatic cancer. Gut 60: 861-8

Netti PA, Berk DA, Swartz MA, Grodzinsky AJ, Jain RK (2000) Role of extracellular matrix assembly in interstitial transport in solid tumors. Cancer Res 60: 2497-503

Nichols JW, Bae YH (2014) EPR: Evidence and fallacy. J Control Release 190: 451-64

Nie S (2010) Understanding and overcoming major barriers in cancer nanomedicine. Nanomedicine (Lond) 5: 523-8

Ohlund D, Elyada E, Tuveson D (2014) Fibroblast heterogeneity in the cancer wound. J Exp Med 211: 1503-23

Ojha T, Pathak V, Shi Y, Hennink WE, Moonen CTW, Storm G, Kiessling F, Lammers T (2017) Pharmacological and physical vessel modulation strategies to improve EPR-mediated drug targeting to tumors. Adv Drug Deliv Rev 119: 44-60

Ojha T, Rizzo L, Storm G, Kiessling F, Lammers T (2015) Image-guided drug delivery: preclinical applications and clinical translation. Expert Opin Drug Deliv 12: 1203-7

Olsson AK, Larsson H, Dixelius J, Johansson I, Lee C, Oellig C, Bjork I, Claesson-Welsh L (2004) A fragment of histidine-rich glycoprotein is a potent inhibitor of tumor vascularization. Cancer Res 64: 599-605

Papasotiriou M, Genovese F, Klinkhammer BM, Kunter U, Nielsen SH, Karsdal MA, Floege J, Boor P (2015) Serum and urine markers of collagen degradation reflect renal fibrosis in experimental kidney diseases. Nephrol Dial Transplant 30: 1112-21

Park JH, McMillan DC, Powell AG, Richards CH, Horgan PG, Edwards J, Roxburgh CS (2015) Evaluation of a tumor microenvironment-based prognostic score in primary operable colorectal cancer. Clin Cancer Res 21: 882-8

Park JH, Richards CH, McMillan DC, Horgan PG, Roxburgh CS (2014) The relationship between tumour stroma percentage, the tumour microenvironment and survival in patients with primary operable colorectal cancer. Ann Oncol 25: 644-51

Peer D, Karp JM, Hong S, Farokhzad OC, Margalit R, Langer R (2007) Nanocarriers as an emerging platform for cancer therapy. Nat Nanotechnol 2: 751-60

Perry JL, Reuter KG, Luft JC, Pecot CV, Zamboni W, DeSimone JM (2017) Mediating Passive Tumor Accumulation through Particle Size, Tumor Type, and Location. Nano Lett 17: 2879-2886

Petersen GH, Alzghari SK, Chee W, Sankari SS, La-Beck NM (2016) Meta-analysis of clinical and preclinical studies comparing the anticancer efficacy of liposomal versus conventional non-liposomal doxorubicin. J Control Release 232: 255-64

Pickup MW, Mouw JK, Weaver VM (2014) The extracellular matrix modulates the hallmarks of cancer. EMBO Rep 15: 1243-53

Poon C, McMahon D, Hynynen K (2017) Noninvasive and targeted delivery of therapeutics to the brain using focused ultrasound. Neuropharmacology 120: 20-37

Poon IK, Patel KK, Davis DS, Parish CR, Hulett MD (2011) Histidine-rich glycoprotein: the Swiss Army knife of mammalian plasma. Blood 117: 2093-101

Poste G, Fidler IJ (1980) The pathogenesis of cancer metastasis. Nature 283: 139-46

Prabhakar U, Maeda H, Jain RK, Sevick-Muraca EM, Zamboni W, Farokhzad OC, Barry ST, Gabizon A, Grodzinski P, Blakey DC (2013) Challenges and key considerations of the

enhanced permeability and retention effect for nanomedicine drug delivery in oncology. Cancer Res 73: 2412-7

Provenzano PP, Eliceiri KW, Campbell JM, Inman DR, White JG, Keely PJ (2006) Collagen reorganization at the tumor-stromal interface facilitates local invasion. BMC Med 4: 38

Radisky D, Hagios C, Bissell MJ (2001) Tumors are unique organs defined by abnormal signaling and context. Semin Cancer Biol 11: 87-95

Radisky DC, Kenny PA, Bissell MJ (2007) Fibrosis and cancer: do myofibroblasts come also from epithelial cells via EMT? J Cell Biochem 101: 830-9

Ramos AM, Gonzalez-Guerrero C, Sanz A, Sanchez-Nino MD, Rodriguez-Osorio L, Martin-Cleary C, Fernandez-Fernandez B, Ruiz-Ortega M, Ortiz A (2015) Designing drugs that combat kidney damage. Expert Opin Drug Discov 10: 541-56

Rapoport N, Payne A, Dillon C, Shea J, Scaife C, Gupta R (2013) Focused ultrasound-mediated drug delivery to pancreatic cancer in a mouse model. J Ther Ultrasound 1: 11

Rihova B, Jelinkova M, Strohalm J, Subr V, Plocova D, Hovorka O, Novak M, Plundrova D, Germano Y, Ulbrich K (2000) Polymeric drugs based on conjugates of synthetic and natural macromolecules. II. Anti-cancer activity of antibody or (Fab')(2)-targeted conjugates and combined therapy with immunomodulators. J Control Release 64: 241-61

Rix A, Palmowski M, Gremse F, Palmowski K, Lederle W, Kiessling F, Bzyl J (2014) Influence of repetitive contrast agent injections on functional and molecular ultrasound measurements. Ultrasound Med Biol 40: 2468-75

Rizzo LY, Theek B, Storm G, Kiessling F, Lammers T (2013) Recent progress in nanomedicine: therapeutic, diagnostic and theranostic applications. Curr Opin Biotechnol 24: 1159-66

Robertson EG, Baxter G (2011) Tumour seeding following percutaneous needle biopsy: the real story! Clin Radiol 66: 1007-14

Rockey DC, Bell PD, Hill JA (2015) Fibrosis--A Common Pathway to Organ Injury and Failure. N Engl J Med 373: 96

Rolny C, Mazzone M, Tugues S, Laoui D, Johansson I, Coulon C, Squadrito ML, Segura I, Li X, Knevels E, Costa S, Vinckier S, Dresselaer T, Akerud P, De Mol M, Salomaki H, Phillipson M, Wyns S, Larsson E, Buysschaert I et al. (2011) HRG inhibits tumor growth and metastasis by inducing macrophage polarization and vessel normalization through downregulation of PlGF. Cancer Cell 19: 31-44

Ross JP, Cai X, Chiu JF, Yang J, Wu J (2002) Optical and atomic force microscopic studies on sonoporation. J Acoust Soc Am 111: 1161-4

Sanches PG, Muhlmeister M, Seip R, Kaijzel E, Lowik C, Bohmer M, Tiemann K, Grull H (2014) Ultrasound-mediated gene delivery of naked plasmid DNA in skeletal muscles: a case for bolus injections. J Control Release 195: 130-7

Sanders HM, Iafisco M, Pouget EM, Bomans PH, Nudelman F, Falini G, de With G, Merkx M, Strijkers GJ, Nicolay K, Sommerdijk NA (2011) The binding of CNA35 contrast agents to collagen fibrils. Chem Commun (Camb) 47: 1503-5

Sangwaiya MJ, Sherman DI, Lomas DJ, Shorvon PJ (2014) Latest developments in the imaging of fibrotic liver disease. Acta Radiol 55: 802-13

Schindelin J, Arganda-Carreras I, Frise E, Kaynig V, Longair M, Pietzsch T, Preibisch S, Rueden C, Saalfeld S, Schmid B, Tinevez JY, White DJ, Hartenstein V, Eliceiri K, Tomancak P, Cardona A (2012) Fiji: an open-source platform for biological-image analysis. Nat Methods 9: 676-82

Sheikov N, McDannold N, Sharma S, Hynynen K (2008) Effect of focused ultrasound applied with an ultrasound contrast agent on the tight junctional integrity of the brain microvascular endothelium. Ultrasound Med Biol 34: 1093-104

Shi J, Kantoff PW, Wooster R, Farokhzad OC (2017) Cancer nanomedicine: progress, challenges and opportunities. Nat Rev Cancer 17: 20-37

Snipstad S, Sulheim E, de Lange Davies C, Moonen C, Storm G, Kiessling F, Schmid R, Lammers T (2018) Sonopermeation to improve drug delivery to tumors: from fundamental understanding to clinical translation. Expert Opin Drug Deliv 15: 1249-1261

Song KH, Harvey BK, Borden MA (2018) State-of-the-art of microbubble-assisted blood-brain barrier disruption. Theranostics 8: 4393-4408

Stapleton S, Milosevic M, Tannock IF, Allen C, Jaffray DA (2015) The intra-tumoral relationship between microcirculation, interstitial fluid pressure and liposome accumulation. J Control Release 211: 163-70

Sterzel RB, Hartner A, Schlotzer-Schrehardt U, Voit S, Hausknecht B, Doliana R, Colombatti A, Gibson MA, Braghetta P, Bressan GM (2000) Elastic fiber proteins in the glomerular mesangium in vivo and in cell culture. Kidney Int 58: 1588-602

Stylianopoulos T, Jain RK (2013) Combining two strategies to improve perfusion and drug delivery in solid tumors. Proc Natl Acad Sci U S A 110: 18632-7

Stylianopoulos T, Jain RK (2015) Design considerations for nanotherapeutics in oncology. Nanomedicine 11: 1893-907

Sun Q, Baues M, Klinkhammer BM, Ehling J, Djudjaj S, Drude NI, Daniel C, Amann K, Kramann R, Kim H, Saez-Rodriguez J, Weiskirchen R, Onthank DC, Botnar RM, Kiessling F, Floege J, Lammers T, Boor P (2019) Elastin imaging enables noninvasive staging and treatment monitoring of kidney fibrosis. Sci Transl Med 11

Tampe D, Zeisberg M (2014) Potential approaches to reverse or repair renal fibrosis. Nat Rev Nephrol 10: 226-37

Theek B, Baues M, Gremse F, Pola R, Pechar M, Negwer I, Koynov K, Weber B, Barz M, Jahnen-Dechent W, Storm G, Kiessling F, Lammers T (2018) Histidine-rich glycoprotein-induced vascular normalization improves EPR-mediated drug targeting to and into tumors. J Control Release 282: 25-34

Theek B, Baues M, Ojha T, Mockel D, Veettil SK, Steitz J, van Bloois L, Storm G, Kiessling F, Lammers T (2016) Sonoporation enhances liposome accumulation and penetration in tumors with low EPR. J Control Release 231: 77-85

Theek B, Gremse F, Kunjachan S, Fokong S, Pola R, Pechar M, Deckers R, Storm G, Ehling J, Kiessling F, Lammers T (2014a) Characterizing EPR-mediated passive drug targeting using contrast-enhanced functional ultrasound imaging. J Control Release 182: 83-9

Theek B, Rizzo LY, Ehling J, Kiessling F, Lammers T (2014b) The Theranostic Path to Personalized Nanomedicine. Clin Transl Imaging 2: 66-76

Thomas D, Radhakrishnan P (2019) Tumor-stromal crosstalk in pancreatic cancer and tissue fibrosis. Mol Cancer 18: 14

Thongboonkerd V, Barati MT, McLeish KR, Benarafa C, Remold-O'Donnell E, Zheng S, Rovin BH, Pierce WM, Epstein PN, Klein JB (2004) Alterations in the renal elastin-elastase system in type 1 diabetic nephropathy identified by proteomic analysis. J Am Soc Nephrol 15: 650-62

Tinkov S, Coester C, Serba S, Geis NA, Katus HA, Winter G, Bekeredjian R (2010) New doxorubicin-loaded phospholipid microbubbles for targeted tumor therapy: in-vivo characterization. J Control Release 148: 368-72

Tolaney SM, Boucher Y, Duda DG, Martin JD, Seano G, Ancukiewicz M, Barry WT, Goel S, Lahdenrata J, Isakoff SJ, Yeh ED, Jain SR, Golshan M, Brock J, Snuderl M, Winer EP, Krop IE, Jain RK (2015) Role of vascular density and normalization in response to neoadjuvant bevacizumab and chemotherapy in breast cancer patients. Proc Natl Acad Sci U S A 112: 14325-30

Tsuchida-Straeten N, Ensslen S, Schafer C, Woltje M, Denecke B, Moser M, Graber S, Wakabayashi S, Koide T, Jahnen-Dechent W (2005) Enhanced blood coagulation and fibrinolysis in mice lacking histidine-rich glycoprotein (HRG). J Thromb Haemost 3: 865-72

Tugues S, Honjo S, Konig C, Noguer O, Hedlund M, Botling J, Deschoemaeker S, Wenes M, Rolny C, Jahnen-Dechent W, Mazzone M, Claesson-Welsh L (2012) Genetic deficiency in plasma protein HRG enhances tumor growth and metastasis by exacerbating immune escape and vessel abnormalization. Cancer Res 72: 1953-63

Tung JC, Barnes JM, Desai SR, Sistrunk C, Conklin MW, Schedin P, Eliceiri KW, Keely PJ, Seewaldt VL, Weaver VM (2015) Tumor mechanics and metabolic dysfunction. Free Radic Biol Med 79: 269-80

Ueno H, Jones A, Jass JR, Talbot IC (2002) Clinicopathological significance of the 'keloid-like' collagen and myxoid stroma in advanced rectal cancer. Histopathology 40: 327-34

Ueno H, Shinto E, Shimazaki H, Kajiwara Y, Sueyama T, Yamamoto J, Hase K (2015) Histologic categorization of desmoplastic reaction: its relevance to the colorectal cancer microenvironment and prognosis. Ann Surg Oncol 22: 1504-12

von Roemeling C, Jiang W, Chan CK, Weissman IL, Kim BYS (2017) Breaking Down the Barriers to Precision Cancer Nanomedicine. Trends Biotechnol 35: 159-171

Wang LM, Silva MA, D'Costa Z, Bockelmann R, Soonawalla Z, Liu S, O'Neill E, Mukherjee S, McKenna WG, Muschel R, Fokas E (2016) The prognostic role of desmoplastic stroma in pancreatic ductal adenocarcinoma. Oncotarget 7: 4183-94

Willett CG, Kozin SV, Duda DG, di Tomaso E, Kozak KR, Boucher Y, Jain RK (2006) Combined vascular endothelial growth factor-targeted therapy and radiotherapy for rectal cancer: theory and clinical practice. Semin Oncol 33: S35-40

Wong MG, Perkovic V, Woodward M, Chalmers J, Li Q, Hillis GS, Yaghobian Azari D, Jun M, Poulter N, Hamet P, Williams B, Neal B, Mancia G, Cooper M, Pollock CA (2013) Circulating bone morphogenetic protein-7 and transforming growth factor-beta1 are better predictors of renal end points in patients with type 2 diabetes mellitus. Kidney Int 83: 278-84

Wynn TA (2008) Cellular and molecular mechanisms of fibrosis. J Pathol 214: 199-210
Yazdani S, Bansal R, Prakash J (2017) Drug targeting to myofibroblasts: Implications for fibrosis and cancer. Adv Drug Deliv Rev 121: 101-116

Yu M, Tannock IF (2012) Targeting tumor architecture to favor drug penetration: a new weapon to combat chemoresistance in pancreatic cancer? Cancer Cell 21: 327-9

Yuana Y, Jiang L, Lammertink BHA, Vader P, Deckers R, Bos C, Schiffelers RM, Moonen CT (2017) Microbubbles-Assisted Ultrasound Triggers the Release of Extracellular Vesicles. Int J Mol Sci 18

Zaman MH, Trapani LM, Sieminski AL, Mackellar D, Gong H, Kamm RD, Wells A, Lauffenburger DA, Matsudaira P (2006) Migration of tumor cells in 3D matrices is governed by matrix stiffness along with cell-matrix adhesion and proteolysis. Proc Natl Acad Sci U S A 103: 10889-94

Zeisberg M, Kalluri R (2013) Cellular mechanisms of tissue fibrosis. 1. Common and organ-specific mechanisms associated with tissue fibrosis. Am J Physiol Cell Physiol 304: C216-25

Zeisberg M, Khurana M, Rao VH, Cosgrove D, Rougier JP, Werner MC, Shield CF, 3rd, Werb Z, Kalluri R (2006) Stage-specific action of matrix metalloproteinases influences progressive hereditary kidney disease. PLoS Med 3: e100

Zhao YZ, Luo YK, Lu CT, Xu JF, Tang J, Zhang M, Zhang Y, Liang HD (2008) Phospholipids-based microbubbles sonoporation pore size and reseal of cell membrane cultured in vitro. J Drug Target 16: 18-25

7. Appendix

7.1. List of original publications

1. **Baues M.***, Klinkhammer B.M.*, Ehling J., Gremse F., van Zandvoort M.A.M.J., Reutelingsperger C.P.M., Daniel C., Amann K., Bábíčková J., Kiessling F., Floege J., Lammers T.#, Boor P.#: A collagen-binding protein enables molecular imaging of kidney fibrosis in vivo. ***Kidney International***. [in press]
2. Sun Q.*, **Baues M.***, Klinkhammer B.M.*, Ehling J., Djudjaj S., Drude N.I., Daniel C., Amann K., Kramann R., Kim H., Saez-Rodriguez J., Weiskirchen R., Onthank D.C., Botnar R.M., Kiessling F., Floege J., Lammers T., Boor P.: Elastin imaging enables noninvasive staging and treatment monitoring of kidney fibrosis. ***Science Translational Medicine***. (2019) 486
3. Hansel C., Erschfeld S., **Baues M.**, Lammers T., Weiskirchen R., Trautwein C., Kroy D.C., Drescher H.K.: The Inhibitory T Cell Receptors PD1 and 2B4 Are Differentially Regulated on CD4 and CD8 T Cells in a Mouse Model of Non-alcoholic Steatohepatitis. ***Frontiers in Pharmacology***. (2019) 10:244
4. Ergen C., Niemietz P.M., Heymann F., **Baues M.**, Gremse F., Pola R., van Bloois L., Storm G., Kiessling F., Trautwein C., Luedde T., Lammers T., Tacke F.: Liver fibrosis affects the targeting properties of drug delivery systems to macrophage subsets in vivo. Biomaterials. ***Biomaterials***. (2019) 206:49-60
5. Drescher H.K., Schumacher F., Schenker T., **Baues M.**, Lammers T., Hieronymus T., Trautwein C., Streetz K.L., Kroy D.C.: c-Met Signaling Protects from Nonalcoholic Steatohepatitis- (NASH-) Induced Fibrosis in Different Liver Cell Types. ***Oxidative Medicine and Cellular Longevity***. (2018) 6957497
6. Theek B.*, **Baues M.***, Gremse F., Pola R., Pechar M., Negwer I., Koynov K., Weber B., Barz M., Jahnen-Dechent W., Storm G., Kiessling F., Lammers T.: Histidine-rich glycoprotein-induced vascular normalization improves EPR-mediated drug targeting to and into tumors. ***Journal of Controlled Release***. (2018) 282:25-34
7. **Baues M.**, Dasgupta A., Ehling J., Prakash J., Boor P., Tacke F., Kiessling F., Lammers T.: Fibrosis imaging: Current concepts and future directions. ***Advanced Drug Delivery Reviews***. (2017) 121:9-26

8. Tsvetkova Y., Beztsinna N., **Baues M.**, Klein D., Rix A., Golombek S.K., Al Rawashdeh W., Gremse F., Barz M., Koynov K., Banala S., Lederle W., Lammers T., Kiessling F.: Balancing Passive and Active Targeting to Different Tumor Compartments Using Riboflavin-Functionalized Polymeric Nanocarriers. ***Nano Letters***. (2017) 8:4665-4674
9. Bangen J., Hammerich L., Sonntag R., **Baues M.**, Haas U., Lambertz D., Longerich T., Lammers T., Tacke F., Trautwein C., Liedtke C.: Targeting CCl4 -induced liver fibrosis by RNA interference-mediated inhibition of cyclin E1 in mice. ***Hepatology***. (2017) 4:1242-1257
10. Theek B., **Baues M.**, Ojha T., Möckel D., Veettil S.K., Steitz J., van Bloois L., Storm G., Kiessling F., Lammers T.: Sonoporation enhances liposome accumulation and penetration in tumors with low EPR. ***Journal of Controlled Release***. (2016) 231:77-85.

7.2. Acknowledgments

First of all, I would like to thank Prof. Dr. Dr. Twan Lammers for all the interesting projects, for supporting me during the entire time and for always taking time to discuss. Your advice was encouraging as well as challenging, I am very grateful for the trust and for the incredible research freedom that I experienced.

I would like to thank Prof. Dr. Fabian Kiessling for his support, the opportunity to work in his laboratory and to perform my thesis at the Institute for Experimental Molecular Imaging.

Also, I would like to thank Prof. Dr. Peter Boor, who was an excellent cooperation partner and supported me as the second examiner of my thesis.

Further, I would like to express my gratitude to my early PhD supervisors, Benjamin Theek and Josef Ehling, for their excellent guidance and support.

A special thank you to all the cooperation partners that provided me with materials, assisted with experimental expertise, supported the research and contributed with productive criticism: Barbara Klinkhammer, Qinxue Sun, Natascha Drude, Felix Gremse, Sonja Djudjaj, Ralf Weiskirchen, Willi Jahnen-Dechent, Robert Pola, Michal Pechar, Inka Negwer, Kaloian Koynov, Benjamin Weber, Matthias Barz, Rafael Kramann, Hyojin Kim, Julio Saez-Rodriguez, Seena Koyadan Veetil, Julia Steitz, Louis van Blois, David Onthank, Marc von Zandvoort, Tarun Ohja, Anshuman Dasgupta, Chris Reutelingsperger, Christoph Daniel, Kerstin Amann, Jai Prakash, Frank Tacke, Janka Bábíčkova, Jürgen Floege, Rene Botnar and Gert Storm.

A big thank you to Marek Weiler, Anne Rix, Diana Möckel und Susi Koletnik, who continuously do their best and essentially supported my work.

I also want to thank the whole ExMI group for all the help, the really nice atmosphere and the amazing time. You made this roller coaster ride of a PhD enjoyable. Our beer o'clocks, the Karneval craziness, the original MoBi team, my two sets of officemates and Team Orga will always have a place in my heart.

A special thank you to Jan-Niklas May for being simply the best, most patient desk neighbor ever. On some occasions, you definitely stopped me from insanity and exploding. Keep it up and *egal was kommt, es wird gut, sowieso*!

Ein besonderer Dank gilt meiner Familie, im Besonderen meiner Schwester Jana, der weltbesten MTLA! Ich kann an dieser Stelle nicht in Worte fassen, was ihr mir bedeutet. Ihr habt mich zu jeder Zeit, in allen erdenklichen Weisen unterstützt. Ohne diesen bedingungslosen Rückhalt, eure vielen Ratschläge und euren Einsatz hätte ich meine Ziele nicht erreichen können. Danke!

Last but far from least, I would like to thank Tristan Wagner for listing, understanding and supporting me throughout the whole process. Thank you for turning this collection of words into a proper dissertation. Your contribution to this thesis is inestimably precious, as is your incredible ability of always making me laugh. You are the one, I want to discover the world with.

7.3. Erklärung zur Datenaufbewahrung

Erklärung § 5 Abs. 1 zur Datenaufbewahrung

Hiermit erkläre ich, dass die dieser Dissertation zu Grunde liegenden Originaldaten am Institut für Experimentelle Molekulare Bildgebung des Universitätsklinikums Aachen hinterlegt sind.

7.4. Erklärung über den Eigentanteil

Eidesstattliche Erklärung gemäß § 5 Abs. (1) und § 11 Abs. (3) 12. der Promotionsordnung

Hiermit erkläre ich, Maike Baues an Eides statt, dass ich folgende in der von mir selbstständig erstellten Dissertation „Modulating and monitoring the microenvironment in cancer and renal fibrosis“ dargestellten Ergebnisse erhoben habe:

Bei der Durchführung der Arbeit hatte ich folgende Hilfestellungen, die in der Danksagung angegeben sind

	Literaturrecherche	Studienplanung	Versuchsdurchführung *in vivo*	Versuchsdurchführung *ex vivo*	Mikroskopie	Bereitstellung von Materialien	Materialcharakterisierung	Massenspektrometrie	Datenauswertung	Statistische Auswertung	Interpretation der Datenauswertung
M. Baues	85	54	55	65	100				51	51	53
B. Theek	5	10	12	5					20	21	15
F. Gremse									5	5	
Q. Sun	3	4	10						5	5	5
B.M. Klinkhammer	5	10	12	22					15	15	20
J. Ehling	2	2	2	5							
S. Djudjaj			1							1	
N.I. Drude			1				35			1	
C. Daniel						13					
K. Amann						13					
R. Weiskirchen								100			
D.C. Onthank						13					
R.M. Botnar							15				
D. Möckel			5			8					
S.K. Veettil			1								
L. van Bloois						8					
M.A.M.J. van Zandvoort						6					
C.P.M. Reutelingsperger						6					
J. Bábíčková			1	3							
M. Barz							12		1		
B. Weber							13		1		
K. Koynov							12		1		
I. Negwer							13		1		
M. Pechar						10					
R. Pola						10					
W. Jahnen-Dechent						13					
F. Kiessling		5									
P. Boor		5									2
T. Lammers		10								1	5
Summe (%)	100	100	100	100	100	100	100	100	100	100	100

_____

Unterschrift der Doktorandin

Als Betreuer der obigen Dissertation bestätige ich die Angaben von Maike Baues

_____

Unterschrift des Doktorvaters

7.5. Curriculum vitae

Maike Baues

Alexanderstr. 28a

52499 Baesweiler

Phone: +(49)176-32864353

maike.baues@gmx.de

EDUCATION:

RWTH Aachen University, Aachen

Doctoral Studies June 2015 - present

- Dr. rer. medic. at the Institute for Experimental Molecular Imaging, Department for Nanomedicines and Theranostics
  "Modulating and monitoring the microenvironment in cancer and renal fibrosis"
- Certificate in Basics of Laboratory Animal Science according to FELASA B

Master of Science in Molecular Biotechnology October 2012 – May 2015

- Thesis at the Institute for Experimental Molecular Imaging, Department for Nanomedicines and Theranostics
  "Analyzing accumulation and penetration of nanomedicines in tumors upon vascular normalization and sonoporation"
- Area of specialization: Medical Biotechnology

Bachelor of Science in Molecular Biotechnology October 2009 – September 2012

- Thesis at the Fraunhofer Institute for Molecular Biology and Applied Ecology,
  "Development of a nanoparticle-based *Plasmodium falciparum* specific immunoassay"

EXPERIENCE:

Fraunhofer Center for Molecular Biotechnology, Newark, Delaware USA

Intern March 2014 – August 2014

- Design, generation, and cloning of Pfs25 CP-VLP constructs for Malaria transmission blocking vaccine
- Screening and expression of developed candidates in *N. benthamiana*
- Large scale purification of plant material using different chromatographic strategies and assessment techniques for CP-VLPs

Uniklinik RWTH Aachen – Institute for Medical Microbiology, Aachen

Intern November 2013 – January 2014

- Isolation and characterization of *S. aureus* strains out of anterior nares
- Isolation of bacteriophages against *S. aureus* from the environment

Fraunhofer Institute for Molecular Biology and Applied Ecology, Aachen

Research Assistant April 2012 – March 2014

- Development of coupling procedures for antibodies to nanoparticles
- Recombinant antigen expression and murine monoclonal antibody generation
- Establishment of proof of concept for malaria diagnostic multiplex-assay

Codexis Julich Chiral Solutions GmbH, Jülich

Intern Summer 2009

- Assisted team on various projects, from protein production to analytic tests and purity evaluation
- Gained experience in fermentation processes

PerkinElmer chemagen Technologie GmbH, Baesweiler

Intern July 2007

- Introduced to biopolymer technology for functionalization of magnetic beads
- Evaluated automated nucleic acid isolation

EXTRACURRICULAR ACTIVITIES:

TANDEMpeerMED program, RWTH Aachen University

Mentee November 2017 – Present

- Career planning, coaching and key competence development

German young Molecular Imaging Community, Germany

Founder, board member March 2017 – Present

- National network for young imaging scientists
- MoBi meeting organization, connect researchers and provide a mentoring platform

TANDEMschool program, RWTH Aachen University

Mentor May 2011 – March 2014

- Informed students about RWTH Aachen Universities field of study
- Presented life science subjects and projects to students

btS e.V., student group Aachen

Member April 2010 – Present

- Dedicate in area of public relations between universities, industry, and students
- Arrange seminars, speeches, panel discussions, and company contact fair

Sinfonietta Regio, orchestra, Aachen

Concertmaster December 2008 – April 2010

- Contributed to organization of concerts and exercised junior violins

AWARDS AND GRANTS:

- B. Braun-Stiftung research project funding "CXCL10-targeted T-cell nanoimmunotherapy against HCC"
- German Academic Exchange Service Congress Stipend, WMIC, 2018, Seattle
- Women in Molecular Imaging Network Scholar Award, WMIC, 2018, Seattle
- Student Travel Stipends, WMIC, 2018, Seattle
- Outstanding oral presentation, DGBM, 2016, Aachen
- Poster Award, EMIM, 2016, Utrecht
- Women in Molecular Imaging Network Scholar Award, WMIC, 2016, New York
- Student Travel Stipends, WMIC, 2016, New York

CONFERENCE PRESENTATIONS:

- Controlled Release Society (CRS) Annual Meeting & Exposition 2019
- European Molecular Imaging Meeting (EMIM) 2019, 2018, 2017, 2016, 2015
- European Club for Liver Cell Biology (ECLCB-8) 2018
- World Molecular Imaging Congress (WMIC) 2018, 2016
- Flanders Training Network Life Sciences (f-TALES) 2017
- Jahrestagung der Deutschen Gesellschaft für Biomaterialien (dgbm) 2016
- European Foundation for Clinical Nanomedicine (CLINAM) 2016

ADDITIONAL EXPERIENCE:

Ratskeller, restaurant, Aachen

Service Staff October 2014 – August 2015

Burger King, system catering, Alsdorf

Counter Attendant August 2007 – October 2012

LANGUAGE SKILLS:

- Fluent in written and spoken English
- Qualification in Latin

INTERESTS:

Skiing, Playing the violin, scuba diving, photography, travelling, strategic board games, reading, Pilates and bodystyling workout